Data-driven model-based approaches to condition monitoring and improving power output of wind turbines

Peng Qian

This thesis is submitted in partial fulfillment

of the requirements for the degree of

Doctor of Philosophy

May 2017

Lancaster University

Faculty of Science and Technology

Engineering Department

Declaration

I declare that this dissertation consists of original work undertaken solely by myself at Lancaster University and not been submitted in substantially the same form towards the award of a degree or other qualificatory work, and affirm that acknowledgement has been made to assistance given and that all major sources have been appropriately referenced.

Peng Qian

May 2017

Acknowledge

I am extremely grateful to my supervisor Dr Xiandong Ma for believing in me and offering his support throughout the project. His guidance, feedback and patience were essential not only for the progress of the research work, but also for the personal development during the PhD study.

I would like to thank Kathryn Rucastle and Laura Gracie for his important support throughout this work.

I also appreciate the supports from Prof. Claudio Paoloni for his support.

I wish to express my special and sincere thanks to Prof. Liangbi Li for her support in financial support and experimental tests.

Finally, I would like to express my gratitude to my parents. Their continuous encouragement and support have been invaluable for me throughout the PhD study. This thesis is dedicated to them.

Publications

Journal paper

P. Qian, X. Ma, and P. Cross, "An integrated data-driven model-based approach to condition monitoring of the wind turbine gearbox", *IET renewable power generation*, DOI: 10.1049/iet-rpg.2016.0216, 2017.

P. Qian, X. Ma, G. Liu, and Z. Chen " Reducing neutral point voltage fluctuation in NPC three-level active power filters Electrical Engineering", *Electrical Engineering*, DOI: 10.1007/s00202-017-0538-y

X. Ma, P. Cross, and P. Qian, "A condition monitoring system for an early warning of developing faults in wind turbine electrical systems," *Insight* vol. 58, pp. 663-670, 2016.

P. Qian, X. Ma, D. Zhang， "Estimating health condition of the wind turbine drivetrain system"， *energies*, DOI:10.3390/en10101583

P. Qian, X. Ma, D. Zhang, and J. Wang, "Optimizing wind farm power output control based on estimating health condition of wind turbines ", *IEEE transactions on sustainable energy* (under review)

Conference paper

P. Qian, X. Ma, and Y. Wang, "Condition monitoring of wind turbines based on extreme learning machine," presented at *the 21st International Conference on Automation & Computing*, Glasgow, UK, 2015.

Abstract

The development of the wind farm has grown dramatically in worldwide over the past 20 years. In order to satisfy the reliability requirement of the power grid, the wind farm should generate sufficient active power to make the frequency stable. Consequently, many methods have been proposed to achieve optimizing wind farm active power dispatch strategy. In previous research, it assumed that each wind turbine has the same health condition in the wind farm, hence the power dispatch for healthy and sub-healthy wind turbines are treated equally. It will accelerate the sub-healthy wind turbines damage, which may leads to decrease generating efficiency and increases operating cost of the wind farm. Thus, a novel wind farm active power dispatch strategy considering the health condition of wind turbines and wind turbine health condition estimation method are the proposed. A model-based CM approach for wind turbines based on the extreme learning machine (ELM) algorithm and analytic hierarchy process (AHP) are used to estimate health condition of the wind turbine. Essentially, the aim of the proposed method is to make the healthy wind turbines generate power as much as possible and reduce fatigue loads on the sub-healthy wind turbines. Compared with previous methods, the proposed methods is able to dramatically reduce the fatigue loads on sub-healthy wind turbines under the condition of satisfying network operator active power demand and maximize the operation efficiency of those healthy turbines. Subsequently, shunt active power filters (SAPFs) are used to improve power quality of the grid by mitigating harmonics injected from nonlinear loads, which is further to increase the reliability of the wind turbine system.

Abbreviations

ANN	Artificial neural network
AHP	Analytic hierarchy process
AI	Artificial intelligence
BP	Back propagation
CM	Condition monitoring
CNPCI	Current controlled NPC three-level inverter
DG	Distributed generation
DFIG	Doubly-fed induction generator
ED	Euclidean distance
ELM	Extreme learning machine
GA	Genetic algorithm
IGBT	Insulated gate bipolar transistor
LPF	Low pass filte
MD	Mahalanobis distance
MPPT	Maximum power point tracking
NPC	Neutral point clamped
PLL	Phase locked loop
PWM	Pulse-width modulation
PV	Photovoltaics
RIV	Risk indicator value

SLFN network	single hidden-layer feed forward neural
SCADA	Supervisory control and data acquisition
SAPF	Shunt active power filters
SCIG	Squirrel-cage induction generator
SVM	Support vector machine
SVPWM	Space voltage vector pulse-width modulation
THD	Total harmonic distortion
VNPCI	Voltage dependent NPC three-level inverter
WRIG	Wound rotor induction generator

Nomenclature

R	Length of the blade
T_a	Aerodynamic torque
F_t	Thrust force
ρ	Air density
v_r	Wind speed
C_p	Power coefficient
C_t	Thrust coefficient
J_r	Rotor inertia
J_g	Generator inertia
N_g	Gearbox ratio
T_s	Shaft torque
T_g	Real electrical torque of the generator

P_g^{cmd}	Reference power
T_g^{ref}	Reference electrical torque
β	Pitch angle
ω_f	Actual generator speed
ω_{rated}	Rated generator speed
τ_g	Time constant of the measurement filter
ΔV	voltage change
P	Active power
Q	Reactive power
v_{in}	Wind speed of the cut in
v_{out}	Wind speed of the cut out
U_H	Voltage harmonic content
U_n	Each voltage harmonic component
HRU_n	Distortion rate of voltage
I_H	Current harmonic content
I_n	Each current harmonic component
HRI_n	Distortion rate of current
u_{sa}, u_{sb}, u_{sc}	Three-phase alternating-current supply
i_{sa}, i_{sb}, i_{sc}	Grid currents
i_{La}, i_{Lb}, i_{Lc}	Load currents
i_{ca}, i_{cb}, i_{cc}	Compensation currents provided by the SAPF
u_o	Neutral point voltage of the three-phase bridge arm
u_N	Neutral point voltage of the DC-link capacitors
u_c	Voltage of the primary side of the transformer
u_b	Compensating voltage

u_s	DC-link voltage applied across the capacitors
S_1, S_2, S_3, S_4	IGBT power switches
T	Coupling transformer
L, C_f	LC filter
u_{dc}	DC voltage applied to the single-phase full-bridge inverter
u_i	Voltage output of the single-phase inverter
i_1	Current through the filter inductor
i_2	Transformer primary side current
i_{cf}	Current through the filter capacitor
D_1	Diode used to prevent reverse current flow
L_2, C_3	LC filter
u_{dc1}	Voltage input of the boost DC/DC converter
u_{dc2}	Voltage output of the boost DC/DC convertor
$i_{c3(off)}$	Current in capacitor C_3 when switching device S_5 is turned off
i_3	Current in the inductor L_1
i_4	Compensating current
$u_{L1(off)}$	Voltage across the inductor L_1 when switching device S_5 is turned off
$u_{L1(on)}$	Voltage across inductor L_1 when switch S_5 is turned on
D	Duty cycle of the switching device S_5
K_p, K_i	Parameters of the PI controller

Table of Content

List of Figures

List of Tables

Chapter1. Introduction

This chapter starts with a background information of wind power technologies. Then, the importance of wind energy research and the demand are given. Thereafter, the research motivation in developing condition monitoring system, health estimation method and optimizing strategy are illustrated. The objectives and aims involved in this dissertation are also described. Finally, the dissertation layout is demonstrated.

1.1 The importance of wind energy research

There has been a dramatic increase in the construction of wind farms over the past decade in global world, especially offshore wind installations, contributing to all around the world achieving targets for reducing CO_2 emissions and the production of sustainable energy [1], because of its technology maturity and improved cost competitiveness. Fig. 1.1 shows the global installation (GW) of wind turbines for each year, the installation of the wind turbines reaching 432 GW in the entire world in 2015. In order to achieve sustainable energy generation projects hold by industrial community, many countries have carried out corresponding targets and policies. Taking China for example, after Renewable Energy Law issued in 2006, the installation of wind turbines has witnessed a rapid growth by over 40 times from 2006 to 2015 [2]. In 2010, Chinese government carried out an explicit project for establishing eight 10-GW-level wind farms in Jiangsu, Jilin, Inner Mongolia, Hebei, Gansu and Xinjiang. As the rapid development of wind energy in China, some classical characteristics of wind energy in China are given as follow [3, 4]:

1) The installation of the wind turbines grows rapidly reaching high penetration level in abundant wind resource areas.

2) In some region, the establishment of wind farms is tend to be highly concentrated, especially in the northwest of China.

3) Over 90% wind farms are directly connected to the high-voltage power grid, including 110KV power grid and above, in China.

A more ambitious plan has been established in "High Renewable Energy Penetration Scenario and Roadmap Study, 2050 in China" hold by Energy Research Institute. This project plans to increase the wind power installation capacity to 2.4TW by the year of 2050, which accounts for more than 30% of the total power generation in China [2].

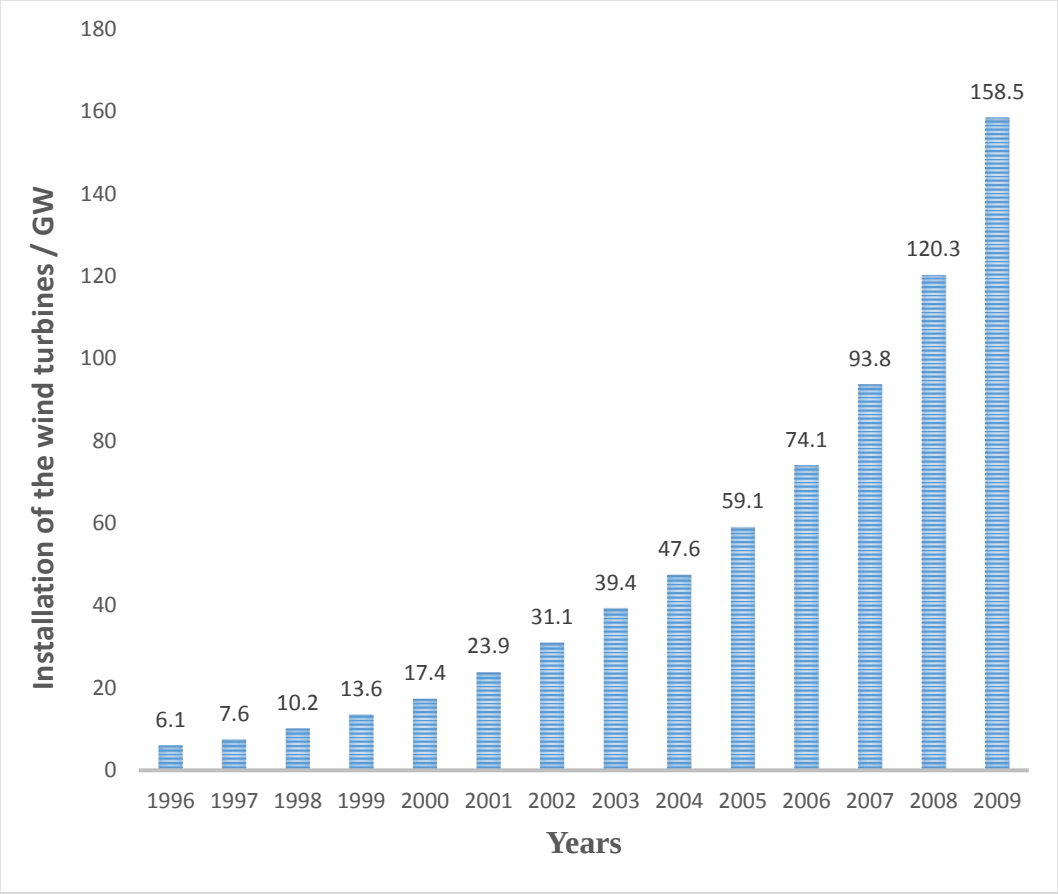

Figure 1.1 Global installation (GW) of wind turbines for each year [2]

Because of abundant wind resource on-shore, the development of wind power pay more attention to on-shore wind power projects. Compared with on-shore wind farm, the cost of the manufacture and maintenance for offshore wind farm is much higher, particularly when the wind turbines are operating in harsh environments and are sited in deep sea waters. From year 2015 to 2020, the new installation of the wind turbines will be expected to reach 25-30 GW per year. By year 2020, the total new installation of the wind turbines will be anticipated to 250-300GW, which meets 5% of the annual power demand. From year 2020 to 2040, a much more growth of the wind power construction are expected to be witnessed. By 2030, the scale of the wind power is expected to expand to more than 1.1 TW, consisting of both on-shore and offshore wind farms. At the end of 2050, the total newly installed

wind turbines will reach 2.7 TW. Corresponding wind power generation development plan is shown in Fig. 1.2.

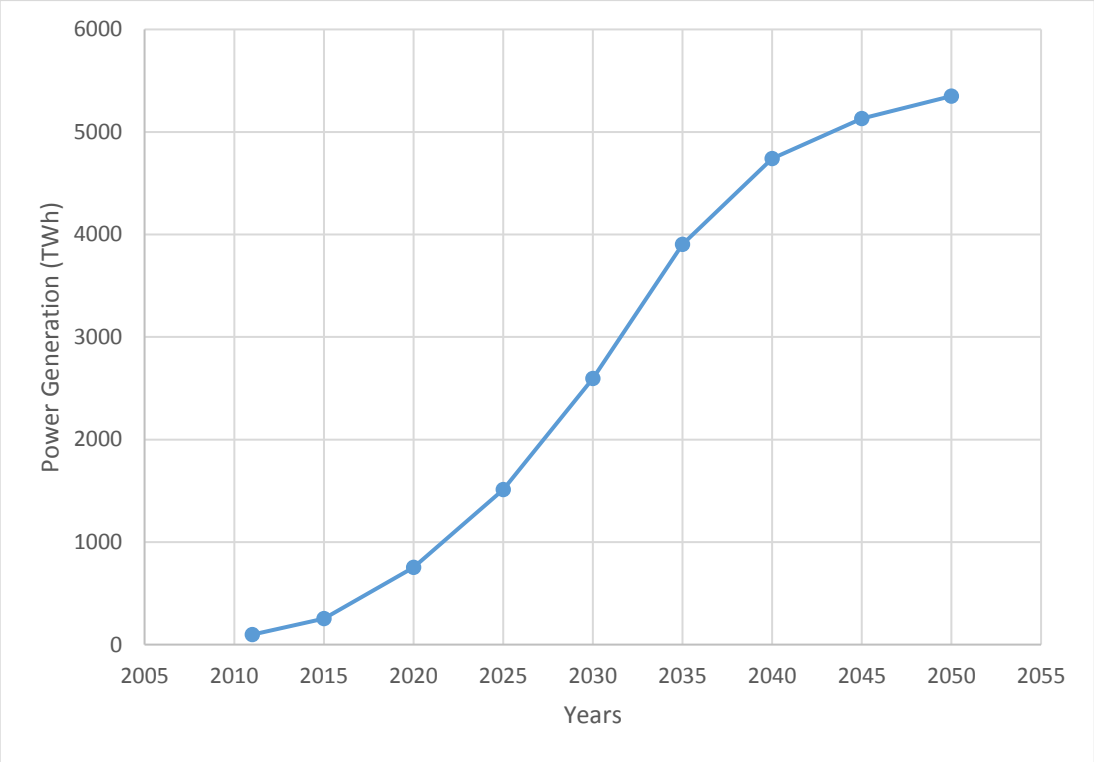

Figure 1.2 A wind power generation development plan in China [2]

Besides of China, The wind energy has been widely accepted as an effective energy solution to reducing CO_2 emissions and producing sustainable energy because of its technology maturity and improved cost competitiveness in UK. From the roadmap published by the Department of Energy and Climate Change, the UK government plans to make renewable energy generation satisfy 100% energy consumption for Scotland, 40% for Wales and Northern Ireland by 2020. In 2016, the installation of the wind turbine reaches 15031 MW and generating 41500 GW/h power output in UK, which accounts for 11.5% energy consumption.

Nowadays, one of the key priorities identified by the wind industry is to reduce costs in the operation and maintenance of wind turbines, which currently accounts

for 18% of the cost of offshore energy. Over an operating life of 20 years, maintenance costs of wind farm may reach 15% and 30% of the total income for onshore and offshore wind farms, respectively [5]. The costs of operation and maintenance for wind turbines are usually consisted of technician and engineering staff salaries, unexpected damage or maintenance and replacement parts and the costs associated with routine maintenance. The cost-effective operations of the wind farm is therefore crucial in the current industrial field due to the fierce competition in global sustainable energy market. Monitoring of the operating conditions of the wind turbines has been considered as an effective method to enhance the reliability of wind turbines and implement cost-effective maintenance. Clearly, it is essential to develop effective CM techniques for wind turbines [6-8], in order to provide information regarding the past and current conditions of the turbines and to enable the optimal scheduling of maintenance tasks [9, 10].

With increasing penetration of wind energy, the reliability of power grid effected by wind energy is a challenge [7]. Thus, it is necessary for wind farm to provide stable active and reactive powers to support the frequency and voltage value in the power grid [11, 12]. To fulfill these requirements, the operation of the modern wind farm is required to be much more like a conventional power plant [13]. In this circumstance, keeping each wind turbine operating in a stable condition is very essential. However, wind turbines are usually installed in harsh condition, especially for offshore wind farm, which poses a challenge for operation and maintenance of wind turbine [6, 14]. Wind turbine is also a complex generation system, health condition of each component will affect the whole system working efficiency. The wind turbine usually consists of a number of components and subsystems, including generator, gearbox, bearing, rotor hub and blade， main shaft， mechanical brake， power electronic converter [15, 16]. It is worth noting that health condition of each component or subsystem not only determines the whole wind turbine operational efficiency, but also affects an optimizing control strategy in wind farm control system, which plays a critical role in reliable operation of a large scale wind power plant when connected to the power grid.

In order to make wind turbines generating stable power, power electronics devices are widely used in wind power generation systems. However, power electronics device is a kind of nonlinear device [17-19] that generally generates harmonic currents. Harmonic currents are harmful to electrical equipment, which causes electrical equipment malfunction and also reduces life time of electrical equipment [20]. Meanwhile, harmonic currents also affect the reliability of wind farms. Active power filter (APF), as an effective technical means to solve the problem of harmonic pollution, has been obtained great concern [21-23]. Compared to traditional two-level voltage-source inverters used in SAPFs, three-level voltage-source inverters are able to bear higher voltage classes and operate with lower harmonic distortion and at lower switching frequencies. Three-level inverters therefore offer better performance, in particular for medium-voltage applications [24]. Thus, a NPC three-level APF is applied in wind power generation systems to enhance the reliability.

1.2 Project motivation and aims

Traditional wind farm power dispatch strategy is formulated by considering the available power and the power demand of the operators. The vast majority of research simply distributes power references to wind turbines based on a proportional distribution just following available active power from the wind farm and maximum demand for the reactive power [25]. Few works take account in the health condition of the wind turbines in wind farm. Thus, it is desirable to adopt an optimizing wind farm power output control based on estimating health condition of wind turbines. The flow chart of research propose is given in Fig. 1.3. The first step is condition monitoring of wind turbines. The condition monitoring system is able to monitor the operating status and detect the faults of the wind turbines by using model-based method. Although a method relying on residual signals alone can detect faults effectively, it is not able to provide accurate characteristics about the failure of components. Furthermore, the wind turbine generally has several

components, and traditional methods have only focused on detecting faults or identifying the health of an individual component [26]. Clearly, it would be desirable to use a more appropriate method in order to identify the health condition of the gearbox system as a whole. In second step, the results gained in step 1 can provide a quantitative value about fault degree of each component in wind turbines. As mentioned above, the wind turbine is a complex system and each component has different weight of index significance in whole system in terms of different maintenance time and cost caused. Hence, health condition estimation for the wind turbine can be regarded as a kind of multi-criterion decision making. In order to optimize power dispatch in the wind farm, it is necessary to adopt a method to solve multi-criterion decision making problem of wind turbines based on their health conditions. In third step, the optimal power control for wind farm based on heath condition estimation of individual turbines is to reduce mechanical loads acting on the faulty wind turbines while satisfying power output demanded by the network operator.

1.3 Objectives

In relation to the proposed research, the following objectives will be addressed:

Objective 1: To conduct a systematic literature review of background information of wind power technology, previous research works concerning to condition monitoring algorithms and techniques applied in wind turbines, and optimizing power dispatch strategy of the wind farm.

Objective 2: To study the supervisory control and data acquisition (SCADA) data obtained from a commercial operational wind farm for future research.

Objective 3: To propose appropriate model based algorithm to detect the faults of wind turbines effectively.

Objective 4: To establish health condition estimation method to assess the health condition of the whole wind turbine system.

Objective 5: To design an optimizing wind farm power output control strategy based on estimating health condition of wind turbines.

Objective 6: To adopt SAPF to enhance the reliability and output power quality of the wind farm

Objective 7: To validate and analyze the proposed methods and algorithms by using SCADA data and simulation data.

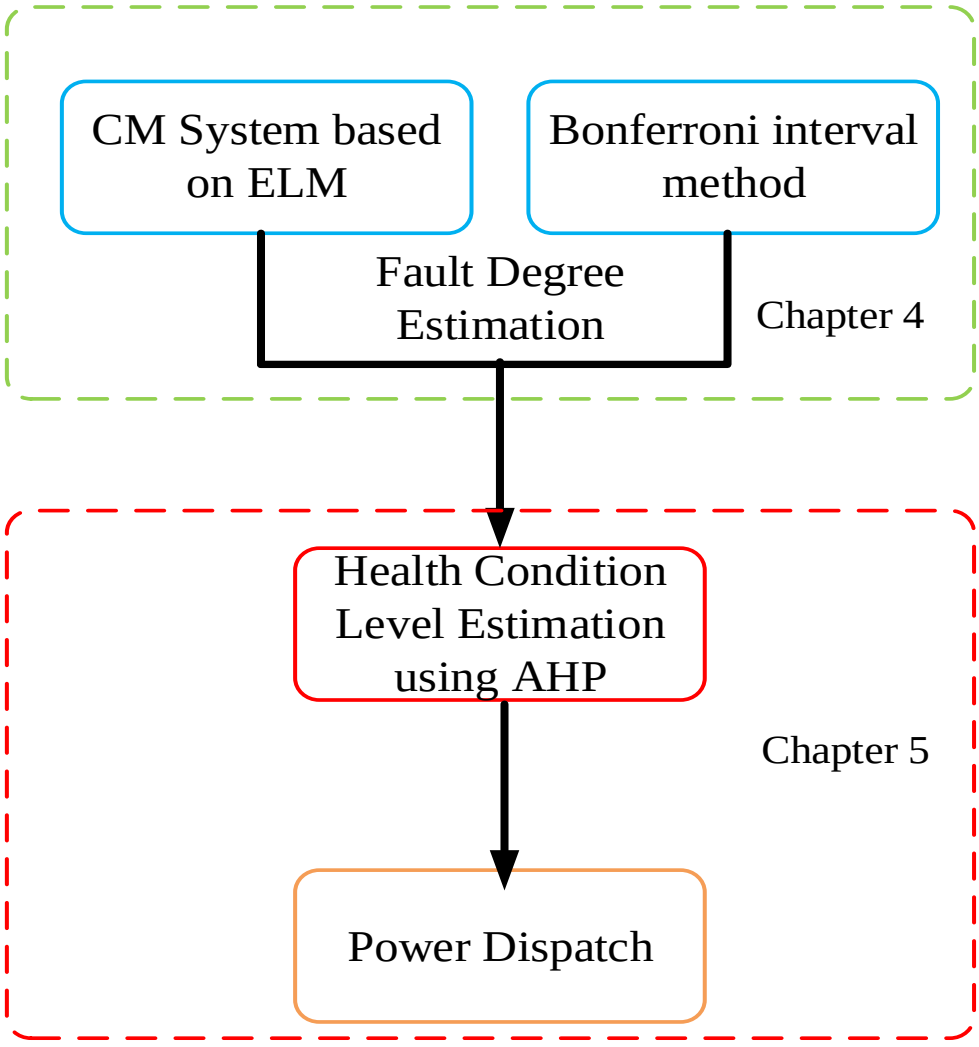

Figure 1.3 Flow chart of research propose

1.4 Layout of the thesis

The layout of this thesis describes as follows:

In the first chapter, it systematic illustrates the importance and necessary of wind power research and gives the motivation and research objectives. Besides, this chapter also describes the layout of the thesis.

In the second chapter, the background information and literature of previous research in terms of wind turbine condition monitoring and optimizing wind farm power output strategy are carried out. They include overview of wind turbine technologies, control strategy and algorithms.

In the third chapter, the structure and mathematical model of doubly fed induction generator (DFIG) are illustrated. Besides, SCADA data technology is introduced in this chapter, because the algorithms validation is based on SCADA data obtained from a commercial operating wind farm in this thesis.

In the fourth chapter, a model-based condition monitoring method based on extreme learning machine (ELM) is proposed to detect the faults occurred in the wind turbine system. However, wind turbines usually have several operating scenarios, which requires prediction model with training data updating ability. Thus, an improved ELM named online sequential extreme learning machine is adopted. In order to validate the effectiveness of proposed methods, they are compared with traditional back propagation (BP) artificial neural network. Finally, genetic algorithm is selected to optimize initial input weights and biases of ELM to overcome the drawback of random selecting initial input weights and biases.

In the fifth chapter, health condition of wind turbines is established by using residual signals obtained from chapter 4. Firstly, abnormal residual signals indicating faults occurring are assessed with a Bonferroni interval method for fault degree estimation. Secondly, analytic hierarchy process (AHP) that is a kind of technology for analysing complex decisions is used to estimate health condition level in terms of fault degree, maintenance cost and maintenance time. Finally,

optimal power dispatch control strategy is formulated based on result of health condition estimation.

In the sixth chapter, a new method for improving the performance of SAPFs using neutral point clamped (NPC) three-level inverters is presented. NPC three-level inverters often suffer excessive voltage fluctuations at the neutral-point of DC-link capacitors, which may damage switching devices and cause additional high harmonic distortion of the output voltage. In order to solve the problem, two compensating schemes are proposed to restrict voltage fluctuation in the inverters. The first is voltage dependent, adopting a voltage compensation method, while the second is current dependent, using a current compensation method.

In the seventh chapter, a conclusion for the current research is given. Achievements corresponding to the objectives set out in this chapter and the contributions to knowledge arising from this research are presented. Finally, the limitations of the algorithms proposed in this research and recommendations for future research are discussed.

Chapter2. Literature review of wind power system and condition monitoring technology

In this chapter, a review of the wind turbine technologies and wind turbine condition monitoring are given. Firstly, the background of current wind turbine technologies is illustrated; secondly, the detailed information about structure of DFIG wind turbine, including mathematical model of each subsystem, is described; finally, the review of the existing techniques for wind turbine condition monitoring, AI techniques used in model-based methods, and signal techniques applied in condition monitoring, including vibration signals, temperature signals, acoustic emission signals, torque signals and electrical signals are presented.

2.1 Overview of wind turbine technologies

Recently, there has been increasing interest in renewable energy because this kind of energy is more sustainable and eco-friendly. Wind turbines will play a crucial role in renewable energy system. Table 1 and Figure 2.1 illustrate the structures, configurations, operating and control principles, and gird connection methods of four types of typical wind turbines operated in the wind farm.

Fig. 2.1 (a) shows a constant speed wind turbine structure that is usually designed to operate in some particular wind speed arrange. Hence, any fluctuations of the wind speed will cause oscillation of power output. A squirrel-cage induction generator (SCIG) is usually adopted in this type of wind power generation system, which is generally designed to be appropriate for operating in specific rotate speed. The gearbox is a key component of the constant speed wind turbine, because the turbine rotor cannot reach synchronous speed that satisfies the operating condition of DFIG generator. The use of gearbox is to transmit kinetic energy from the turbine rotor to the SCIG electric generator through the drivetrain system. Two sets of windings are installed in SCIG to satisfy the efficiency of the power generation. However, this kind of wind power generation system has its drawbacks given as follow [27]: 1) the mechanical components need to bear high stress loads caused by sudden and substantial changes of the wind speed; 2) the power grid should have a good robustness due to the fluctuation of the power output; 3) the efficiency of this wind turbine is lower than the other types of wind turbines because of the constant speed operating.

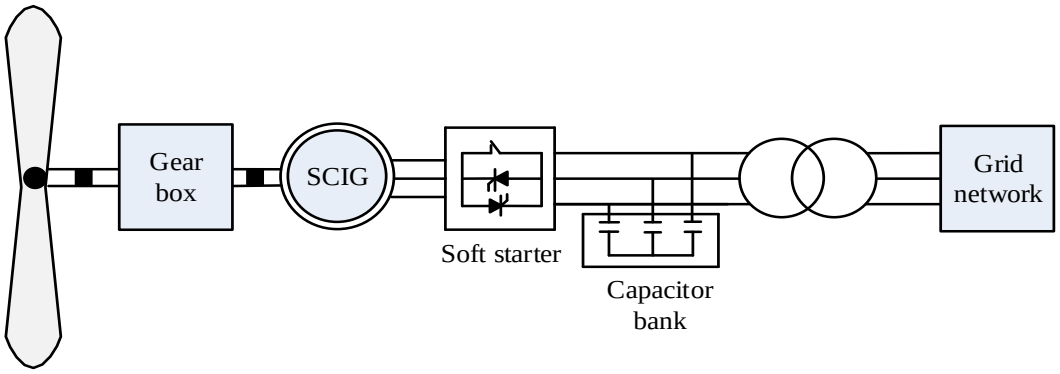

a. Constant speed wind turbine structure

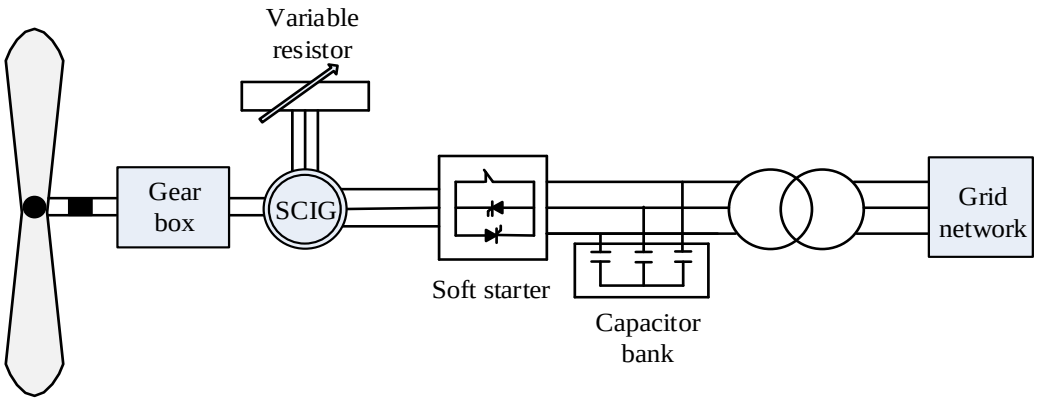

b. Variable speed wind turbine using variable resistor

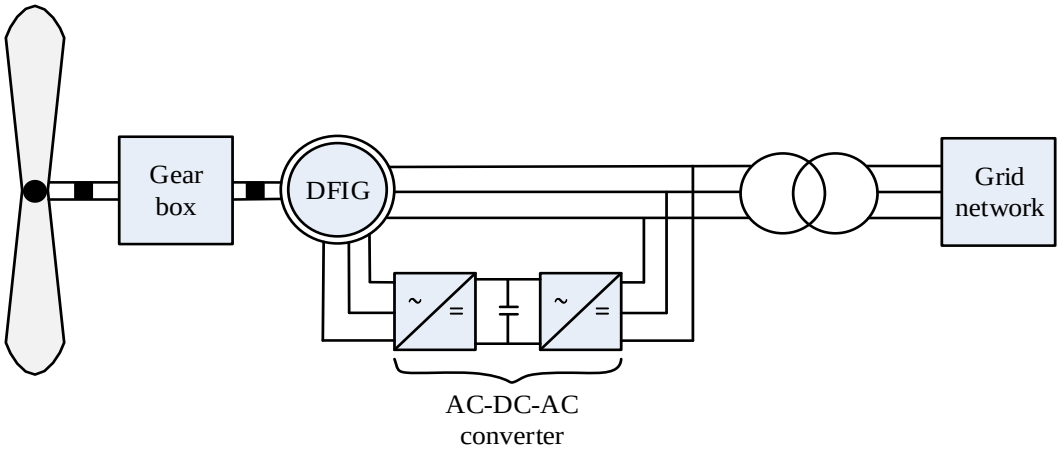

c. Doubly-fed induction indirect-drive wind turbine

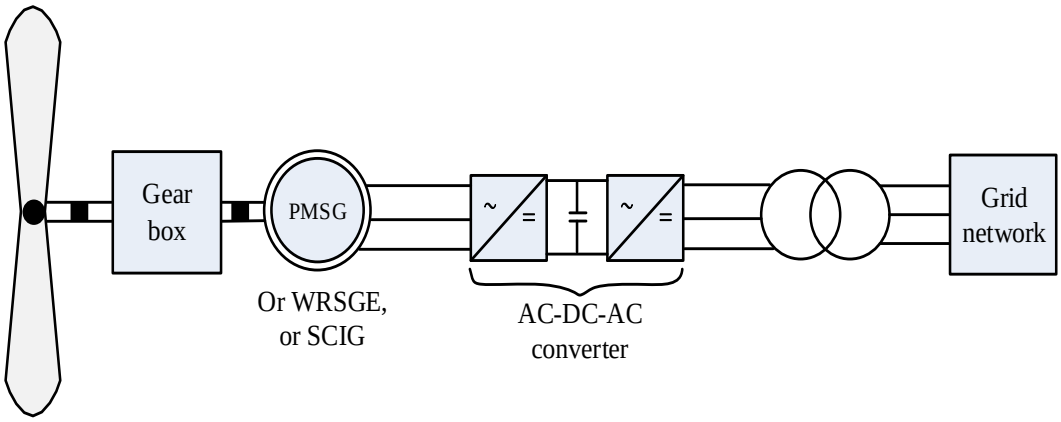

d. Permanent magnet synchronous direct-drive wind turbine

Figure 2.1 Four commonly applied wind turbine configurations

Fig 2.1 (b), (c) and (d) illustrate three types of variable speed wind turbines, which are designed to capture the maximum power over a range of wind speeds. Fig 2.1 (b) shows a variable speed wind turbine using variable resistor and a wound rotor induction generator (WRIG) method to achieve variable speed control. The rotate speed of generator is changed with the variable rotor resistance. This type of generator has more efficiency than the constant speed wind turbine [28]. However, the cost and reliability is not very satisfactory due to its complex structure.

Fig 2.1 (c) and (d) are two kinds for most extensively used wind turbines. Compared with previous variable speed wind turbine, these wind turbines adopt power electronics device to implement variable speed control [29-31]. From the failure data collected in the wind farm located in Germany, it was able to be found that direct-drive wind turbines are usually more reliable than indirect-drive wind turbines, because of the indirect-drive wind turbine with a gearbox. However, the permanent magnet synchronous direct-drive wind turbine should employ a full power converter, while the doubly-fed induction indirect-drive wind turbine adopts a 33% full power converter. It means that the cost and failure rate of the electronic components in the permanent magnet synchronous direct-drive wind turbine is

higher than that in the doubly-fed induction indirect-drive wind turbine, due to higher power level of the power converter

Type	Rotating Speed	Blade Control	Drivetrain	Generator	Grid Connection
a	Fixed speed	Pitch or stall control	Using a gearbox	Squirrel-cage induction generator	Directly connected
b	Partly variable speed	Pitch or stall control	Using a gearbox	Wound-rotor induction generator	Directly connected
c	Variable speed	Pitch control	Using a gearbox	Wound-rotor induction generator	Through partial-load power converters
d	Variable speed	Pitch control or fixed pitch	No gearbox	Synchronous generator	Through full-load power converters

Table 2.1 Classifications based on respective configurations and features

2.2 The structure of the wind power system and model

2.2.1 A typical doubly-fed wind turbine system

Over the past decades, wind energy has been widely accepted as an effective energy solution to reducing CO_2 emissions and producing sustainable energy because of its technology maturity and improved cost competitiveness. With increasing penetration of wind energy, the reliability of power grid effected by wind energy is a challenge. Thus, it is necessary for the wind farm to provide stable active and reactive powers to support the frequency and voltage value in the power grid. To fulfil these requirements, the operation of the modern wind farm is required to be much more like a conventional power plant [13]. In this circumstance, keeping each wind turbine operating in a stable condition is very essential. However, wind turbines are usually installed in harsh condition, especially for offshore wind farm,

which poses a challenge for operation and maintenance of wind turbine [6, 14]. The wind turbine is also a complex generation system, as shown in Fig 2.2, the health condition of each component will affect the whole system working efficiency. DFIG wind turbine is the most widely used wind turbine in the world. Compared with PMSG wind turbine, DFIG wind turbine has higher failure rate [34].

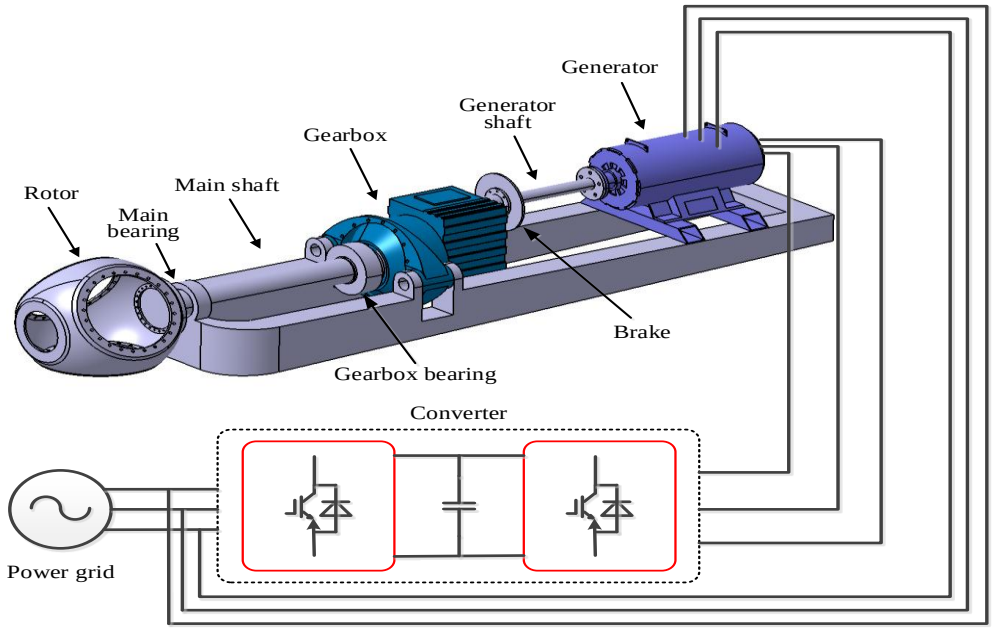

Figure 2.2 A typical doubly-fed wind turbine system with subsystems

2.2.1.1 Rotor hub and blade

The power generation of the wind turbine depends on the interaction between the rotate speed of the rotor and the wind speed. The rotor is composed of the hub and blades. The fault of rotor is usually caused by errors of the blade pitch angle or mass imbalance of blades. The faults of rotor hub and blade are generally caused by fatigue or surface roughness. Long-term fatigue will cause the delamination of blade's material, i.e. glass or carbon fiber-reinforced plastic structure, resulting in reducing the stiffness of the blade. Cracks will also be produced on the surface or

in the internal structure of blades, due to long-term fatigue. The surface of blades will become roughness, because of the exfoliation, blowholes, icing and pollution.

2.2.1.2 Gearbox

The gearbox is used to transmit kinetic energy from the turbine rotor to the electric generator, adjusting rotational speed and torque accordingly. However, the gearbox can be a major contributor to a turbine's downtime, with common failure modes being bearing faults and gear teeth faults. Surveys have shown that the root cause of gearbox failure is due to rapid changes of torque from stochastic wind profiles, which create an uneven load for the bearing and misalignment of gear teeth. Other causes of bearing and gear teeth failure are elevated operating temperature and excessive contamination of the cooling lubricant due to failure of the gearbox cooling system. Any fault from the gearbox can result in an abnormal power input to the generator, reducing efficiency or in extreme cases, damaging the generator [57-59]

Fig 2.3 shows a schematic diagram of the structure of a three-stage gearbox. The gearbox consists of three types of components, specifically, gears, bearings and the cooling system (usually oil cooling). In this thesis, gearbox temperature and oil pressure measurements at different locations of the gearbox obtained from the SCADA [32, 33] data are selected to monitor the condition of gearbox, which contain specifically temperature readings for gearbox bearing 1 (main speed shaft bearing connected to the rotor), gearbox bearing 2 (high speed shaft bearing connected to the electric generator) and the gearbox oil (the temperature of gearbox oil is close to actual gear temperature) and the pressure in the oil pump. The oil pressure shows the operating condition of the gearbox cooling system.

Monitoring and analysis of the vibration signals have been proven very effective, as it is easy to obtain the fault signature of a specific component in the frequency or time-frequency domains. However, it is difficult to obtain the accurate vibration signals in the wind turbine under varying speed operation. Furthermore, condition

monitoring based on vibration signals is a kind of component-specific technique, which lacks providing an inherent relationship between different subsystems

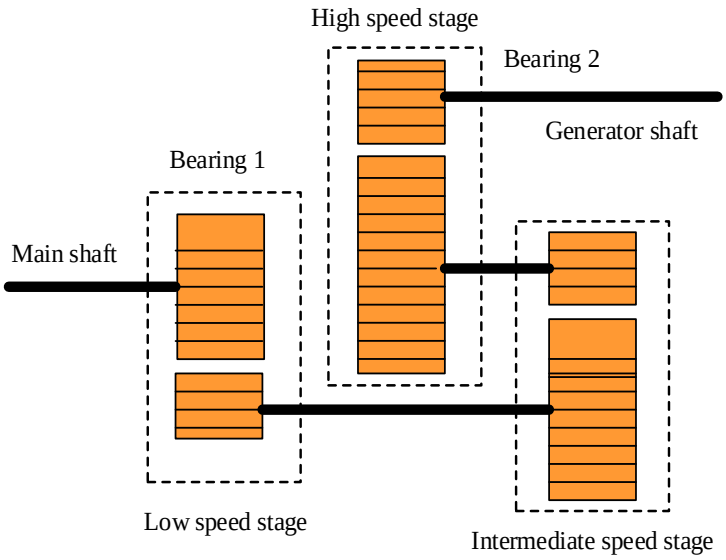

Figure 2.3 Schematic diagram of gearbox structure

From surveys concerning the reliability of wind turbine, the faults caused by drivetrain system account for over 20% of total faults and contribute to approximately 30% of the downtime of wind turbines in the doubly-fed wind turbine [15, 16]. Thus, the studies about fault diagnosis of the drivetrain system are necessary. Fig 2.2 shows a typical drivetrain and gearbox subsystem in a doubly-fed wind turbine that contains hub, main bearing, main shaft, gearbox, brake, generator shaft power converter and generator. The main function of drivetrain system is to transmit kinetic energy from the turbine rotor to the electric generator by adjusting rotational speed and torque.

2.2.1.3 Bearing

Bearings are extensively applied to various wind turbine components and subsystems, including generator, main shaft, gearbox, rotor, yaw system and pitch system. In recent year, using roller bearings instead of ball bearings is become a

trend. One of a typical fault of bearing is surface roughness of certain parts caused by using for long time, which will then develop into more serious fault. Meanwhile, the fault happened in bearings will induce different frequencies feature of the vibration.

2.2.1.4 Main shaft

The function of main shaft is to transfer the energy from the rotor to generator. The failure modes of the main shaft in the wind turbine include corrosion, crack, and misalignment. The fault of main shaft will reduce the power transmission efficiency and generate vibrations in generator, rotor and gearbox.

2.2.1.5 Hydraulic system

Generally, the hydraulic systems are used to delivery hydraulic power to blade pitch system or yaw system to adjust the angle of the blade or the yaw position in the wind turbine, in order to obtain the maximize power from the wind. Some kinds of fault, including oil leakage and sliding valve blockage can be detected by using oil pressure signals or oil level signals acquired from corresponding sensors.

2.2.1.6 Mechanical brake

In order to avoid the rotor over speed or make wind turbine stop in the condition of failures of key components, the mechanical brake is installed on high-speed shaft. Generally, the mechanical brake is consisted of three parts: a disc and calipers, a hydraulic mechanism system, and a three-phase AC motor. The disc of the mechanical brake will be subject to cracks caused by overheating, because the mechanical brake usually bears extreme high mechanical load. The faults of the mechanical brake can be diagnosed by using temperature signals, vibration signals, and electrical signals.

2.2.1.7 Tower

The corrosion and crack are two main faults in wind turbine structure damages, which are usually induced by a poor quality control during the manufacturing process, harsh environment, and fire disaster.

2.2.1.8 Electric machine

The detailed information of the wind turbine generator is illustrated in section 2.1 and table 2.1. Apart from the generator, the motors are also applied in pitch and yaw system. The failures of the electric machine are able to be classified into electrical faults (i.e. winding insulation damage, circuit short and open) and mechanical faults (i.e. bearing wearing, rotor mass imbalance, and air gap eccentricity).

2.2.1.9 Power electronic converter

With the rapid development of the wind turbine power rating, the reliability of the power electronic converter has been paid more attention. From the statistical data in [15], the failure of power electronic converter accounts for around 25% of the total failure in the whole wind turbine system, and the downtime caused by the fault of power electronic converter may reach approximately 14% of the total wind turbine downtime. There are three main reasons that cause the power electronic converter damage, including overheating, humid environment and vibration condition. The capacitor, printed circuit boards (PCB) and power switch (i.e. insulated gate bipolar transistor) are the three vulnerable components in the power electronic converter.

2.2.2 Nonlinear wind turbine model

2.2.2.1 Aerodynamics

For aerodynamics model, there are two main parameters, including the aerodynamic torque T_a and the thrust force F_t, which can be expressed as follow:

$$T_a = \frac{0.5\pi\rho R^2 v_r^3 C_p(v_r,\omega_r,\beta)}{\omega_r} \quad (2\text{-}1)$$

$$F_t = 0.5\rho R^2 v_r^2 C_t(v_r,\omega_r,\beta) \quad (2\text{-}2)$$

Where R is the length of the blade; ρ is the air density; $v_r$is the wind speed; C_p and C_t are the power coefficient and the thrust coefficient respectively.

2.2.2.2 Drive train

The drive train is a key component of the wind turbine, which is to transmit kinetic energy from the turbine rotor to the electric generator through the drivetrain system. J_r is the rotor inertia; J_g represents the generator inertia. One of the widely used drive train model is the single-mass model illustrated by low-speed shaft motion equation. Hence, the equivalent mass J_t can be gained by using equation (2-3).

$$J_t = J_r + N_g^2 J_g \quad (2\text{-}3)$$

Where N_g is the gear box ratio, then the relationship between the rotate speed of the rotor and the rotate speed of the generator can be expressed as follow:

$$\omega_r = \frac{1}{J_t}\left(T_a - N_g T_g\right) \quad (2\text{-}4)$$

$$\omega_g = N_g \omega_r \quad (2\text{-}5)$$

Then, the shaft torque T_s twisting the low-speed shaft is calculated by using equation (2-6).

$$T_s = \frac{N_g^2 J_g}{J_t} T_r + \frac{N_g J_r}{J_t} T_g \quad (2\text{-}6)$$

2.2.2.3 Generator

P_g^{cmd} is the reference power; T_g^{ref} is the reference electrical torque of the generator; T_g is the real electrical torque of the generator obtained from the wind turbine system.

$$T_g^{ref} = \frac{P_g^{cmd}}{\omega_g} \quad (2\text{-}7)$$

In wind turbine control system, the vector control is adopted in close-loop electrical torque control to make a fast and accurate feedback from the generator. If the control system normally operates, the real electrical torque of the generator T_g is almost close to the reference electrical torque of the generator T_g^{ref}.

$$T_g \approx T_g^{ref} \quad (2\text{-}8)$$

Then the generator power output P_g can be expressed as follow [34]:

$$P_g = \mu T_g \omega_g \quad (2\text{-}9)$$

2.2.2.4 Pitch actuator

Due to the inertia existing in pitch system, the pitch system model considering the inertia is established. The pitch angle β is adjusted by the gain-scheduled proportional-integral (PI) controller, which is based on difference between filtered actual generator speed ω_f and rated generator speed ω_{rated}.

$$\beta = -\frac{K_p}{K_c}\omega_f - \frac{K_i}{K_c}\left(\omega_f - \omega_{rated}\right) \quad (2\text{-}10)$$

Where K_p and K_i illustrate proportional and integral gain of the PI controller respectively; K_c represent the correction factor derived by equation (3-11).

$$K_c = f_{corr}\left(P_{ref}^{WT}(k-1), \beta(k-1)\right) \quad (2\text{-}11)$$

And the rotation angle range of the pitch angle β should be in a certain range described by equation (3-12).

$$-\Delta\beta_{max} \leq \beta \leq \Delta\beta_{max} \quad (2\text{-}12)$$

Where $\Delta\beta_{max}$ denotes maximum change rate of the pitch angle.

$$\omega_f = \frac{1}{\tau_g}\omega_g - \frac{1}{\tau_g}\omega_f \quad (2\text{-}13)$$

τ_g illustrates the time constant of the measurement filter for the generator speed ω_g.

2.2.3 Wind turbine faults

In order to analysis the failure events of the wind turbine, the data gained from a commercial wind farm in German is used, which contains 731 daily operational reports in 2011 and 2012 respectively. The data contains parameters of power generation, wind velocities, stoppage times caused by faults, and events and alarm logs of each wind turbine.

The percentage of failure events for each subsystem occurred in 2011 and 2012 are presented in Fig 2.4 respectively. It seems that the rotor accounts the largest percentage of failure events in 2011, reaching 44%. The gearbox, control system and converter have the almost same percentage of failure events, which are around 10%. In 2012, the percentage of failure events for each subsystem is similar to its in 2011. The above mentioned four subsystems have higher failure frequencies than the other subsystems.

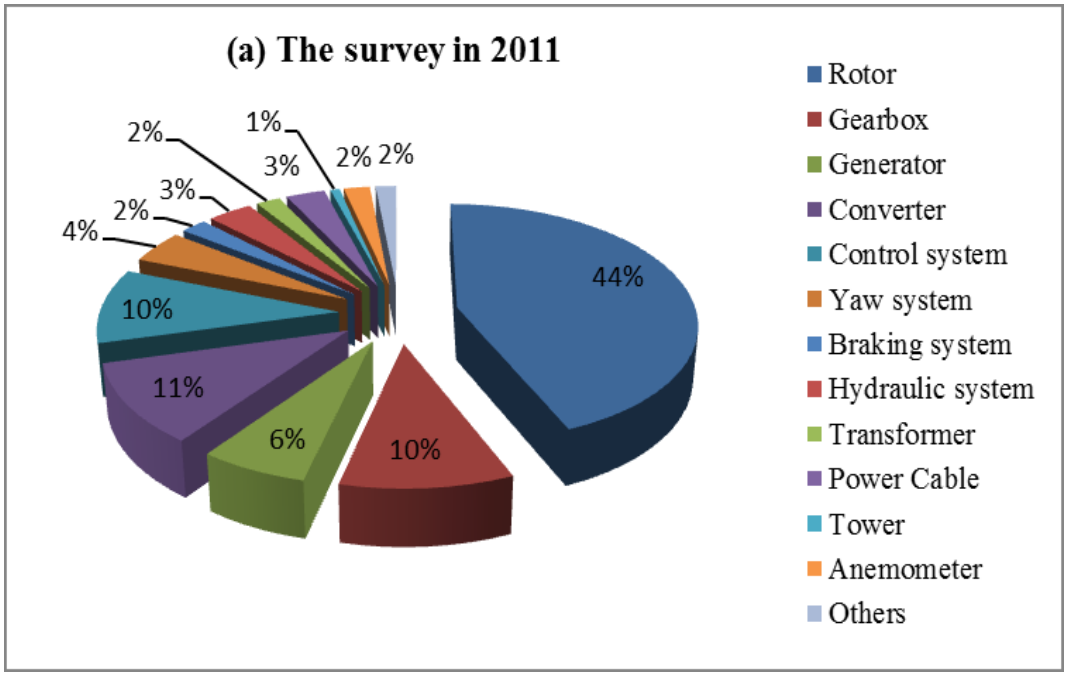

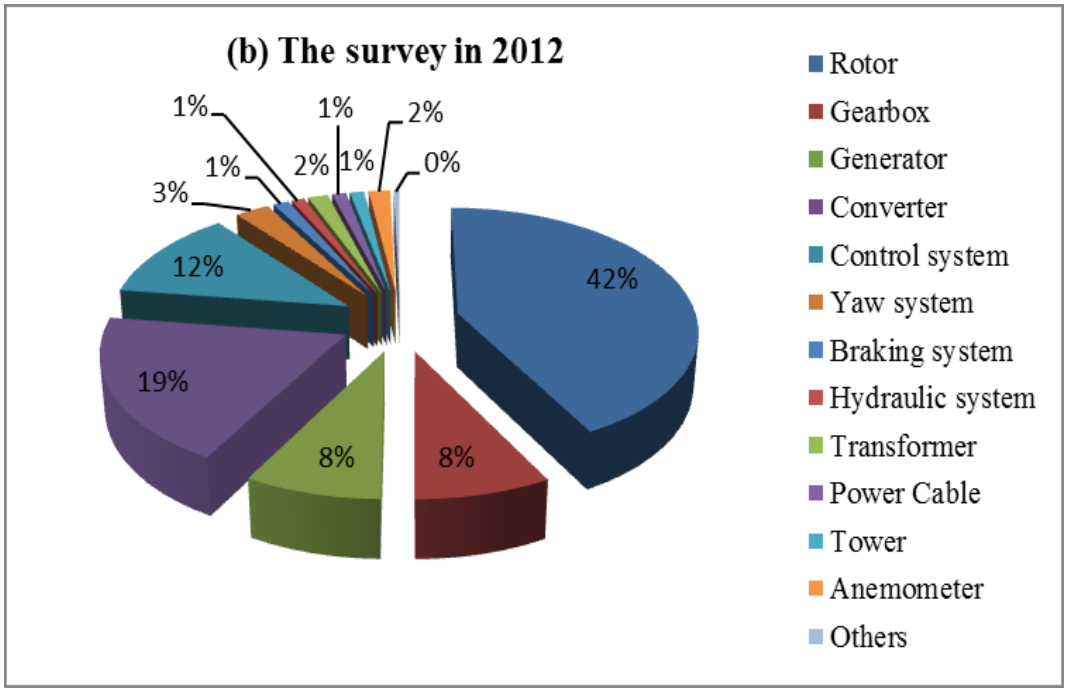

Figure 2.4 Percentage of failure events for each subsystem in two years [35]

WT subsystems	Components	Possible failures	Component or subsystem monitoring
Rotor	Blades	Deterioration, Cracking and adjustment error	Ultrasound and active thermography
	Bearings	Spalling, Wear, defect of bearing shells and rolling element	Vibration, OA, AE, SPM and performance monitoring
	Shaft	Fatigue and crack formation	Vibration
Drive Train	Main shaft bearing	Wear and high vibrations	Vibration, SPM, temperature and AE
	Mechanical Brake	Locking position	Temperature
	Gearbox	Wearing, fatigue, oil leakage, insufficient lubrication, braking in teeth, displacement and eccentricity of toothed wheels	Temperature, vibration, SPM, particles in oil and AE
Generator		Wearing, electrical problems, slip rigs, winding damage, rotor asymmetries, bar break, overheating and over speed.	Generated effects, temperature, vibration, SPM, OM.
Auxiliary Systems	Yaw System	Yaw motor problem, brake locked and gear problem	Motor current
	Pitch System	Pitch motor problem	OM
	Hydraulic System	Pump motor problems and oil leakage	OM, process parameter, performance monitoring
	Sensors	Broken and wrong indication	Thermography
Electrical System	Control System	short circuit, component fault and bad connection	Current consumption and temperature
	Power Electronics	short circuit, component fault and bad connection	Current consumption and temperature
	High Voltage	contamination and arcs	Arc guard, temperature
System transformer		Problem with contamination, breakers, disconnectors and isolators.	Thermography

OA - Oil analysis, AE - Acoustic Emission, SM – Strain Measurement, VI – Visual Inspection, SPM – Shock Pulse Method, OM – Operation and Maintenance

Table 2.2 Overview of possible failures and monitoring techniques for various wind turbine components and subsystem

2.3 Wind turbine condition monitoring

The condition monitoring system is used to monitor the change of the operating parameters in physical system [36-38]. The system failure can be diagnosed and

prognosed from the change of the operating parameters. The condition monitoring systems can be divided into two categories: offline condition monitoring system and online condition monitoring system. Compared with offline condition monitoring system, the online condition monitoring system has several advantages: firstly, the online condition monitoring system can operate when the wind turbines are operating. It means that this system is able to reduce power generation loss of wind turbines. It would therefore save the cost of wind farm operating. Secondly, the online condition monitoring system provides a deeper insight into health condition of wind turbine components and subsystems. It can alert the maintenance department to both long-term trends and short-term information, which is not able to be observed by the offline condition monitoring system. Thirdly, the online condition monitoring system can be integrated with SCADA system, which can automatically trigger appropriate alarms and maintenance schedule. This characteristic of the online condition monitoring system is very essential to some wind farms, especially in remote and harsh environment area.

2.3.1 Existing techniques

Actually, the signal processing technologies are the core parts in the condition monitoring system, which is used to extract features and transfer the data collected from the sensors into the format of the request. From previous research, the signal processing technologies used for condition monitoring of the wind turbine mainly include classical time-domain analysis methods, classical frequency analysis methods, classical time-frequency analysis methods, model-based methods, and probability-based methods [16].

2.3.1.1 Classical time-domain analysis methods

In classical time-domain analysis methods, there are three main methods, including statistical analysis, Hilbert transform, and envelope analysis. In the statistical

analysis methods, the time-domain signals from the healthy wind turbine, including statistical features (i.e. variance, crest factor, root mean-square value, and mean value), are selected as the base data for the condition monitoring systems [39]. Then, the same type of signals are monitored with time series during the wind turbine operation. Any deviations between the base data and online data that exceed the predetermined thresholds indicate faults occurred in the wind turbine.

Hilbert transform is another classical time-domain analysis method that is able to extract fault features from modulated signals [40]. When there is a fault in the wind turbine, the faulty component will induce the vibration of the component. The vibration of the component will modulate signals obtained from the sensors in the wind turbine. However, it is difficult to extract fault characteristic directly by using raw data due to the modulation of signals. Hilbert transform is considered one of effective demodulation method that has been used for signal demodulation in fault diagnosis of mechanical components, i.e. bearing, gearbox, and main shaft.

While envelope analysis is widely used in commercial wind turbine condition monitoring systems. Compared with Hilbert transform, envelope analysis is able to gain the envelope of a signal by combining with other amplitude demodulation methods. However, envelope of a signal is a kind of time-domain signal that needs to be further processed by other signal processing technologies.

2.3.1.2 Classical frequency analysis methods

Fast Fourier transform (FFT) analysis is the most extensively used frequency analysis method. FFT analysis can easily obtain the frequency spectrum of the signal in the digital system [41]. The fault happened in some components will induce the vibration with specific frequency in the frequency spectrum, which can be easily detected by using FFT analysis. FFT analysis is particularly applied in frequency spectrum analysis of acoustic emission signal and vibration signal. FFT analysis is also be used to analysis harmonic contents in the frequency spectra of the current and voltage signals that is associated with faults of the electrical

subsystem in the wind turbine. While the wind turbine generally operates with varying condition, so signals collected from the sensors are nonstationary signals. It is difficult for FFT analysis method to process the nonstationary signals during the wind turbine operation.

2.3.1.3 Classical time-frequency analysis methods

Classical time-frequency analysis methods combine the both advantages of time-domain analysis methods and frequency-domain analysis methods. Short-term Fourier transform (STFT) and wavelet transform are two types of the most widely used time-frequency analysis methods. A mean for analysing the time-varying frequency response of a nonstationary signal is able to be obtained by using STFT, which provides a three-dimensional signal that contains values of the time, frequency and amplitude. STFT method has been successfully applied in the fault diagnosis of the rotor, generator, gearbox, and structure damage. However, STFT method is incapable to simultaneously achieve high time resolution and high frequency resolution, because STFT method is a kind of the window-base method. Thus, STFT method is difficult to achieve the frequency analysis of nonstationary signals with high sampling frequency.

Beside STFT method, the other classical time-frequency analysis method is wavelet transform method. Essentially, wavelet transform method is able to hierarchically decompose a signal into a set of frequency channels that have the same bandwidth on a logarithmic scale [42, 43]. Because of this characteristic, wavelet transform method has an ability to extract the signal feature from both the time-domain and frequency-domain. However, wavelet transform method has the same disadvantage with STFT, it cannot achieve the frequency analysis of nonstationary signals with high sampling frequency.

2.3.1.4 Probability-based methods

Bayesian methods are kinds of classical probability-based techniques that is appropriate for applying in the field of the real-time state prediction. Generally, a process of a Bayesian prediction is consisted with two operations recursively [44], including propagation and update. In order to obtain the better prediction result, a recursive Bayesian algorithm based on the concept of sequential importance sampling and the Bayesian theorem is proposed, which has been used for the fault diagnosis of the blade and bearing in the wind turbine. However, the number of prior tests and the size of data samples will significantly affect the prediction accuracy of Bayesian methods. This disadvantage of Bayesian methods limits its application in industrial field.

2.3.1.5 Model-based methods

In the model-based condition monitoring system, the establishment of the accurate prediction model is the key step, which is used to simulate the dynamic behaviours of components and subsystems in the wind turbine. Generally, the wind speed and power output are selected as input signals for prediction model [45]. Then, actual output signals are compared with the signals that are predicted by the model for given input signals. Differences between actual output signals and the model predicting signals could be caused by changes in the process, possibly due to the occurrence of faults. The establishment of the prediction model has three main methods, including mathematical model, and data-driven method.

The mathematical model is established based on the physical principle. Adopting mathematical model for predication requires a thorough understanding of about physical structure and mathematical relationship of models. It is difficult to be obtained for complex or nonlinear system. Moreover, the mathematical model applied in the model-based condition monitoring system is not suitable for on-line implementation. The data-based model method does not require the detailed information about physical structure and mathematical relationship. Input signals for the data-based model can obtained directly from measured signals that are

collected from planned experiments or real-time online data during system operation.

Compared with above mentioned methods, the signal sampling rate for the model-based methods do not need to be very high. Therefore, there is no needs for addition high performance sensors in condition monitoring system, which is able to significantly reduce the cost and complexity of the system. Moreover, the computation load of the above mentioned methods is very high, resulting in limitation of the industrial application. The other advantage of the model-based condition monitoring is that it can detect some non-negligible changes in the model output caused by an even small damage of the component in the wind turbine. Thus, the model-based methods are suitable to be used to diagnose of faults in an early and monitor the development of the faults. Although the model-based methods has an ability to diagnose the faults occurred in the wind turbine, it is difficult to provide the detail information of faulting, i.e. the location and fault degree. Furthermore, accuracy of the model-based methods is depend on the prediction model, however, the accurate mathematical model for some complex system is usually difficult to obtain in real-world applications.

.

2.3.2 AI techniques in model-based methods

For data-based condition monitoring systems, accurate models are essential for the relationships between those parameters being monitored. In this regard, artificial intelligence (AI) techniques are utilized by many researchers for data-based CM schemes, such as artificial neural networks (ANNs) [46], support vector machines (SVMs) [47] and fuzzy logic [48]. ANN-based methods require little or even no knowledge about the physical principle of the model. ANN-based methods have two functions in condition monitoring of the wind turbine, including prediction and classification. In the behavior prediction, the reference data of the wind turbine obtained from the database is selected as training data for ANN-based methods. After training process, ANN-based methods are then used to predict the operation

performance of the wind turbine or its subsystem. Then, actual output signals are compared with the signals that are predicted by the model for given input signals. Differences between actual output signals and the model predicting signals could be caused by changes in the process, possibly due to the occurrence of faults. Besides the prediction function, ANN-based methods are also able to be used to recognize the fault categories of the wind turbine subsystem from the input signals that contain the information of faults. ANN-based methods are robust to signal noise, making them suitable for dealing with data acquired in noisy environments. However, the long training times associated with ANN models can limit their application.

Support vector machines (SVMs) are another data-driven techniques that tend to have better generalized performance and more accurate training results than ANN-based methods. SVM methods are generally applied in the condition monitoring of gearbox, generator, bearing and main shaft in the wind turbine. However, training SVM models with large datasets is not straightforward.

Expert systems are rule-based techniques that are able to construct a mapping associated with measurements of the health condition of the wind turbine. Then, expert systems can achieve the fault diagnosis by reasoning with new measurements. But expert systems also have their own disadvantages, they have the same shortcomings of other heuristic methods. One of the main disadvantage of expert systems is that the size of the prediction model will increase exponentially with the number of the fault model raising, which will significantly increase the computational load and cost.

Fuzzy logic systems, based on fuzzy sets of linguistic variables, use predefined rules to enable reasoning. Fuzzy logic systems are based upon fuzzified features of the faults and then use these features to diagnose faults by using the predefined rules. It is clear that fuzzy logic systems require full knowledge of failure mechanisms of a wind turbine in order to design these rules, which is usually unfeasible in practice. If the designment of rules is not accurate enough, the prediction results will also be false. Furthermore, fuzzy logic systems also have the

same disadvantage with expert systems.

In this thesis, an extreme learning machine (ELM) algorithm [49-51] is employed to train a neural network model for data-based condition monitoring, overcoming the drawbacks of a traditional feedforward ANN. The prediction model is established by using ELM algorithm, the actual data collected from real wind turbine is compared with prediction signal. Any difference means that there are some faults happening in the wind turbine.

2.3.3 Signal types for wind turbine condition monitoring

The faults occurring in wind turbines can be divided into two types: the temporary random faults and the wear-out failures. There are many types of signals can be used in condition monitoring systems, including current, voltage, temperature, strain, vibration, oil pressure, acoustic emission (AE) and torque.

2.3.3.1 Vibration signals

Many faults happing in wind turbines usually induce the vibration of the corresponding components and subsystems, which can be easily detected by vibration sensors. Vibration monitoring technology is one of widely used condition monitoring method in commercial wind turbine condition monitoring system. Vibration sensors are usually installed on blade surface, main shaft and bearing, gearbox and generator [52]. There are three types of vibration sensors, including displacement sensors, accelerometers, and velocity sensors. Their operating frequencies normally arrange from 1 Hz to 30 kHz. However, the signal-to-noise ratio of vibration signal is low when it is used to diagnose the incipient faults. It means that vibration signal is easy to be disturbed.

2.3.3.2 Temperature signals

The temperature signal based condition monitoring technique is considered as one of the cost effective and reliable method in condition monitoring of wind turbines. It has been applied for fault detection of the generator, gearbox, main bearing and power electronic device. In normal operating conditions, the temperature of components or subsystems in a wind turbine is below certain values. When an abnormal temperature rising happens in wind turbine components or subsystems, it can be caused by a degradation of some components or subsystems. As a mature technique, temperature signals are able to provide useful information on the health condition of the wind turbine. However, the temperature signal based condition monitoring system has its drawbacks. Essentially, there are many factors that may cause the abnormal temperature increasing occurring in the wind turbine, which make it difficult to identify the accurate reasons of the abnormal temperature increasing. Therefore, the abnormal temperature rising in the wind turbine can just only indicate a possible fault happening, but it can't accurately indicate which component has a fault.

2.3.3.3 Acoustic emission signals

When materials bear external strain or stress, they may generate sound waves called acoustic emission (AE). Even a tiny structural change will make AE signals to be excited, it means that AE signal is very suitable to be applied in incipient structure defecting or monitoring its development. In wind turbine condition monitoring system, AE signals are generally used for fault detection of the blade, gearbox, bearing, and generator. Compared with vibration signals, AE signals have high signal-to-noise ratio for condition monitoring, which means that AE signals is able to be applied in high-noise environments. However, AE technique also has its own disadvantages in wind turbine condition monitoring system. In order to monitor subsystems of the wind turbine, it is necessary to install a large number of AE sensors, and each sensor requires an independent data acquisition system for signal sensing, processing and transferring, which may increases the cost and complexity

of the wind turbine condition monitoring system.

2.3.3.4 Torque signals

Torque based condition monitoring technique is usually applied in generator and drive train. It can detect faults when there is an axle to be turned around or bending moment tends in the shaft. Torque signals are obtained by using rotary torque sensors or reaction torque sensors. Apart from using for condition monitoring, the torque signals are also used to calculate the electrical power output from the generator. The disadvantage of torque signals is similar to vibration signals. However, a relevant torque signal for faulty component is a kind of modulated signal with the dominant components associated with the load, which makes signal processing for torque signals more complicated than using vibration signals.

2.3.3.5 Electrical signals

Voltage and current are types of widely used electrical signals collected from the terminals of the generator and power electronics device in the wind turbine, and therefore extensively applied in diagnosis of the power converter and generator faults. Electrical signals based condition monitoring technique has been paid more attention in recent years, because of its advantage. Collecting electrical signals doesn't need additional sensors and data acquisition devices, because these electrical signals can be obtained from the wind turbine control and protection systems, which means that electrical signal based condition monitoring system requires no additional cost. Furthermore, electrical signals are reliable and not easy to be disturbed by high-noise environments.

2.4 Summary and discussion

In this chapter, the four type of wind turbines and their subsystems have been reviewed. Additionally, this review also covers the importance of condition monitoring of the wind turbine system that is considered as the best solution for improving the wind turbine reliability. In order to have a better understanding of the condition monitoring of the wind turbine, the detailed information about structure of DFIG wind turbine, including mathematical model of each subsystem, is described. Then, the advantage and disadvantage of the existing techniques for wind turbine condition monitoring are presented. In this thesis, the model-based method based on data-drive technique is adopted, the review of AI techniques in model-based methods is therefore described. In previous research, the training time of machine learning method is often too long, which limits its industrial application. This chapter is focus on the wind turbine technology, and the introduction of power grid related technology is given in next chapter.

Chapter3. Study of active power filter and power dispatch strategy

This chapter illustrates the study of active power filter and power dispatch strategy. The detailed introductions of optimizing wind farm power output strategy, including active power and frequency control, reactive power and voltage control, and power dispatch strategy, are given. Thereafter, the active power filter technology and harmonic pollution related problem are described. Finally, the SCADA data collected from a commercial wind farm is illustrated.

3.1 Optimizing wind farm power output strategy

3.1.1 Active power and frequency control

With the rapid increasing installation of wind turbines, the penetration level of the wind power becomes very high. Hence, the network operator issues a more stringent technical requirements for wind farm control [53], especially for active power control. More specifically, there are some different types of active power control strategies, including baseline mode (maximum power point tracking mode MPPT), de-rated mode, delta mode and percentage mode [34, 54, 55].

The active power generated by wind turbines should be in balance with the load demand and power loss in power grid. When produced active power is more than the load demand and power loss, it will cause generator rotate speed rising, and corresponding to the frequency of power grid increasing. Meanwhile, if the generation of active power is not enough, the frequency of power grid will also decrease [56, 57].

The droop control strategy is widely used in renewable energy system [58-60], as shown in Fig. 3.1. The frequency control can be fast achieved by using the primary control illustrated in with the solid line in Fig. 3.1. It is able to maintain the balance between the power generation and load demand. The dashed lines shown in Fig. 3.1 illustrate alternative setting for droop control strategy, which is called the secondary control. Compared with the primary control, the response speed of the secondary control is slower than the primary control. Generally, the power dispatch centre uses the secondary control to control the power distribution of the power generation between different power plants.

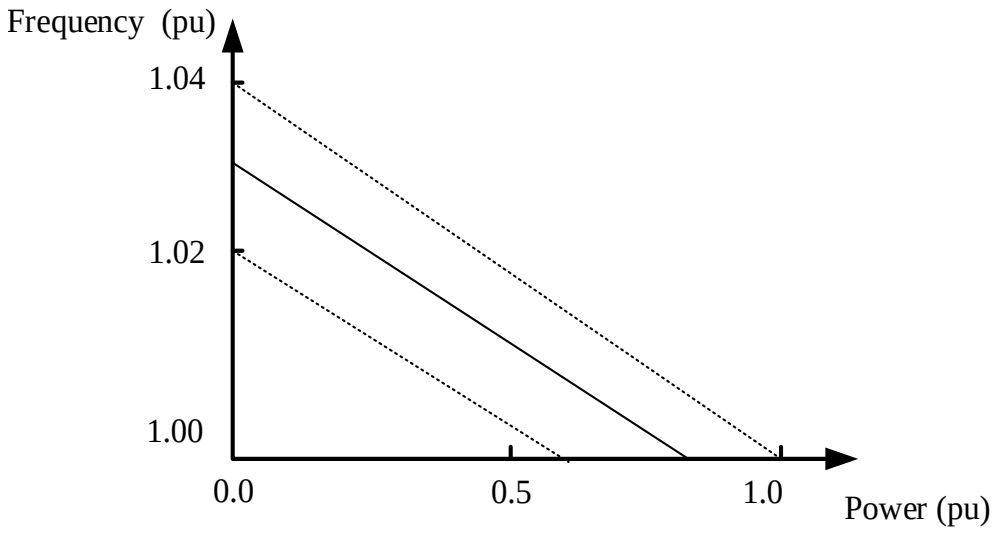

Figure 3.1 The diagram of the droop control

The frequency changes with the active power generation at a liner trend. A falling frequency indicates a load increasing and a demand for more active power generation. Multiple parallel dash lines with the same droop characteristic can respond to the rise in frequency by decreasing their active power outputs simultaneously. The sudden changes in renewable power generations could cause frequency oscillation and other reliability related problem in the power grid. So, the power ramp rate of the secondary control should be specified by network operators. In order to support the primacy control, a dead-band for droop control should be set. Wind turbines usually participate in both the primacy control and the secondary control in the wind farm. However, the switch between the primacy control and the secondary control will cause loss of wind power generation.

3.1.2 Reactive power and voltage control

Reactive power and voltage control are strongly associated with the wind farm control system, due to the strong coupling between the reactive power flow and the

voltage changes in the power grid. The relationship between reactive power and voltage can be expressed as follow:

$$\Delta V = \frac{R \cdot P + X \cdot Q}{V} \quad (3\text{-}1)$$

Where ΔV is the voltage change caused by reactive power fluctuation; V is the voltage of the power grid; P and Q are the active power and reactive power respectively; R and X are the transmission line with serial line resistance and reactance respectively.

In real world, the value of the transmission line with serial line reactance X is much higher than the value of the transmission line with serial line resistance R. In that case, the voltage of the power grid is mainly determined by reactive power.

3.1.3 Power dispatch strategy

Power curves of two wind turbines, obtained from the SCADA data from a commercial wind farm, are shown in Fig 3.2. Fig 3.2 illustrates a power curve of a healthy turbine. It can be seen that power varies with the cube of wind speed below the rated speed of 15 m/s. When the wind speed is below the cut-in speed of 4 m/s, the rotor torque is not sufficient for the turbine to produce any power. When the speed of the wind is greater than the cut-out speed of 25 m/s, the turbine is shut down and does not generate any power. At wind speeds above the rated speed but below the cut-out speed, power output is restricted to the rated power of the turbine.

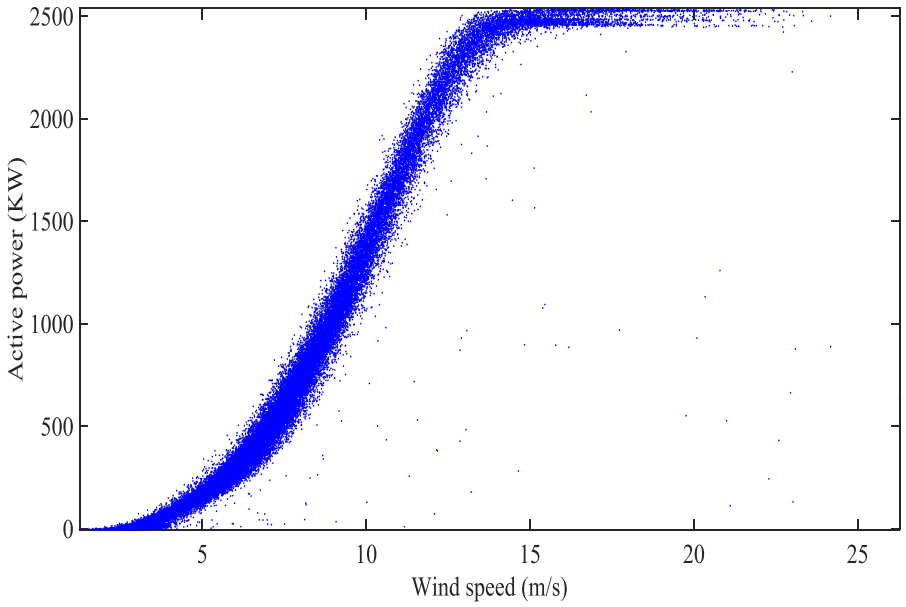

Figure 3.2 Power curve of the fault-free wind turbine

Generally, the wind power curve for wind turbines has two types of fundamental method for approximating [61, 62]. The first one is the stepwise linear profile model illustrated in (3-2).

$$P_{wind} = \begin{cases} 0 & v \le v_{in}\ ,\ v_{out} \le v \\ av + b & v_{in} < v < v_r \\ P_{max} & v_r \le v < v_{out} \end{cases} \tag{3-2}$$

Where v_{in} and v_{out} are the wind speed of the cut in and cut out for wind turbines respectively. v_{in} is the rate wind speed for wind turbines. *a* and *b* are the slope and the intercept parameters of the function.

While the second one is Weibull cumulative distribution function profile [61] that is applied in this paper. Thus, the wind power curve can be shown in (3-3).

$$P_{wind} = \begin{cases} 0 & v \le v_{in}\ ,\ v_{out} \le v \\ P_{max}\left(1 - e^{-\left(\frac{v}{c}\right)^k}\right) & v_{in} < v < v_r \\ P_{max} & v_r \le v < v_{out} \end{cases} \tag{3-3}$$

Where *k* and *c* are shape and scale parameters of the Weibull distribution, which is used to make the shape of Weibull cumulative distribution function profile similar to the wind power curve.

Wind farm control scheme is designed to make wind farm steady operation by using a separate energy storage system or through de-rated operation of wind turbines. But utilization of a separate energy storage system is impossible to apply in a large wind farm, due to high maintenance cost and capital investment of the separate energy storage system. Thus, a de-rated operation wind farm control system is a practical solution. Generally, power demand from the network operator is less than the maximum available power. Fig. 3.3 compares different wind turbine power reserve strategy as a function of wind speed [63-66]. The baseline of power output is obtained via using equation (3-3). In this figure, there are four wind turbine operation modes, i.e., baseline mode (MPPT mode), de-rated mode, delta mode and percentage mode. In MPPT mode, the wind turbine tries to capture the maximum power from the wind until it arrives the rated power. If the wind speed is above the rated wind speed but below the cut-out speed, the turbine's output power is capped at the rated power; the de-rate mode is almost the same as baseline mode, but it limits the maximum rated power production to meet wind farm requirements (80% in this case); the percentage mode keeps the constant percentage power reserve of the baseline mode (80% in this case); the delta mode means wind power production needs to be lower than the available power by a given amount of the baseline mode (500KW in this case).

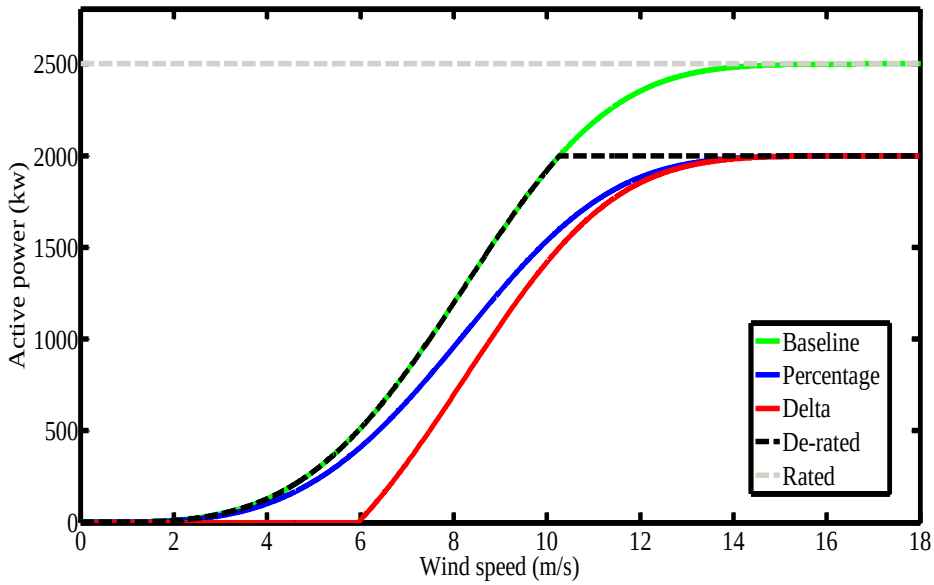

Figure 3.3 Comparison of different wind turbine power reserve strategies as a function of wind speed.

3.2 Active power filter

3.2.1 Harmonic pollution

In the power system, the ideal waves of the current and voltage are sine wave. Actually, the waves of the current and voltage will distort, due to the influence of harmonics. Harmonics will cause abnormal temperature rising and torque ripple in wind turbine generator, which reduces reliability and lifetime of the wind power system [67]. Some definitions of harmonics are given as follow:

$$U_H = \sqrt{\sum_{n=2}^{\infty} U_n^2} \tag{3-4}$$

Where U_H is voltage harmonic content; U_n is each voltage harmonic component.

$$I_H = \sqrt{\sum_{n=2}^{\infty} I_n^2} \tag{3-5}$$

Where I_H is current harmonic content; I_n is each current harmonic component.

$$HRU_n = \frac{U_n}{U_1} \times 100\% \quad (3\text{-}6)$$

HRU_n is the distortion rate of voltage; U_1 is the fundamental voltage.

$$HRI_n = \frac{I_n}{I_1} \times 100\% \quad (3\text{-}7)$$

HRI_n is the distortion rate of current; I_1 is the fundamental current.

$$THD_u = \frac{U_H}{U_1} \times 100\% \quad (3\text{-}8)$$

THD_u is total harmonic distortion of the voltage.

$$THD_i = \frac{I_H}{I_1} \times 100\% \quad (3\text{-}9)$$

THD_i is total harmonic distortion of the current.

From previous research, there are three main sources that generate harmonics in power system.

1) Harmonics generated from the power generator

The power generator will generate harmonics during operating, because there are some manufacture errors in the iron core and winding of generator

2) Harmonics produced by the power transmission and distribution system

The transformer is the key harmonic source in the power transmission and distribution system. When the iron core of the transformer is in the saturation condition, the magnetizing curve will present a nonlinear condition. It means that a large number of harmonics might produce during this stage.

3) Harmonics caused by the nonlinear load

With the development of the renewable energy system, a mass of power electronic devices are applied in the power system. Power electronic device is a kind of typical nonlinear load. The power electronic device will absorb sine wave from the power

grid, while incomplete sine wave will be left in the power grid. This problem causes a larger number of harmonics occurring in the power system.

3.2.2 APF classification

At present, harmonic-related problems have become more serious because of the widespread application of nonlinear loads in human's daily life. Active power filter (APF), as an effective technical method to solve the problem of harmonic pollution, has obtained great concern. Especially the high voltage, large capacity APF, has become a hot spot in today's power quality management, due to its more extensive applications. As mentioned above in section 3.2.1, there are two types of harmonics, i.e. voltage harmonic and current harmonic. In real world, most of harmonic pollution is caused by current harmonic due to use of the nonlinear loads. The voltage harmonic is caused by power generators, which is less serious than current harmonic.

3.2.2.1 The passive power filter

In order to solve this problem, adopting the power filter is the best solution to eliminate harmonics in the power grid. The power filter could be divided into two categories: the passive power filter and active power filter. The passive power filter, shown in Fig. 3.4, is consisted of the electric reactor, resistor, and capacitor. However, the values of the electric reactor, resistor, and capacitor are fixed, which means that a passive power filter can just filter the constant frequency harmonic. According to the regulation of harmonic frequency, the passive power filter could be divided into monotonous filter, more tuned filter, and C type filter.

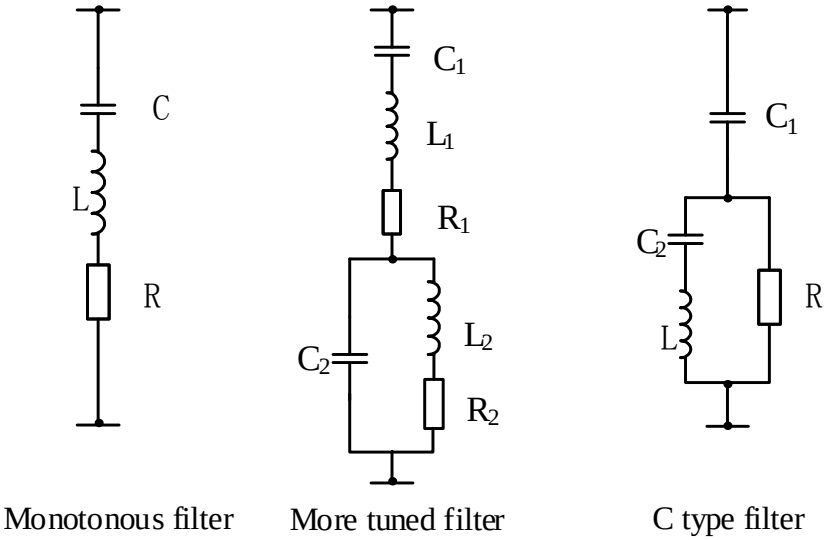

Figure 3.4 The structure of three types of passive power filters

3.2.2.2 The active power filter

Compared with the passive power filter, the active power filter is a more effective method. The active power filter is able to dynamically compensate various frequency harmonics [68]. Furthermore, the operation effect of the active power filter does not influence by the power grid impedance.

The shunt active power filter, shown in Fig 3.5, is usually adopted to eliminate current harmonic generated by the nonlinear load. Besides eliminating current harmonic, the shunt active power filter is also able to compensate reactive current and zero-sequence current in the power grid.

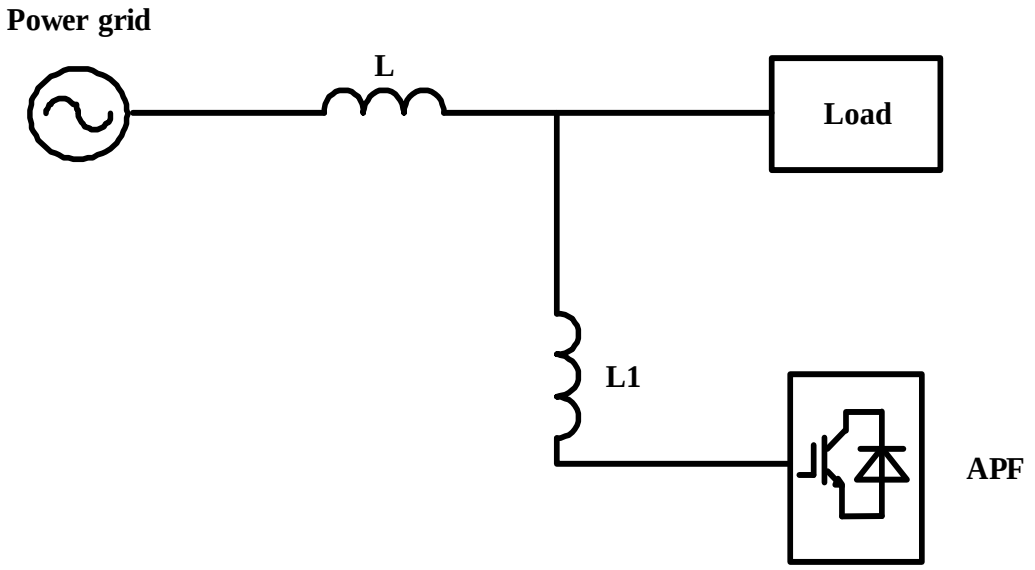

Figure 3.5 The structure of shunt active power filter

The series active power filter, shown in Fig 3.6, is usually adopted to eliminate voltage harmonic from the power grid. The series active power filter is in series the power grid by using the coupling transformer.

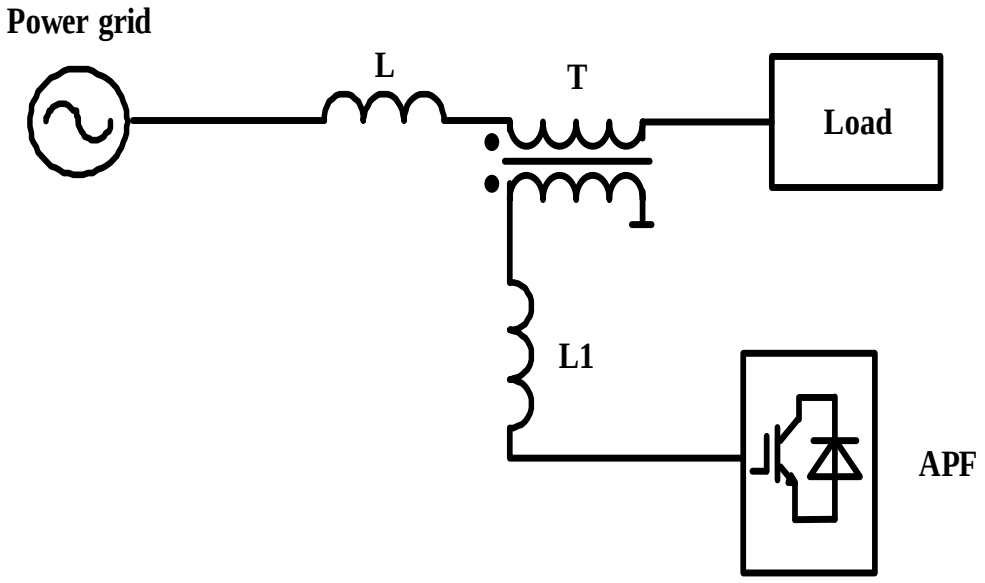

Figure 3.6 The structure of series active power filter

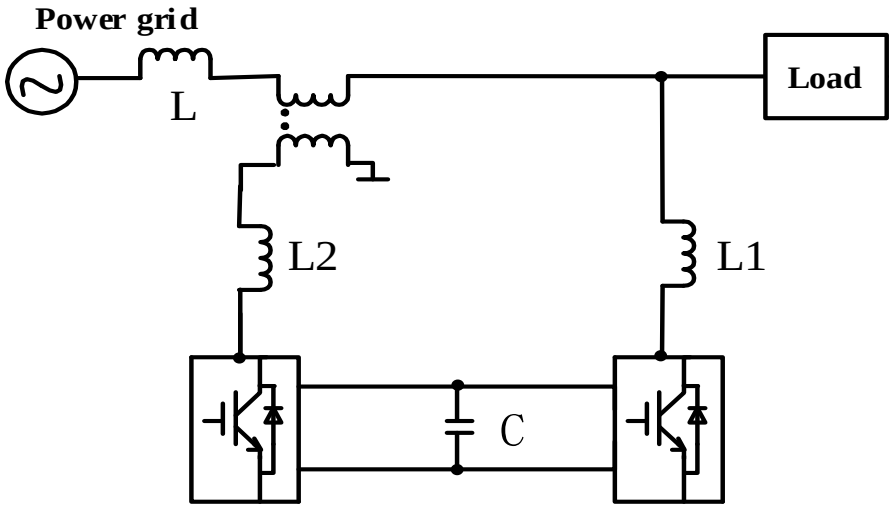

Figure 3.7 The structure of unified power quality controller

The unified power quality controller, shown in Fig 3.7, is consisted by both the shunt active power filter and series active power filter, which is adopted to eliminate both current and voltage harmonics in the power grid.

In this thesis, the research work is only focus on the current harmonic detection and current harmonic elimination. Because the current harmonic related problem is more serious in the wind farm. Fig 3.8 illustrates the schematic diagram of shunt active power filter that is used to eliminate current harmonic in real time. Generally, shunt APF is consisted of four parts, including harmonic detection circuit, control circuit, drive circuit, and main circuit. The harmonic detection circuit collects the current signals from the power grid to analysis the harmonic component of the current. When the harmonic component of the current is obtained, the reference compensating current is therefore determined i_c^* that is then used as the input signal of the control circuit. In order to transfer reference compensating current to PWM signal [69], space voltage vector pulse-width modulation (SVPWM) function is realized by the control circuit [70]. The main circuit is directly connected to the power grid, so the drive circuit amplifies the PWM signal to drive the main circuit.

The drive circuit can make high voltage part and low voltage part isolation, which enhances the reliability of APF. The main circuit normally adopts a voltage type inverter which generates compensating current to eliminate current harmonic in the power grid.

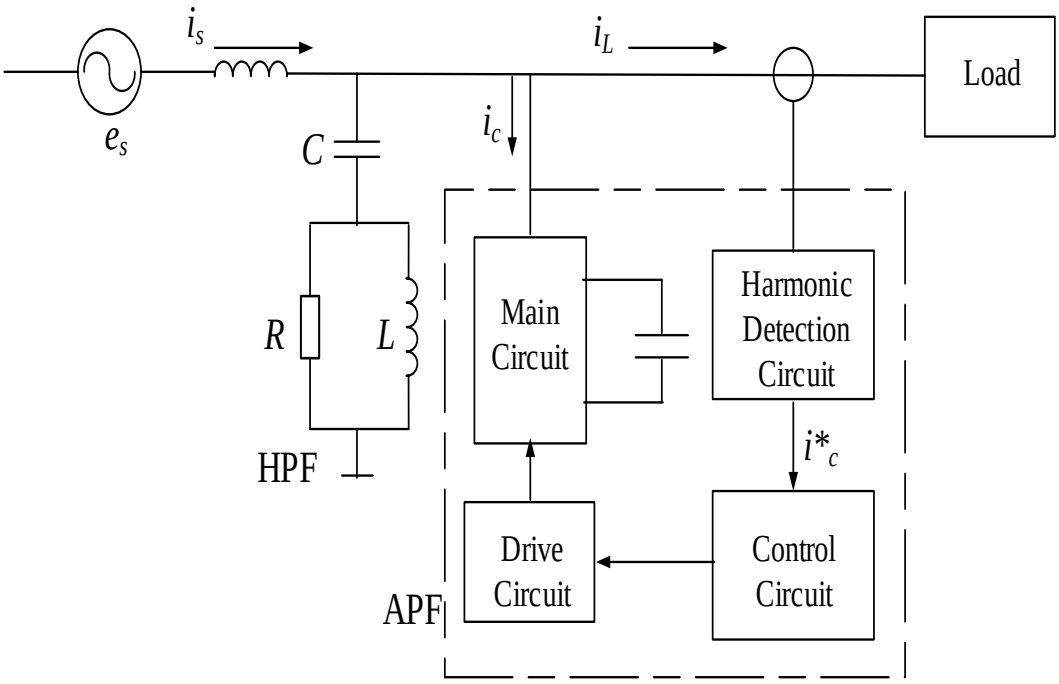

Figure 3.8 Schematic diagram of shunt active power filter

3.2.3 Harmonic detection

The harmonic detection technology is the key component in SAPF system, which is used to obtain accurate harmonic currents in three phrase power grid. The harmonic detection method based on the instantaneous reactive power theory is one of the most widely used technique applied in SAPF. Compared with traditional fast Fourier transform (FFT) method, the harmonic detection method based on the instantaneous reactive power theory is able to not only detect harmonic accurately, but also obtain zero sequence current in power grid.

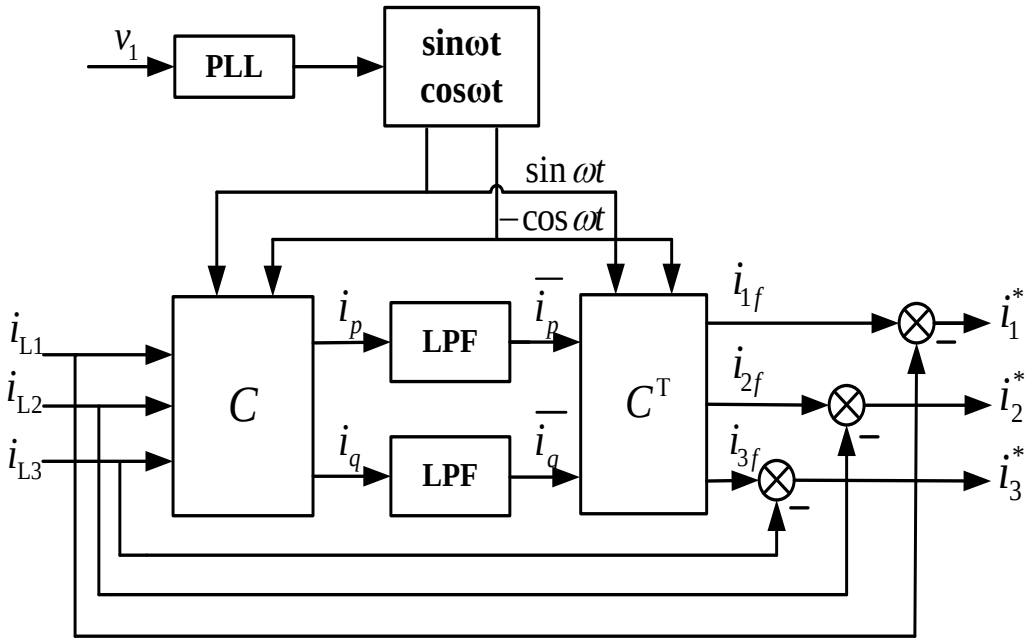

Figure 3.9 Schematic diagram of the harmonic detection method based on the instantaneous reactive power theory

$$C = \begin{pmatrix} sin\omega t & -cos\omega t \\ -cos\omega t & -sin\omega t \end{pmatrix} C_{\alpha\beta} \tag{3-10}$$

$$C_{\alpha\beta} = \sqrt{\frac{2}{3}} \begin{pmatrix} 1 & -\frac{1}{2} & -\frac{1}{2} \\ 0 & \frac{\sqrt{3}}{2} & -\frac{\sqrt{3}}{2} \end{pmatrix} \tag{3-11}$$

Fig 3.9 shows the schematic diagram of the harmonic detection method based on the instantaneous reactive power theory. The A phase voltage v_1 is processed by the phase-locked loop (PLL), and the corresponding $sin\omega t$ and $cos\omega t$ signals are then obtained. Three phrase currents i_{L1}, i_{L2}, and i_{L3} collected from the power grid are transferred to Clark transform unit described in equation (3-10) and (3-31). Active current $i_p$and reactive current i_q then pass through the low pass filter (LPF) to gain the filtered active current $i_{\bar{p}}$and reactive current $i_{\bar{q}}$. The harmonic current components can then be obtained by using reverse Clark transform.

3.3 SCADA data

Supervisory control and data acquisition (SCADA) systems utilize hardware and software elements and IT technologies to monitor, gather, and process data. In the power systems, SCADA systems are used for a range of functions, including data acquisition, control, adjustment of parameters, and generating warning signals. The SCADA systems allows information exchange between the wind farm and the remote monitoring and control centre. By two-channel information transmission channels, the remote monitoring and control centre is able to receive signals collected from sensors and make decision on control strategy. The sampling rate of SCADA system usually is usually below 0.002 Hz, i.e. data is sampled every 5-10 minutes. However, the data processing method of the signals will affect the sampling result.

The SCADA data used here have been obtained from a working wind farm. The use of operational SCADA data is an effective way to demonstrate the algorithms described in this thesis. These data represent 12 months' operation and consist of 128 variables, comprising temperatures, pressures, vibrations, power outputs, wind speed, and digital control signals. Note that SCADA signals are usually processed and stored at 10 minute intervals, although sampled in the order of 2 s.

3.4 Summary and discussion

In this chapter, optimizing wind farm power output strategy is illustrated. In power output strategy, active power control is used to keep the voltage frequency stable, while the reactive power control makes voltage of the power grid in reasonable fluctuation interval. Then, the background information of harmonic related problem is described. Active power filter classification and harmonic detection technology are detailed introduced. Finally, the SCADA data collected from a commercial wind farm is illustrated. In next chapter, the proposed condition monitoring method is

presented. Validation of the proposed algorithms will be carried out by using SCADA data.

Chapter4. Condition Monitoring of Wind Turbines based on Extreme Learning Machine

Condition Monitoring (CM) has been considered as an effective method to enhance the reliability of wind turbines and implement cost-effective maintenance. Thus, adopting an efficient condition monitoring approach of wind turbines is desirable. This chapter presents a model-based CM approach for wind turbines based on the extreme learning machine (ELM) algorithm. In order to solve the arbitrary values assignment problem, the weights of the inputs and the biases of the hidden neurons of the ELM model are optimized by the genetic algorithm (GA). Models have been validated from supervisory control and data acquisition (SCADA) data acquired from an operational wind farm, which contains various types of temperature and pressure data of the gearbox. The results show that the proposed method can more efficiently detect faults of the gearbox.

4.1 Model-based condition monitoring system

Wind farms are usually built in remote locations on land or offshore, which causes that wind turbines are normally subject to harsh weather. Thus, the routine maintenance and inspection of wind turbines are always difficult to be implemented. Over an operating life of 20 years, maintenance costs of wind farm may reach 15% and 30% of the total income for onshore and offshore wind farms, respectively [71]. Condition monitoring (CM) is considered an effective method to schedule cost-effective maintenance activities and enhances the reliability of wind turbines [6, 72, 73]. Consequently, it is essential to develop effective CM techniques for wind turbine, providing information regarding the past and current condition of wind turbines and to enable the optimal scheduling of maintenance task.

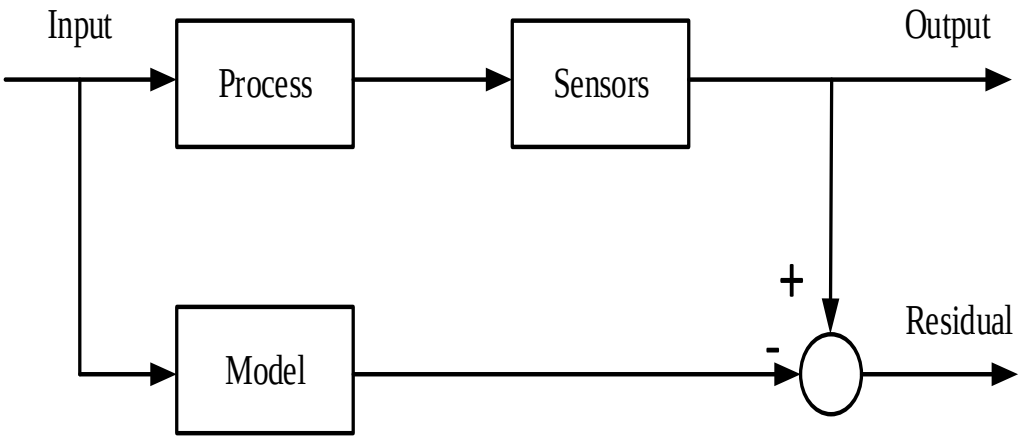

Figure 4.1 Schematic diagram of model-based condition monitoring system

Fig 4.1 shows the schematic diagram of model-based condition monitoring approach where the data generated from condition monitoring system or equivalents are used as inputs using models to predict the output signals of a physical process. Then, actual output signals are compared with the signals that are

predicted by the model for given input signals. Differences between actual output signals and the model predicting signals could be caused by changes in the process, possibly due to the occurrence of faults [14]. The wind speed and power generation are usually selected as input data, and the output is the prediction signal. The residual signal can be an important indicator to provide an early warning of impending component failure. Reasonable maintenance strategies can therefore be implemented, which can significantly reduce the maintenance cost and enhance the availability and reliability of a wind turbine [74].

4.2 Methodology

4.2.1. Artificial neural network

An artificial neural network (ANN) is a kind of computational supervised learning model, which has been widely used in many fields, including mode recognition and state prediction [75, 76]. Among numerous ANN methods, a single hidden-layer feed forward neural network (SLFN) using gradient-based back-propagation (BP) training algorithm is one of the most classic ANN method for the SLFN. It is usually selected as standard of comparison for estimating performance of other ANN methods.

Fig 4.2 shows a diagram of a feed forward neural network with a single hidden-layer. The network consists of an input layer, a hidden layer and an output layer of neurons. For this example, the input layer has n neurons; the hidden layer has L neurons, and the output layer has m neurons. Finally, x_1, x_2, $\cdots$, x_n are the inputs to the network and y_1, y_2, $\cdots$, y_m are the outputs from the network.

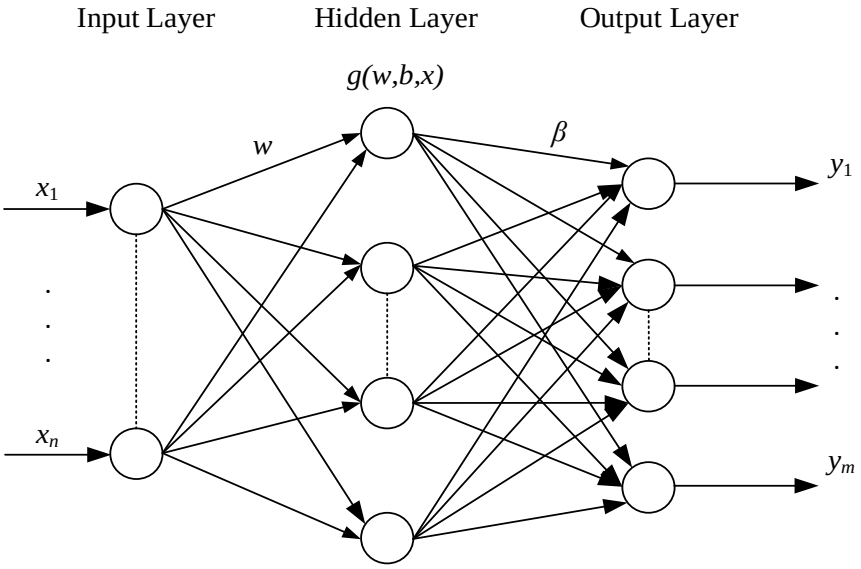

Figure 4.2 Schematic diagram of the SLFN structure.

For the gradient-based BP training algorithm forward calculation, the gradient-based BP training algorithm can be described as follow:

$$Y(t) = [y_1 \quad y_2 \quad \cdots \quad y_m] \tag{4-1}$$

$$D(t) = [t_1 \quad t_2 \quad \cdots \quad t_m] \tag{4-2}$$

Where *Y* is the actual output of the SLFN; *D* is the desired output of the SLFN; *t* is the iterations of the training algorithm. Thus, the errors and error energy between the actual output and the desired output can be given in equation (4-3) and (4-4) respectively.

$$e(t) = Y(t) - D(t) \tag{4-3}$$

$$E(t) = \frac{1}{2}\sum_J^m e(t)^2 \tag{4-4}$$

Otherwise, the gradient-based BP training algorithm reverse calculation, it is the key steps of the BP training algorithm, is illustrated as follow:

$$\Delta\beta(t) = -\eta \frac{\partial E(t)}{\partial \beta(t)} \tag{4-5}$$

$$\beta(t+1) = \Delta\beta(t) + \beta(t) \tag{4-6}$$

$$\Delta\beta(t) = \eta e(t)\, H(t) \tag{4-7}$$

$$\Delta w(t) = \eta\delta\, X(t) \tag{4-8}$$

$$\delta = f'\big(\, X(t)w(t)\big) \tag{4-9}$$

Where w are the weights between the hidden neuron and input neuron; β are the output weights connecting the hidden neuron and the output neurons; t is the training times; η is the learning rate;

From above mentioned calculation process, it shows that the traditional gradient-based BP training flow needs t times forward calculation and reverse calculation respectively. While the iterative times t is generally determined by model designment and demand of training accuracy. Furthermore, input weights and output weights are usually randomly determined, which will affect the training result.

4.2.2.Extreme learning machine

As above mentioned, the traditional gradient-based back-propagation training algorithms have some disadvantages such as trapping at local minima, the overtraining, and the high computing burdens, which causes longer training time of the SLFN during the learning process. Extreme learning machine algorithm was first proposed by Huang [77] for the SLFN. Compared with traditional gradient-based iterative learning algorithm is used extensively to SLFN, ELM algorithm actually incorporates the merits as follows [78-81]. ELM method has been applied in the field of image signal processing.

I. The ELM arbitrarily initializes the input weights and hidden biases and analytically calculates the output weights. The selection of the input weights and hidden biases will affect the prediction accuracy of the model. Furthermore, the output weights do not need to be iterated repeatedly in the training process. Consequently, the ELM

algorithm features an extremely faster learning speed than most popular learning algorithms, and thus dramatically reduce learning time.

II. Traditional gradient-based learning algorithms are iterative and may become trapped in local optima. Other problems include overtraining and overfitting. These issues may interfere with the training result, especially when modelling a nonlinear system. In contrast, the ELM algorithm is better at the generalization of training, thus overcoming these issues.

Consider an ELM based upon the network illustrated in Fig 4.2 with an activation function $g(.)$. It is assumed that the ELM is able to estimate Q training outputs with zero error. The algorithm can be represented by the following expression:

$$w = \begin{bmatrix} w_{11} & w_{12} & \cdots & w_{1n} \\ w_{21} & w_{22} & \cdots & w_{2n} \\ \vdots & \vdots & \ddots & \vdots \\ w_{L1} & w_{L2} & \cdots & w_{Ln} \end{bmatrix}_{L\times n} \tag{4-10}$$

$$\beta = \begin{bmatrix} \beta_{11} & \beta_{12} & \cdots & \beta_{1m} \\ \beta_{21} & \beta_{22} & \cdots & \beta_{2m} \\ \vdots & \vdots & \ddots & \vdots \\ \beta_{L1} & \beta_{L2} & \cdots & \beta_{Lm} \end{bmatrix}_{L\times m} \tag{4-11}$$

$$X = \begin{bmatrix} x_{11} & x_{12} & \cdots & x_{1Q} \\ x_{21} & x_{22} & \cdots & x_{2Q} \\ \vdots & \vdots & \ddots & \vdots \\ x_{n1} & x_{n2} & \cdots & x_{nQ} \end{bmatrix}_{n\times Q} \tag{4-12}$$

$$Y = \begin{bmatrix} y_{11} & y_{12} & \cdots & y_{1Q} \\ y_{21} & y_{22} & \cdots & y_{2Q} \\ \vdots & \vdots & \ddots & \vdots \\ y_{m1} & y_{m2} & \cdots & y_{mQ} \end{bmatrix}_{m\times Q} \tag{4-13}$$

$$M = \begin{bmatrix} \sum_{i=1}^{L} \beta_{i1} g(w_i x_1 + b_i) & \sum_{i=1}^{L} \beta_{i1} g(w_i x_2 + b_i) & \cdots & \sum_{i=1}^{L} \beta_{i1} g(w_i x_j + b_i) \\ \sum_{i=1}^{L} \beta_{i2} g(w_i x_1 + b_i) & \sum_{i=1}^{L} \beta_{i2} g(w_i x_2 + b_i) & \cdots & \sum_{i=1}^{L} \beta_{i2} g(w_i x_j + b_i) \\ \vdots & \vdots & \ddots & \vdots \\ \sum_{i=1}^{L} \beta_{im} g(w_i x_1 + b_i) & \sum_{i=1}^{L} \beta_{im} g(w_i x_2 + b_i) & \cdots & \sum_{i=1}^{L} \beta_{im} g(w_i x_j + b_i) \end{bmatrix}_{\mathrm{m \times Q}}$$

$$\begin{pmatrix} i = 1, 2, \cdots, \mathrm{L} \\ j = 1, 2, \cdots, \mathrm{Q} \end{pmatrix} \quad (4\text{-}14)$$

Where w_{ij} is the weight between the *i*th hidden neuron and *j*th input neuron; $\beta_i = [\beta_{i1} \quad \beta_{i2} \quad \cdots \quad \beta_{im}]$ is the vector of output weights connecting the *i*th hidden neuron and *m* output neurons; $x_j = [x_{1j} \quad x_{2j} \quad \cdots \quad x_{nj}]^T$ are the input signals; $b_i = [b_1 \quad b_2 \quad \cdots \quad b_L]^T$ is the bias of the *i*th hidden neuron.

Eq. (4-14) can be rewritten,

$$H\beta = M^T \quad (4\text{-}15)$$

In which M^T is the transpose of matrix *M* and *H* is the output matrix of the hidden layer. The matrix *H* can be represented as,

$$H = \begin{bmatrix} g(W_1 \cdot x_1 + b_1) & g(W_2 \cdot x_1 + b_2) & \cdots & g(W_L \cdot x_1 + b_L) \\ g(W_1 \cdot x_2 + b_1) & g(W_2 \cdot x_2 + b_2) & \cdots & g(W_L \cdot x_2 + b_L) \\ \vdots & \vdots & \ddots & \vdots \\ g(W_1 \cdot x_N + b_1) & g(W_2 \cdot x_N + b_2) & \cdots & g(W_L \cdot x_Q + b_L) \end{bmatrix}_{\mathrm{Q \times L}} \quad (4\text{-}16)$$

Where the *i*th column of *H* is the vector of outputs of the *i*th hidden neuron given inputs x_1, x_2, $\cdots$; x_n. Following initialization of the input weight matrix *w* ($L \times n$ dimensions) and the hidden layer bias vector *b* (length *L*), the matrix *H* ($n \times L$ dimensions) is uniquely determined. The matrix of output weights, β ($L \times m$ dimensions), can then be calculated by simply finding a matrix $\hat{\beta}$ in order to minimize the error function,

$$\min_{\beta} \|H\beta - M^T\| \quad (4\text{-}17)$$

It is worth noting that the input weights w and the hidden layer biases b are not changed during this procedure. The solution is expressed as the following:

$$\hat{\beta} = H^{+}M^{T} \tag{4-18}$$

Minimizing this function is equivalent to obtaining the unique smallest norm least-squares solution of linear system in eq. (9). The matrix H^{+} is the generalized Moore-Penrose inverse of the matrix H, which can be found using the singular value decomposition (SVD) method [82].

The Fig. 4.3 demonstrates the flowchart of ELM algorithm. There are four steps to implement the ELM algorithm, including (i) design of the SLFN structure, (ii) random choice of the input weights w and hidden biases b, (iii) acquisition of the initial hidden layer output matrix H and the output weights β, and finally (iv) improvement and updating of the hidden layer output matrix H and output weights β.

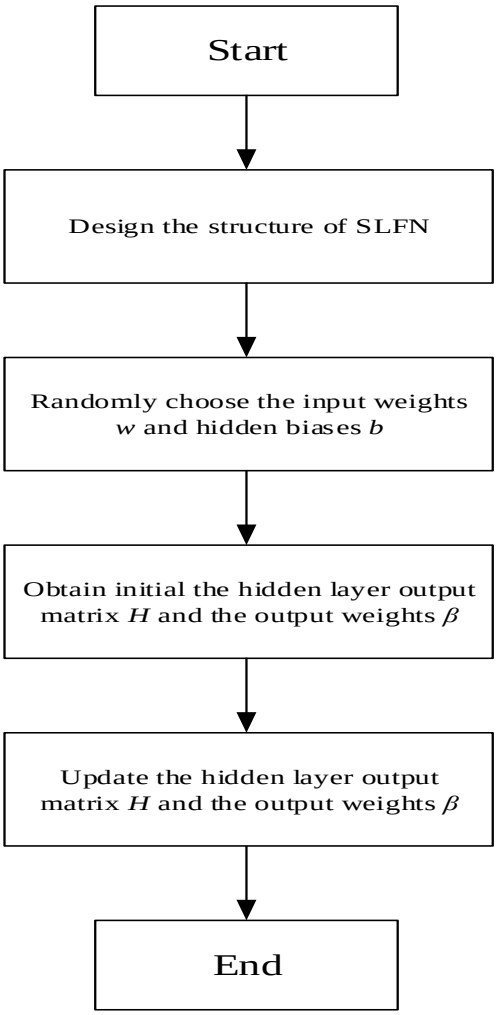

Figure 4.3 The flowchart of extreme learning machine (ELM)

4.2.3.Online sequential extreme learning machine

Compared with other traditional supervised batch learning algorithms in ANNS, ELM algorithm has the advantages of faster learning and better generalization capability. However, the ELM algorithm assumes that all the training data is available before the training begins. In real cases, this assumption cannot always be satisfied, as the data is available for training on a chunk-by-chunk or one-by-one basis. Thus, a novel sequential extreme learning machine is employed. The advantages of OS-ELM algorithm [83] are given as follows:

1) OS-ELM learning algorithm can receive the training data sequentially, i.e., arriving chunk-by-chunk or one-by-one.

2) At any time, only newly arriving data is used as valid training data and transferred to the learning algorithm.

Thus, the application of OS-ELM algorithm is very suitable for condition monitoring of wind turbines. Nowadays, the operation of wind turbines follows the power curve designed by the wind turbine manufacturer. As an example, the normal power curve of turbines from SCADA data is illustrated in Fig. 2.3 as the reference wind turbine; turbine power varies cubically with wind speed, and wind speed varies continuously on time-scales. When the wind speed is lower than the cut-in speed (4 m/s in this case), the turbine does not produce any power because the rotor torque is too low. When the wind speed is above the cut-out speed (25 m/s in this case), the turbine does not produce any power either because it is shut down to protect the turbine. If the wind speed is above the rated wind speed (15 m/s in this case) but below the cut-out speed, the turbine's output power is capped at the rated power.

The normal power curve can represent the operation performance of a fault-free wind turbine. The change of operation performance, i.e., the change of power curve of the wind turbine, may indicate the onset of a turbine fault. The power curve of a wind turbine shown in Fig.4.4 is an example of abnormal operations. In this case, the wind turbine reduces power output (show in the red circle) in order to prevent more serious faults from developing. Compared to shut-down of the wind turbine immediately when the fault is detected, the operation by reducing power output would reduce the mechanical loads experienced by the turbine, whilst still maintaining its operation.

In contrast, Fig. 4.4 shows the power curve of a faulty wind turbine. It can be seen that this turbine has, at some point, operated with reduced power output. After studying the fault log of the turbine, it has been concluded that this power reduction followed a fault with the gearbox.

As described above, the wind turbine can work in the different operation scenarios. When the operation performance is changed, new training data should be refreshed into the prediction model to fit the new operation scenarios. Thus, the advantages of OS-ELM algorithm is able to update training data to fit the new operation scenarios of the wind turbine. The full description of OS-ELM algorithm is given as follow:

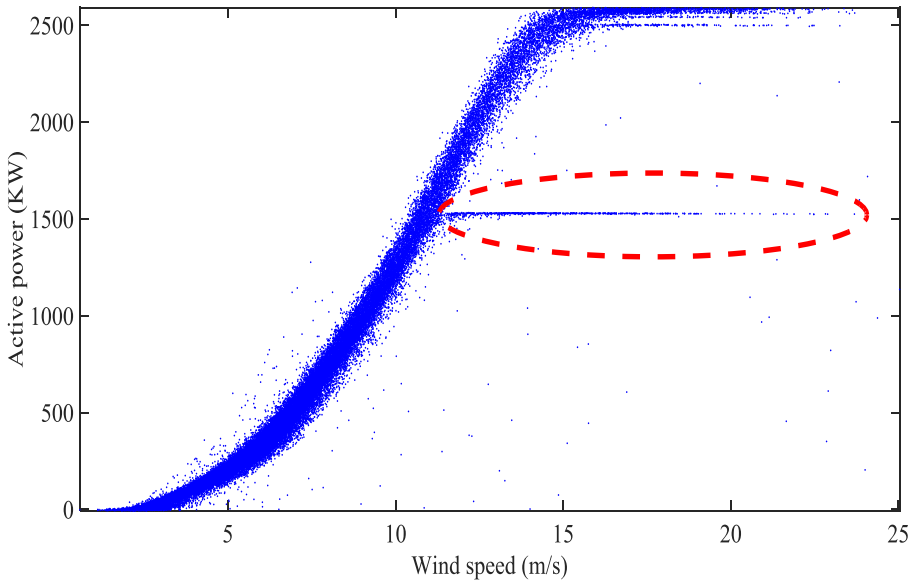

Figure 4.4 Power curve of the wind turbine with a gearbox fault

In order to make ELM online sequential, $\hat{\beta}$ can be transferred as follows:

$$H^{+}=(H^{T}H)^{-1}H^{T} \tag{4-19}$$

$$\hat{\beta} = (H^{T}H)^{-1}H^{T}M^{T} \tag{4-20}$$

Suppose the training data has two sets, one is the chunk of initial training data Q_0 and another is the chunk of update training data Q_1. Then, the equation (4-15) can be updated to equation (4-21), where the H_0 and M_0 are the output matrix of the

hidden layer of the ELM and the output matrix of ELM for the initial training data Q_0. The H_1 and M_1 are the output matrix of the hidden layer of the ELM and the output matrix of ELM for first chunk of training data Q_1 given in the next moment by minimising the error function as follows.

$$\left\| \begin{bmatrix} H_0 \\ H_1 \end{bmatrix} \beta - \begin{bmatrix} M_0^T \\ M_1^T \end{bmatrix} \right\| \tag{4-21}$$

The output weight matrix β that considers both initial block of training data Q_0 and block of training data given in the next moment Q_1 becomes

$$\beta^{(1)} = K_1^{-1} \begin{bmatrix} H_0 \\ H_1 \end{bmatrix}^T \begin{bmatrix} M_0^T \\ M_1^T \end{bmatrix} \tag{4-22}$$

Where

$$K_1 = K_0 + H_1^T H_1 \tag{4-23}$$

Therefore, the output weight matrix $\beta^{(1)}$ for the 1st chunk of training data Q_1 is depicted. Suppose $\beta^{(0)}$ is the output weight matrix for the chunk of initial training data Q_0, then

$$\beta^{(1)} = \beta^{(0)} + K_1^{-1} H_1^T \left(M_1^T - H_1 \beta^{(0)} \right) \tag{4-24}$$

As mentioned above, when the (K+1) th chunk of data arrives, the parameters are updated as follows:

$$K_{K+1} = K_K + H_{K+1}^T H_{K+1} \tag{4-25}$$

$$K_{K+1}^{-1} = K_K^{-1} - K_K^{-1} H_{K+1}^T (I + H_{K+1} K_K^{-1} H_{K+1}^T)^{-1} H_{K+1} K_K^{-1} \tag{4-26}$$

Using $P_{K+1} = K_{K+1}^{-1}$, the equation for $\beta^{(K+1)}$ can be updated

$$P_{K+1} = P_K - P_K H_{K+1}^T (I + H_{K+1} P_K H_{K+1}^T)^{-1} H_{K+1} P_K \tag{4-27}$$

The recursive formula for the (K+1)th output weight matrix $\beta^{(K+1)}$ becomes

$$\beta^{(K+1)} = \beta^{(K)} + P_{K+1} H_{K+1}^T \left(M_{K+1}^T - H_{K+1} \beta^{(K)} \right) \tag{4-28}$$

Hence, this sequential ELM algorithm has the ability of achieving the online training in real time, if the sampling speed for updated training data is quick enough. However, it is worth noting that, in this paper, the main purpose of using OS-ELM is to achieve training data being updated to ensure that the model is adapted to accommodate different operational behaviours of the wind turbines encountered during their operations. Real time online training capacity of the method is not considered in the paper. In this paper, one-year historical data is used as initial data to train initial weights. When the new scene data (the duration is one month in our study) is available, the new dataset is transmitted to OS-ELM model to update the weights.

4.3 Optimizing initial input weights and biases of ELM

As described in Section 4.2, arbitrary values are assigned to the weights of the inputs and the biases of the hidden neurons of the ELM model at the beginning of learning; clearly these parameters may not be the optimum values for the ANN. However, the training results of the ELM model largely depend on both the input-to-hidden weights and hidden-to-output weights, hence the ANN tends to have better generalization performance given small values for the weights. The selection of optimal initial input weights and biases would therefore be essential for an effective ELM model. Thus, a genetic algorithm (GA) [84] is adopted to optimize these weights and biases. GAs were originally proposed by Holland, and are a kind of parallel adaptive search algorithm based on the mechanics of natural selection and genetic systems, where individuals are usually represented by binary strings, as here. The algorithms have unique advantages, particularly in the fields of searching, optimization, and machine learning [85]. The purpose of using a genetic algorithm in this study is to obtain optimum values for the initial input weights and the initial hidden neuron biases so that the weights β can be calculated using equation (4-18). In general, a genetic algorithm has five steps, including initialization, fitness evaluation, selection, crossover and mutation operations.

The purpose of the selection operation is to obtain the probability of an individual being able to contribute to the next generation, This is based upon each individual's 'fitness', in this case, the optimum values for the initial input weights and biases. In order to achieve this, a roulette wheel selection technique is employed in the GA. There needs to be a balance in order to maintain the selection pressure and the diversity of the population. The crossover operation obtains new individuals from two 'parents'. Here a kind two-point crossover is used where two points are chosen on the parent chromosome strings. Two child chromosomes are obtained by swapping the elements between two points on the parent binary strings. Finally, the mutation operation introduces a random element to the individuals of the population. The rate of mutation increases exponentially as the number of generations decreases. For each mutation, a random number is generated. If the random number is smaller than the mutation rate, the value of the bit is flipped; otherwise, the value remains the same.

When the internal weights and biases are initialized, the ELM model calculates a predicted output. Clearly, it is desirable that the difference between the actual output and model prediction is the smaller the better. The fitness value can be found by calculating the sum of the absolute error that is difference between expected output and actual output of the ELM. Thus, the fitness value for each individual can be describe as follow:

$$F = k \sum_{i=1}^{m} |y_i - o_i| \tag{4-29}$$

$$f_i = \frac{k}{F_i} \tag{4-30}$$

Where m is the number of outputs; y_i is the ith predicted output of the ELM model; o_i is the ith actual output of ELM model; although k is an application dependent constant, k=1 is normally selected; f_i is the fitness value.

In selection stage, the operator is selected based on the result of the fitness evaluation. Consequently, the roulette selection approach is used in this section.

$$p_i = \frac{f_i}{\sum_{j=1}^{N} f_i} \tag{4-31}$$

Where N is the number of operators. It is worth noting that the great fitness operators are easy to be selected.

The crossover operation is a kind of two-point crossover. In the condition of some certain crossover probability, the two-point crossover operation is needed. It means that two points is going to be chosen on the parent chromosome strings. Two child chromosomes is obtained by swapping element of the two points between the parent binary strings.

$$\begin{cases} a_{kj} = a_{kj}(1-b) + a_{lj}b \\ a_{lj} = a_{lj}(1-b) + a_{kj}b \end{cases} \tag{4-32}$$

a_{kj} is kth chromosome on point j; a_{lj} is lth chromosome on point j; b is arbitrary constant between value zero and one.

The rate of mutation exponentially increases with the decrease of the number of generations. For each mutation, a random number is generated. If the random number is smaller than the mutation rate, the value on this bit is flipped; otherwise, the value remains the same as before.

$$a_{ij} = \begin{cases} a_{ij} + (a_{ij} - a_{max}) * f(g) & r > 0.5 \\ a_{ij} + (a_{min} - a_{ij}) * f(g) & r \leq 0.5 \end{cases} \tag{4-33}$$

$$f(g) = r_2 \left(1 - \frac{g}{G_{max}}\right)^2 \tag{4-34}$$

a_{max} is upper bound of the gene a_{ij}; a_{min} is lower bound of the gene a_{ij}; r is arbitrary constant between value zero and one; r_2 is random number; g is the number of iterations; G_{max} is the maximum number of the evolution.

The steps of the optimal extreme learning machine incorporating with genetic algorithm are described as follows:

Step 1: Define the structure of the SLFN, including the number of input layer neurons n and hidden layer neurons L respectively; arbitrary initial values are assigned to input weights w and hidden neuron biases b.

Step 2: The input weights and hidden neuron biases are forwarded to the genetic algorithm. Through the five steps of the GA described above, optimal initial values of the input weights and biases are determined. It is worth emphasizing that when the input weights and biases are initialized, the optimal output weights are uniquely determined, as described in the above section; thus output weights need not to be optimized by the GA.

Step 3: The ELM model is then updated using the initial values of w and b. The model is subsequently trained with the training data, with the hidden-to-output weights β being adjusted until the output data from the model matching the target output data.

Step 4: A set of input data are then used to test the model to observe how well the corresponding outputs are predicted. In this case, the output values are predicted by using optimized model. The actual outputs are then compared with the model prediction, and the residual signals between actual outputs and the model prediction are obtained.

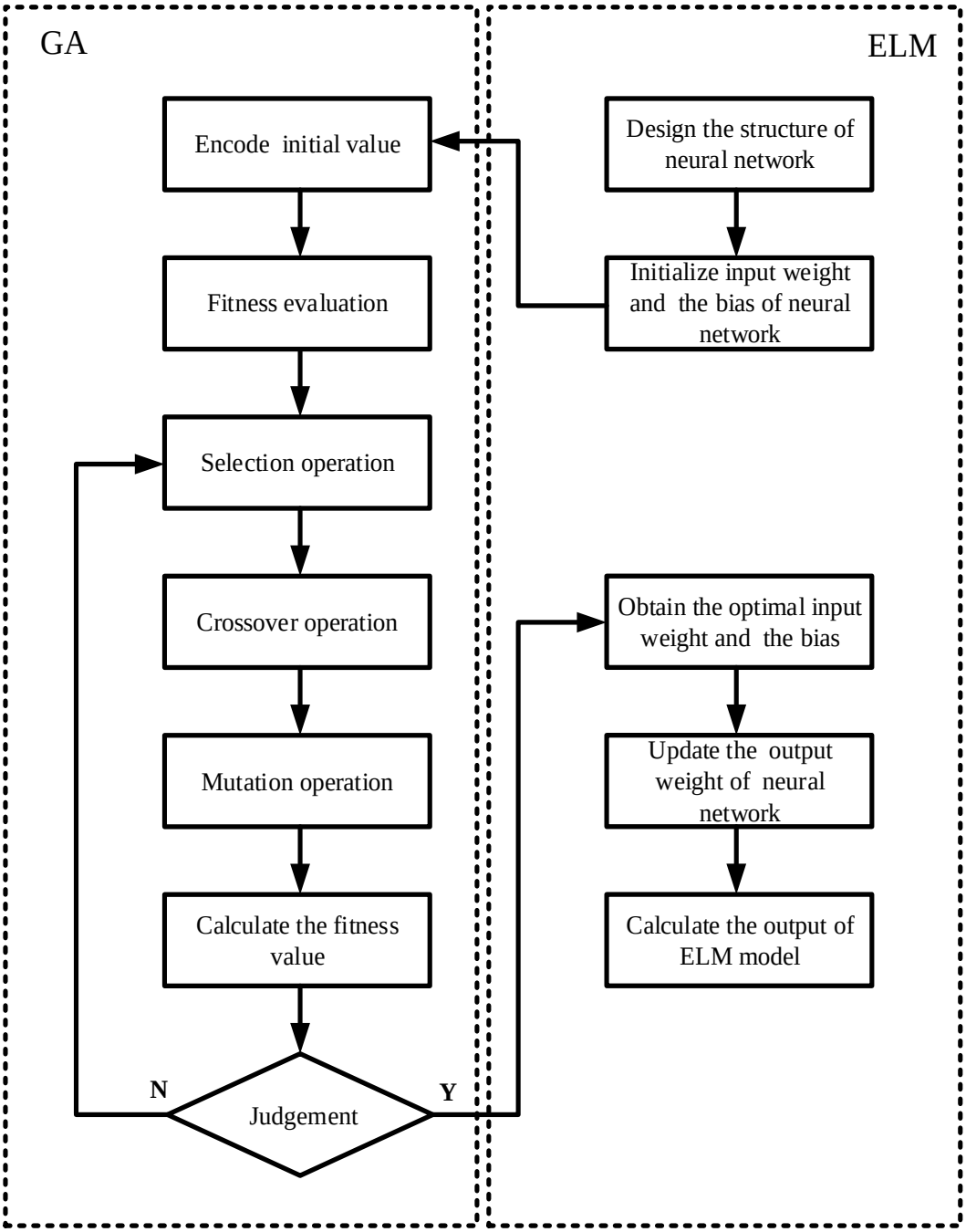

Figure 4.5 Schematic flow diagram of optimal extreme learning machine by using genetic algorithm

4.4 Fault identification

4.4.1.Multiple error calculation

As mentioned above, the faults happened in wind turbines can be investigated by comparing the difference between the actual signal detected in real time and the predicted signal from prediction model. Although a method relying on residual signals alone can only provide information regarding a specific component [7], it is not able to provide accurate overall details of the whole subsystem and relationship between different types of signals (i.e. temperature, pressure, voltage, current and vibration) in a wind turbine [86]. Although the residual signal can show impending component failure, it does not provide accurate details regarding the failure of components or subsystems in a wind turbine. One of the important aims of a CM system is to assist the operators to operate safely and reliably the wind turbines in order to avoid unnecessary operating outages. The outputs from such condition monitoring systems allow turbine operators to make decisions with regards to maintenance scheduling through improved understanding of the turbine's health condition. Reasonable maintenance strategies can therefore be implemented, which can significantly reduce the maintenance cost and enhance the availability and reliability of a wind turbine [7]. Previous research only focuses on a single variable analysis [8, 9], multivariable analysis taking account to interaction between different kinds of variables is more valuable yet. Wind turbines are the complicate system that generally have several subsystems, and each subsystem also has many components. Thus, it would be desirable to adopt a multiple error calculation method that considers relationship between multivariate in order to identify the fault degree of whole subsystem.

In previous research, Euclidean distance (ED) is a method that is widely used to estimate multidimensional variable error [35]. However, ED described in equation (4-35) is only suitable to measure the variables that has the same unit. Actually, there are more than 10 varieties of monitoring signals in real wind turbine condition monitoring system.

$$D = \sqrt{(A_1 - B_1)^2 + \cdots + (A_i - B_i)^2} \quad (4\text{-}35)$$

Where A_i and B_i are observation vectors and standard vectors respectively.

A minimum-redundancy maximum-relevance feature approach is adopted in this chapter to optimize the residual signal, taking into account interactions between signals measured from different components in the gearbox. The Mahalanobis distance (MD) is a measure of the distance between a point and a distribution without consideration of the units used for the measurement. Therefore, MD value is a positive value. This means that the MD measure has the capability to describe correlations among variables in a process or a system. Thus, the MD measure can provide a univariate distance value for multivariate data, which is ideal for estimating the deviation values of a complex system [87, 88]. Consequently, the MD measure is selected to help obtain the deviation from the group data, which can be used to identify the fault features of the gearbox. For the *i*th observation vectors $X_i = (x_{1i}, x_{2i}, ..., x_{ni})$ and $Y_i = (y_{1i}, y_{2i}, ..., y_{ni})$, the MD is given by matrix

$$MD = \sqrt{(X_i - Y_i)C^{-1}(X_i - Y_i)^T} \quad (4\text{-}36)$$

Where n is the number of parameters x_1, x_2, ·, x_n to be analyzed, for example, the temperatures and pressures of oil in the gearbox; the matrix C is the covariance matrix of X_i and Y_i , i.e., $C = cov(X_i,Y_i)$. In this chapter, the residual signals from the prediction model are used to from an observation vector X_i. Y_i is regarded as the reference vector with a reasonable deviation value. In ideal conditions, the values in the reference vector can be considered to be zero.

4.4.2.Fault identification

MD values can be accumulated over a period of time *t*, indicating the deviation of the calculated MD value from the expected value for different components in the gearbox. However, it is necessary for a confidence band for the accumulated MD values to be defined. In this chapter, the value of the confidence band is set to unity. If the accumulated MD values are below this level, the deviations are attributed to

signal interference, which are therefore ignored in the accumulation of MD values. Otherwise, the values are added to the accumulated MD value. Three relationships are considered in this study, including gearbox pump oil pressure with gearbox oil temperature, gearbox pump oil pressure with gearbox bearing 1 (main speed shaft bearing connected to the rotor) temperature, and gearbox pump oil pressure with gearbox bearing 2 (high speed shaft bearing connected to the electric generator) temperature, assessing the condition of each component in the gearbox. The MD values described in this section can therefore be extended to multiple processes.

However, the durability and failure modes of each component in a gearbox can be different; thus weights are allocated to represent the fault impact of each component on the performance of a gearbox. Here, a multiple MD model is defined as sum of all MD values above the confidence band observed during a defined period of time. This multiple MD model can be used as the basis of an early warning system, with an alarm raised if the threshold is exceeded.

The accumulated MD model with multiple components is described as follows:

$$RIV = \int_0^t (\alpha MD_1 + \beta MD_2 + \gamma MD_3)\, dt \quad \alpha + \beta + \gamma = 1 \tag{4-37}$$

where *RIV* is the risk indicator value of the gearbox as a whole*;* MD_1 is the MD value of the gearbox pump oil pressure to the gearbox oil temperature; MD_2 is the MD value of the gearbox pump oil pressure to the gearbox bearing 1 temperature; MD_3 is the MD value of the gearbox pump oil pressure to the gearbox bearing 2 temperature; α, β *and* γ are the weights of these MD values, respectively. The *RIV* takes the variability of each MD value into account when determining its distance from the multivariate center of the distribution, thus providing a more sensitive indicator. As can be seen from eq. (4-3), the *RIV* and its derivative change over time and a higher value of the derivative represents an indication of higher risk, indicating worsening fault of the gearbox.

4.5 Case study and analysis

The model predictions for the gearbox oil temperature, gearbox bearing 1 temperature and bearing 2 temperature using the optimized ELM model are illustrated in figures 4.6 to 4.8. Fig. 4.6 (a) shows the gearbox oil temperature obtained from the SCADA data for the faulty turbine. Fig. 4.6 (b) illustrates the predicted gearbox oil temperature obtained from the ELM model. Fig. 4.6 (c) illustrates the residual signal between the actual temperature and predicted temperature of the gearbox oil. It can be seen that the actual temperature deviates from the prediction at hour 2850 indicating the onset of the fault. Fig. 4.7 and Fig 4.8 show actual SCADA data, the signals predicted by the model, and the residual signals of the temperatures of gearbox bearing 1 and gearbox bearing 2, respectively. The temperatures of gearbox bearing 1 and bearing 2 deviate from the model predictions at hour 2850. At the same time, the actual gearbox oil temperature deviates from the predicted temperature. Clearly, it can be concluded that the models provide a reliable and effective indication of the onset of the gearbox fault.

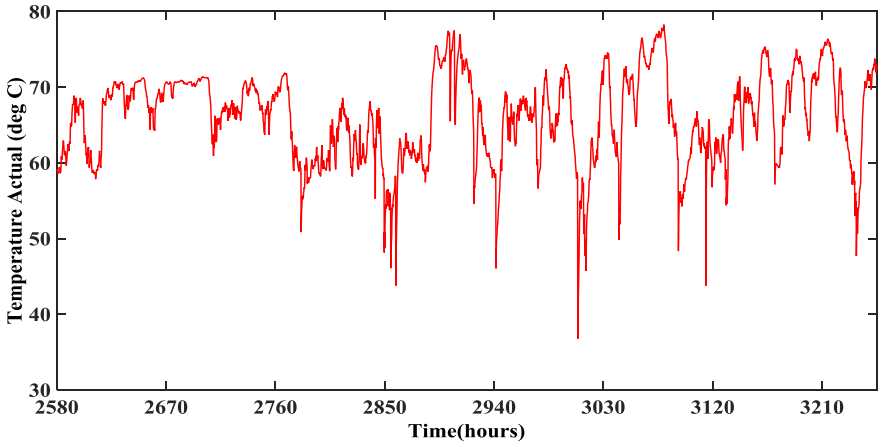

a. Actual temperature of the gearbox oil

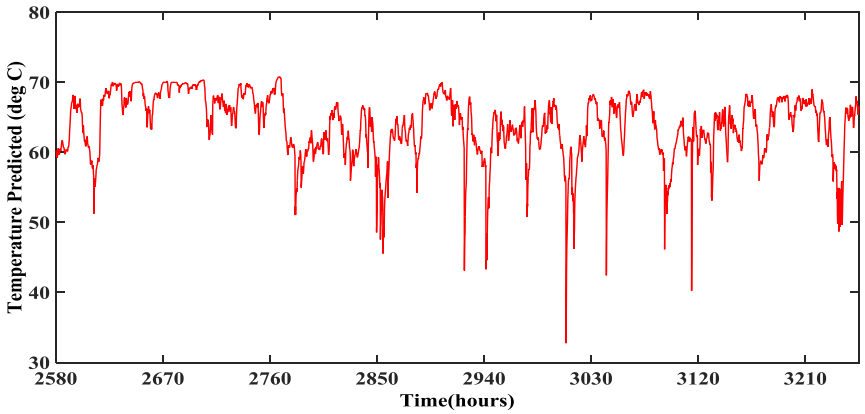

b. Predicted temperature of the gearbox oil

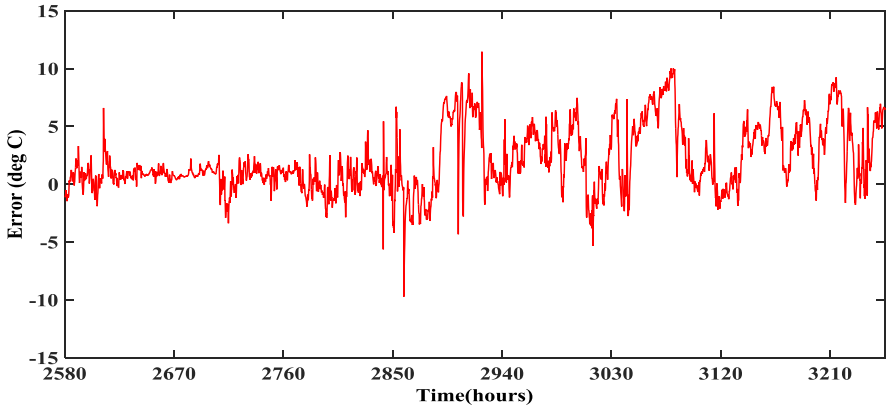

c. Residual signal of the gearbox oil

Figure 4.6 ELM model prediction compared to SCADA data for the gearbox oil temperature

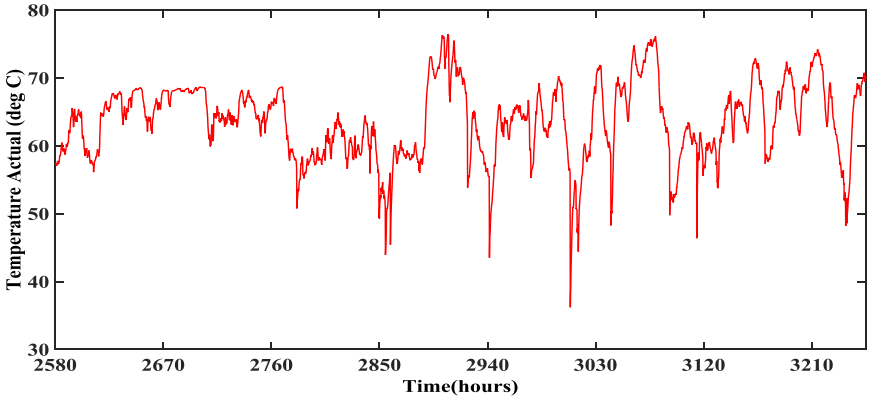

a. Actual temperature of the gearbox bearing 1

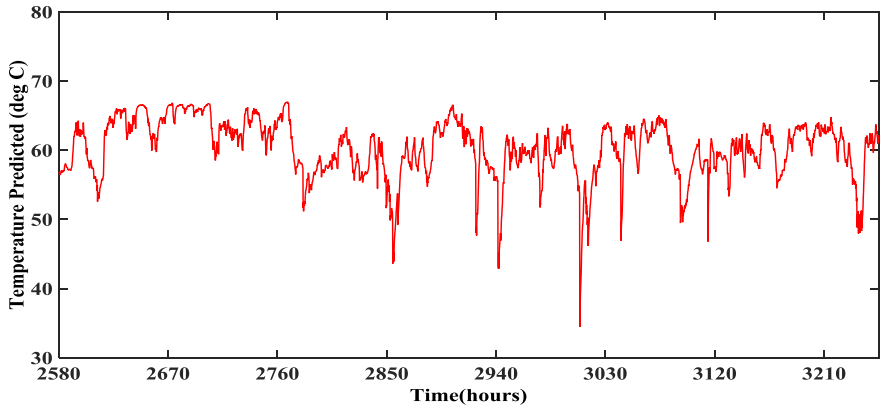

b. Predicted temperature of the gearbox bearing 1

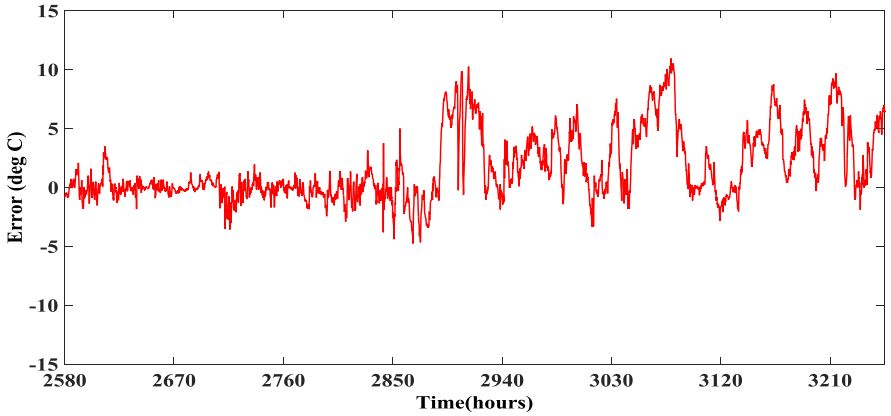

c. Residual signal of the gearbox bearing 1

Figure 4.7 ELM model prediction compared to SCADA data for the gearbox bearing 1

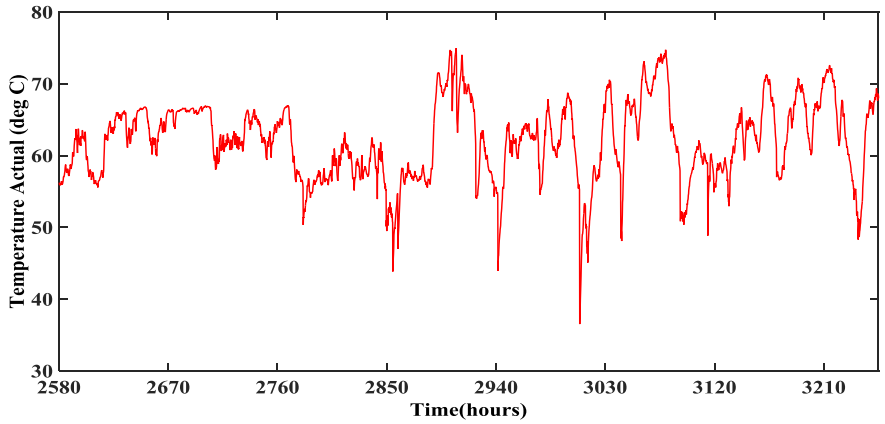

a. Actual temperature of gearbox bearing 2

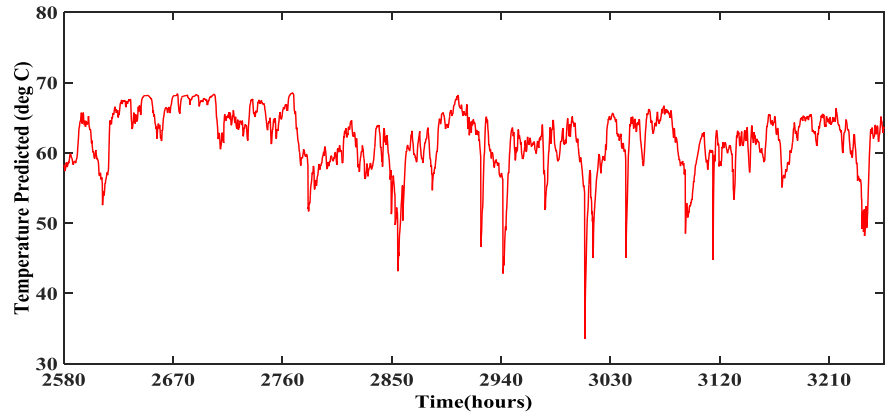

b. Predicted temperature of the gearbox bearing 2

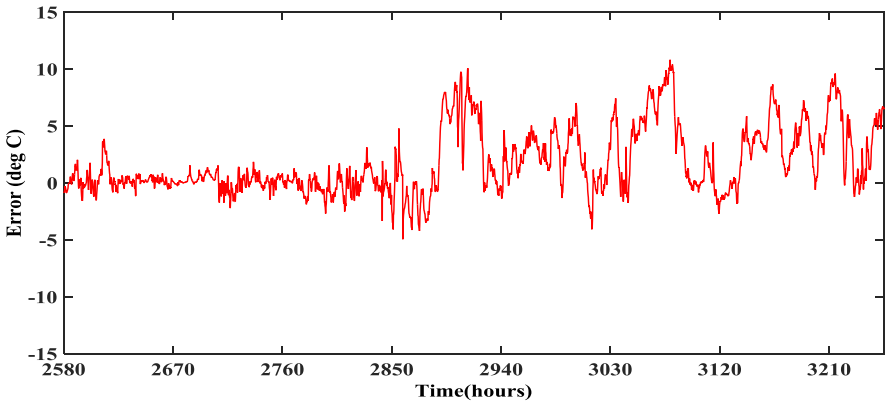

c. Residual signal of the gearbox bearing 2

Figure 4.8 ELM model prediction compared to SCADA data for the gearbox bearing 2

In addition to the temperature of the gearbox, the pressure of oil in the gearbox pump is another important signal that can be used to detect the faults of the gearbox in a wind turbine. Abnormal levels of oil pressure in the gearbox pump will affect heat dissipation from the gearbox, which is usually caused by faults in the gearbox oil pump, filter blocking of oil-conveying pipes or deterioration of the condition of the cooling oil. Thus, the modelled predictions for the oil pressure in the oil pump are also considered here. Note that the gearbox pump oil pressure changes with the power output of the turbine. Fig. 4.9 (a) shows the actual oil pressure in the oil pump, while Fig. 4.9 (b) illustrates the pressure of the oil as predicted by the ELM model. At 2850 hours, the residual signal in Fig. 4.9 (c) shows that the oil pressure begins

to deviate from the model prediction. In general, the cooling system is able to keep the gearbox at the normal operating temperature to ensure that no damage is caused, but when the temperature of the gearbox becomes abnormal, the residual signal of the oil pressure in Fig. 4.9 (c) fluctuates between positive and negative values. This indicates that the cooling system is attempting to restore the normal working conditions of the gearbox, but it is unable to do so effectively.

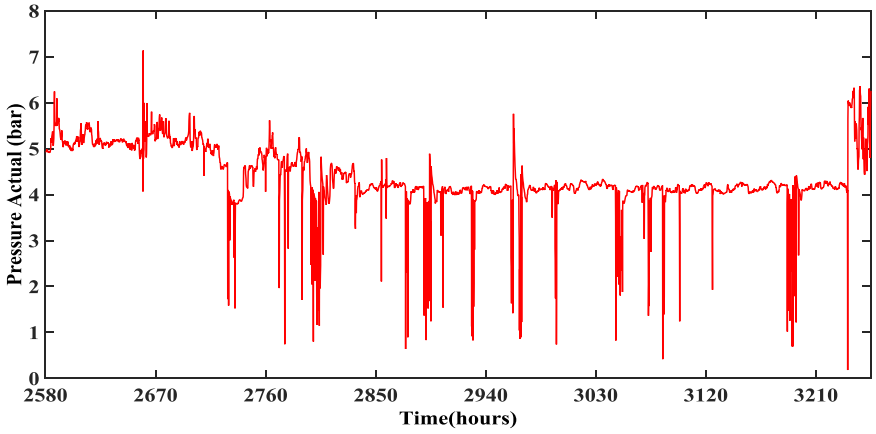

a. Actual pressure of the gearbox pump oil

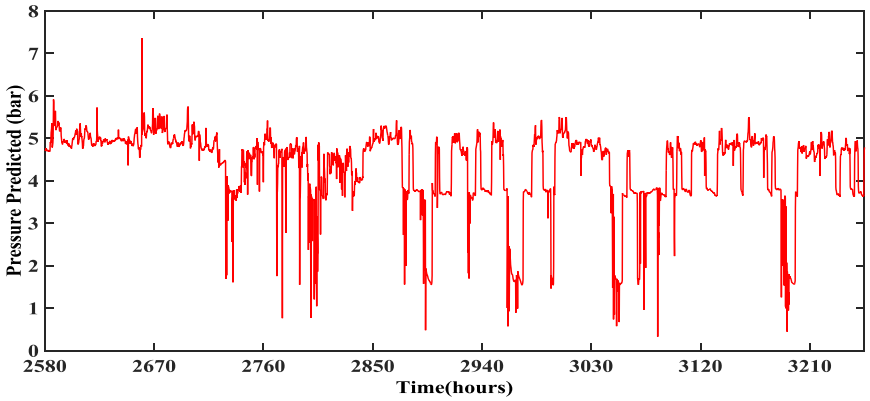

b. Predicted pressure of the gearbox pump oil

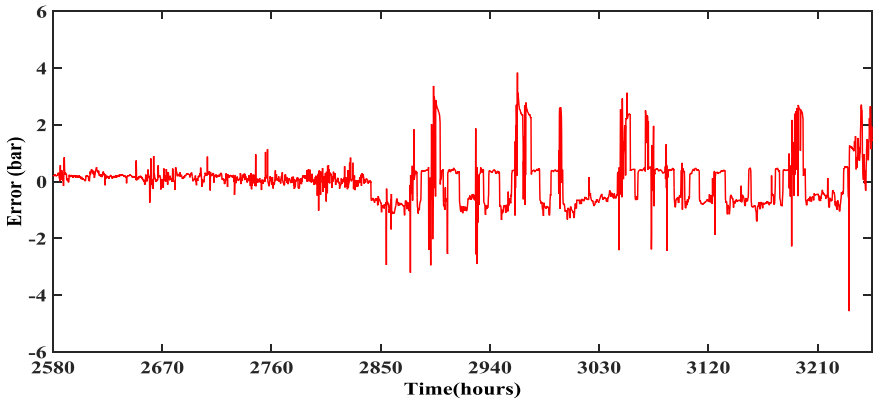

c. Residual signal of the gearbox pump oil

Figure 4.9 ELM model prediction compared to SCADA data for the gearbox pump oil

A desktop PC with a Xeon E3-1271 v3 3.6GHz CPU and 16GB RAM was used to implement the ELM. The time taken to train the ELM was compared with that taken to train a traditional BP back propagation neutral network using a threshold training algorithm, an algorithm commonly used to train ANNs. The ELM algorithm learns on an average of 0.16s compared to 22s using the BP method for the same training sets. Consequently, the ELM learning algorithm run around 138 times faster than the BP method. The root mean square error (RMSE) is also employed here as a measure of how well the models explain the actual output data. The RMSE values for the models with ELM and BP are 0.0915 and 0.0862 respectively. The full detail is given in table 4.1. This indicates that the ELM model also provides a good fit with considerably reduced learning time.

Type	Algorithm	Time(s)
Gearbox oil temperature	ELM	0.159s
Gearbox bearing1 temperature	ELM	0.154s
Gearbox bearing2 temperature	ELM	0.155s
Gearbox oil temperature	BP	23.018s
Gearbox bearing1 temperature	BP	22.786s
Gearbox bearing2 temperature	BP	23.542s

Table 4.1 Performance comparison between the ELM and the BP method

In order to assess further the condition of gearbox components, a MD measure of residual signals is used in this section to establish a relationship between the temperature change of gearbox components and oil pressure in the gearbox oil pump. The residual signal of the oil pressure is shown in Fig. 4.9 (c). The gearbox component residual temperatures, shown in Fig. 4.6 (c), 4.7 (c) and 4.8 (c), have been selected as the observation vectors. Hence, MD values of temperatures for the gearbox oil, gearbox bearing 1, and gearbox bearing 2 in relation to the working condition of the cooling system are obtained. Fig 4.10 shows the MD values calculated using equation (4-36) for these gearbox components. It can be seen that the MD values increase significantly at hour 2850, indicating the onset of the fault. Compared to individual residual signals from the predicted models shown in the fig 4.6 (c), 4.7 (c), 4.8 (c) and 4.9(c), these MD values shown in the fig 4.10, 4.11, and 4.12 can identify the fault more clearly by taking into account different monitoring signals from the system.

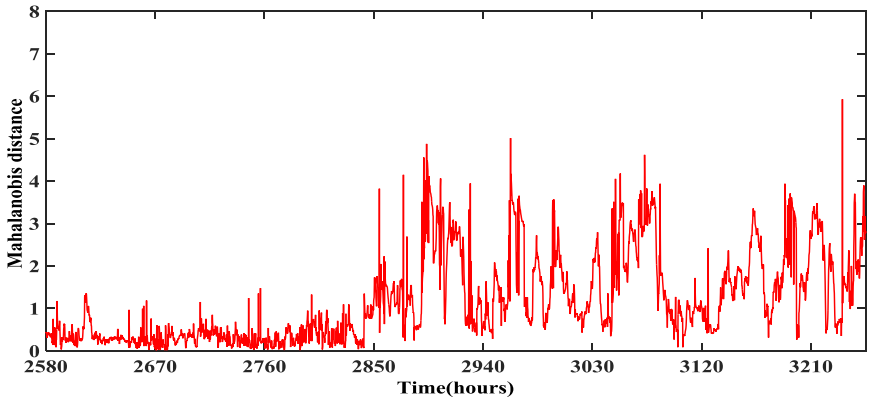

Figure 4.10 MD calculated for the gearbox Gearbox oil

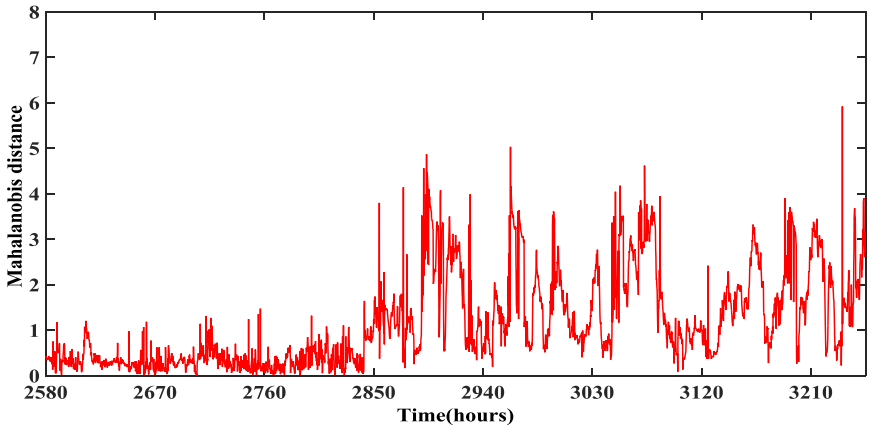

Figure 4.11 MD calculated for the gearbox Gearbox Bearing 1

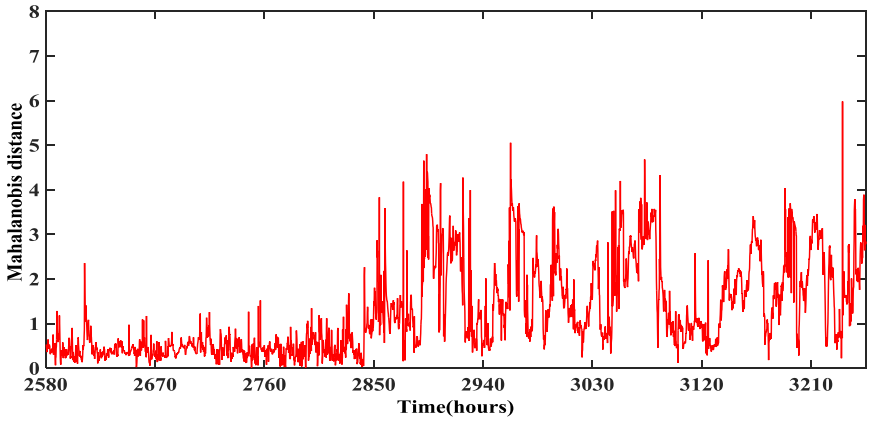

Figure 4.12 MD calculated for the gearbox Gearbox Bearing 2

The gearbox can be a major contributor to a turbine's downtime, with common failure modes being bearing faults and gear teeth faults. Surveys have shown that the root cause of gearbox failure is due to rapid changes of torque from stochastic wind profiles, which create an uneven load for the bearing and misalignment of gear teeth. Other causes of bearing and gear teeth failure are elevated operating temperature and excessive contamination of the cooling lubricant due to failure of the gearbox cooling system. Any fault from the gearbox can result in an abnormal input to the generator, reducing efficiency or, in extreme cases, damaging the generator. It would be desirable to use a more appropriate method in order to identify the health condition of the gearbox system as a whole. The accumulated MD values, referred to here as the 'risk indicator', describing relationships between the oil pressure and the bearing temperature changes are shown in Fig 4.10. As can be seen from the figure, the risk indicators of pump oil pressure to gearbox oil temperature, pump oil pressure to gearbox bearing 1 temperature and pump oil pressure to gearbox bearing 2 temperature demonstrate an almost same change in the derivative over time, representing an approximately equal share of risk of failure of each component. Therefore, for this case, the weightings of gearbox pump oil pressure to gearbox oil temperature, α, gearbox pump oil pressure to gearbox bearing 1 temperature, β, and gearbox pump oil pressure to gearbox bearing 2 temperature, γ, are each set to 1/3. The accumulated MD values from these components are then calculated using equation (4-37) to indicate the health condition of the gearbox as a whole. Fig 4.13 shows the observed risk indicator values of oil pressure to bearing 1 temperature for the gearboxes of one faulty and two fault-free wind turbines over a period of 1 month; the gearbox failure in the faulty wind turbine occurs at the middle of the month. When the fault begins to occur, the risk indicator value increases dramatically to 3500, after 16 days of the fault occurring. Conversely, the observed risk indicator values for the two fault-free wind turbines over the same month increases slowly, simply because of component aging.

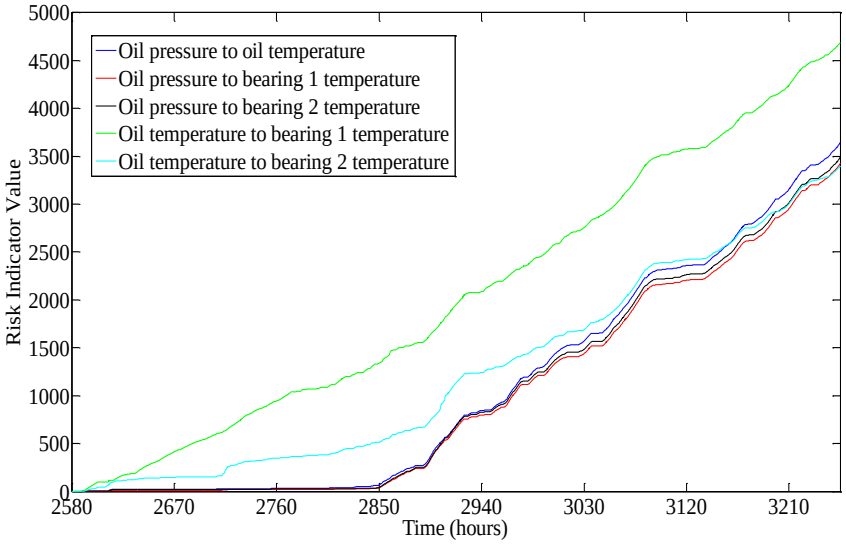

Figure 4.13 Observed risk indicators for the gearbox of a faulty turbine in relation to oil pressure and oil temperature in one faulty wind turbine, respectively

Fig. 4.14 also shows the observed risk indicators describing the relationship between the bearing temperature changes and the oil temperature. Even though these risk indicators have demonstrated a similar change over time, the MD values associated with the oil temperature increase monotonically with the time, and hence do not show the onset of the fault at hour 2850. It can therefore be concluded that the fault occurs in the cooling system, and the oil pressure should be selected to diagnose the operating condition of the cooling system in the gearbox. As is well known, active cooling systems are the main means for dissipating heat, which, for a wind turbine, include the oil lubrication system of the gearbox and the ventilation system of the generator. A typical gearbox lubrication system in a wind turbine consists of an oil pump unit, a heat exchanger, and an oil filter. Oil filters are used to remove impurities or metal particles within the lubrication oil in order to maintain oil quality and to prevent further wear of gearbox components. Pressure sensors are installed at both ends of the filters to monitor their status, while a temperature sensor is installed in the oil sump to measure lubrication oil temperature. The oil cooling system is started if the oil temperature is over a certain threshold, usually 60 ℃ [32].

In this chapter, the increase in gearbox temperature is due to an oil filter becoming blocked, as indicated in the alarm log and from an investigation of the SCADA data. The heat emission efficiency is reduced due to the oil filter blockage, leading to a rise in gearbox temperature.

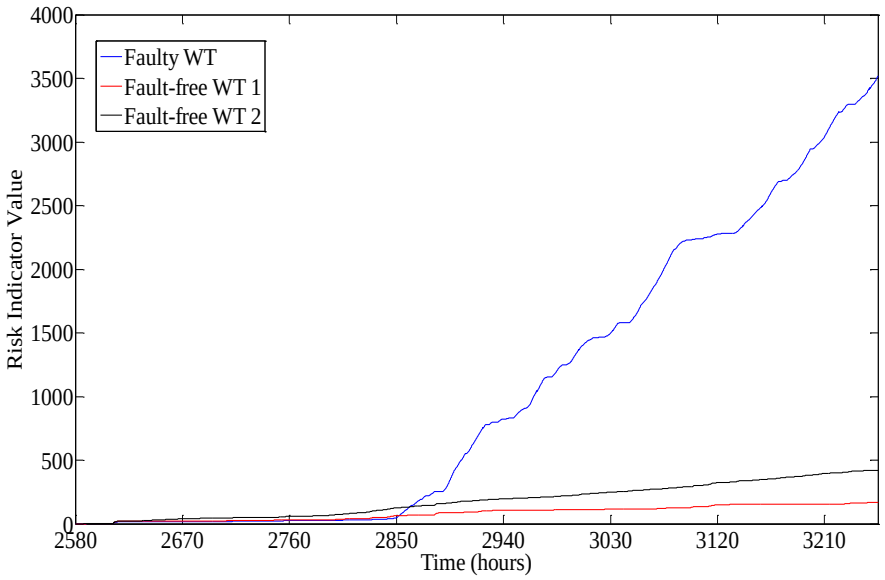

Figure 4.14 Observed risk indicator value of oil pressure to bearing 1 temperature for the gearbox of a faulty and two fault-free wind turbines over a period of 1 month

4.6 Summary and discussion

In this chapter, a data-based approach using an extreme learning machine (ELM) algorithm optimized with a genetic algorithm has been proposed for condition monitoring of the gearbox in wind turbines. The SCADA data, acquired from a working wind farm, have been used to demonstrate the effectiveness of the ELM method. These data include the temperature of the oil in the gearbox, the temperature of the gearbox bearings, and the pressure in the gearbox oil pump. Models derived from these data have been used to identify faults. It has been shown that the residual signals between the actual output and the predicted output are caused by a gearbox

fault, providing an early warning of impending failure. The results also demonstrate that the ELM learning algorithm can provide a good fit with a considerably reduced learning time compared to a BP algorithm.

Moreover, Mahalanobis distance (MD) values and accumulated MD values, obtained from multiple components, are employed to identify the health condition of the gearbox. These MD values can detect the fault more effectively by taking into account a range of different monitoring signals from the system. Observed risk indicator values, describing relationships between different components in the gearbox, have shown that the cooling system has a significant effect on the performance of the gearbox system.

Note that the data used in this chapter are mostly representative of the normal operation of wind turbines and do not contain a great deal of information regarding the occurrence of faults; consequently, this chapter employs static ELM models only. Future work will therefore consider dynamic models by taking into account the effect of more past inputs on the model output, and the different effect each component has on the health condition of the gearbox. In this chapter, the same value is used as the risk indicator for several different gearbox components. It is clearly worth evaluating different risk indicator values, taking into account the residual signal produced from the ELM model and the contributions to the downtime caused by failure of each component. A real-time early warning system, employing an online sequential ELM, will also be developed in order to predict faults in the operational wind turbines.

Chapter5. Optimizing wind farm power output control based on estimating health condition of wind turbines

This chapter presents an optimization of the wind farm power output control based on estimating health condition of wind turbines. The main procedure include fault degree estimation, health condition level estimation and optimal power dispatch control. Compared with previous method, the proposed method can adjust each wind turbine power output according to its health condition to optimize the total energy output of the wind farm and reduce the fatigue loading on faulty wind turbine. Bonferroni interval is selected to achieve fault degree estimation of wind turbines, analytic hierarchy process (AHP) is used to estimate health condition level. Finally, optimal power dispatch control strategy is formulated based on the result of health condition estimation. Models have been identified from supervisory control and data acquisition (SCADA) data acquired from an operational wind farm, which contains temperature data of gearbox bearing, and generator winding. Then, optimal power dispatch control strategy is validated by the simulation, it shows that the proposed method can significantly reduce the fatigue loading on faulty wind turbine.

5.1 Physical kinetic energy correction model

The gearbox is a key component of DFIG wind turbine, which is used because turbine rotor cannot reach synchronous speed that satisfies the operating condition of DFIG generator. The use of gearbox is to transmit kinetic energy from the turbine rotor to the DFIG electric generator through the drivetrain system. The CM of temperature signal is a proven method to diagnose the faults and predict the residual life of drivetrain system in the wind turbine. Traditionally, the same threshold is applied to temperature monitoring regardless of the operating power, which means the same weight is assigned for the temperature change in terms of its contribution to the damage of gearbox. However, the operating power could have a significant impact on the temperature changes; therefore, its effect on the temperature changes should be weighted differently [89-91]. A physical energy correction model is proposed in this chapter, which fully considers the effect of temperature change on drivetrain efficiency in wind turbine via analyzing kinetic energy transmission and heat losses.

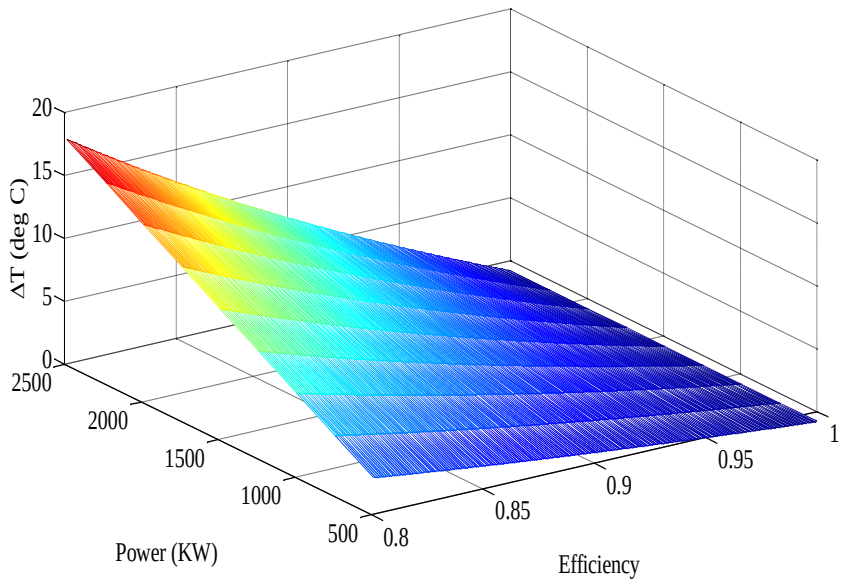

Figure 5.1. A 3D view of temperature rise, efficiency change and operating power of the drivetrain system

Supposing σ is the drivetrain system efficiency, *E* is the input kinetic energy from the rotor to the drivetrain system, *P* is the output kinetic energy from gearbox to generator, then E=1/σ×*P*.

Based on the first law of thermodynamics, we can have

$$Q = \left(\frac{1}{\sigma} - 1\right) P \tag{5-1}$$

Where *Q* represents the heat loss of gearbox, which leads to the temperature rise of drivetrain system. If ∅ is the compound heat transfer coefficient, the relationship between the heat loss of drivetrain system *Q* and the temperature rise of gearbox ΔT can be described by

$$Q = \emptyset \Delta T \tag{5-2}$$

Substituting equation (5-1) into equation (5-2) gives

$$\Delta T = \frac{1}{\emptyset}\left(\frac{1-\sigma}{\sigma}\right) P \tag{5-3}$$

In the ideal conditions, the compound heat-transfer coefficient ∅ is considered as constant. Fig. 5.1 illustrates an example of the relationship between temperature rise and efficiency change of drivetrain system at different operating power outputs for a 2.5MW wind turbine. As can be seen from the figure, the efficiency change rate varies at different power outputs. This implies that a fault occurring in drivetrain will lead to an increase in ΔT in response to a reduction of efficiency σ if the same power output is maintained. The higher the operating power output is, the smaller the efficiency varies for the same temperature change ΔT. This means although a same value of ΔT is caused by a fault in the drivetrain, its effects on the level of damage of drivetrain system differs if the power output is different.

Consequently, a temperature correction method is proposed. The temperature change ΔT is calculated from the ELM model in response to the power value gained from SCADA data, and then the corresponding efficiency σ is calculated by using equation (5-3). The temperature ΔT is then corrected to the value corresponding to when the turbine is operating at the full power at the given efficiency. The

temperature ΔT at different power point is then normalized to the value at the rated power output.

5.2 Fault degree estimation

The residual signals obtained from prediction model are now processed by the energy correction model. Although the traditional health condition systems can detect faults or estimate the health condition, they have been focused on monitoring specific components or areas, thus missing some relationship between components. The rising of gearbox bearing temperature can be caused by either the gearbox system aging or a potential fault or a failure. An example of temperature curve of gearbox bearing due to system aging in wind turbine is illustrated in Fig 5.2. The temperature curve in red shows the trend of temperature rise with active power output in a fault-free wind turbine during first 3 months of one year. Temperature rises with increasing active power output. The temperature curve after 6 months' operation is also shown in the figure with blue color; apparently, the temperature increases after the turbine operates for a period. An example of temperature rise due to a fault of the gearbox system is shown in Fig 5.3. In this case, the temperature actually deviates from the curve randomly, indicating the onset of a fault. After studying the alarm log of the SCADA data, it has been found that this is caused by a fault in the gearbox cooling system. The data in Fig 5.2 and Fig 5.3 are obtained from a commercial wind farm.

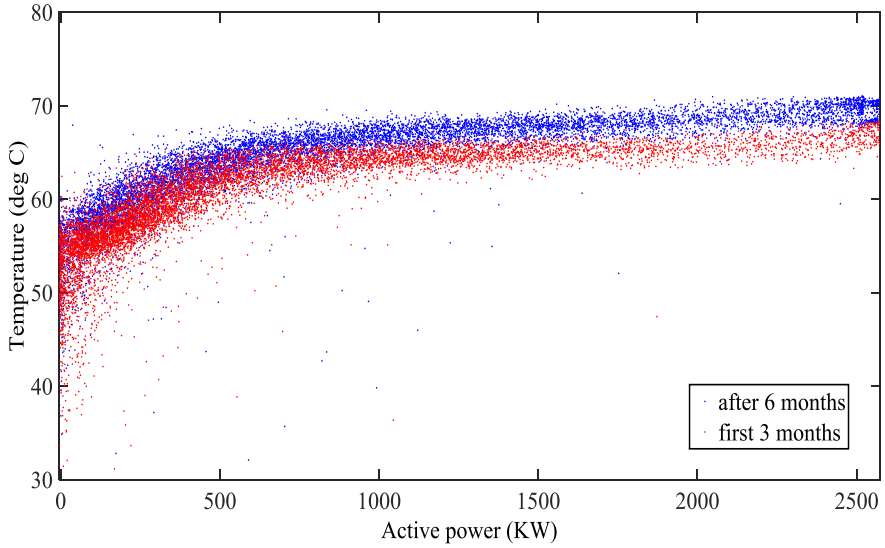

Figure 5.2 Gearbox bearing temperature rise trend in the first 3 months and after 6 months operation

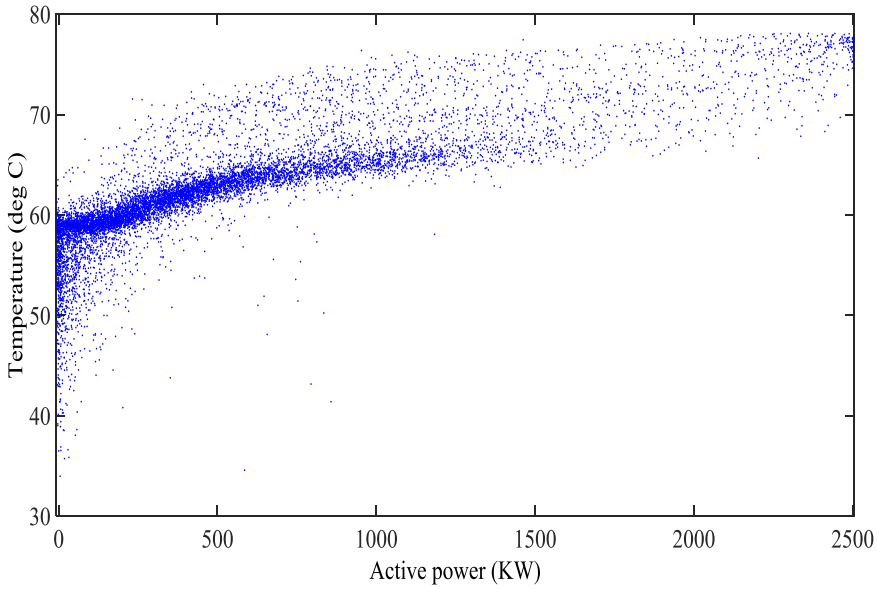

Figure 5.3 Gearbox bearing temperature rise trend resulting from a gearbox fault

In the model-based CM systems, faults can be diagnosed by comparing the difference between the actual signal detected and the predicted signal from the sequential extreme learning machine algorithm. Although a method relying on residual signals alone can detect faults effectively, it is not able to evaluate

accurately the significance about the failure of components. Furthermore, the drivetrain system in a wind turbine is generally composed of several components, which are, specifically, gears, bearings and the cooling system (usually oil cooling) [92, 93]. Clearly, it would be desirable to use a more appropriate method in order to identify the health condition of the drivetrain system by considering relationship between different components.

The estimation of whole system performance by using Hotelling's T-square, as described in equation (5-4), has been proven to be effective in [94], where the method was used to achieve multivariate failure mode analysis of electronics. The method can provide the global information of deviation level in wind turbines. Despite of the global effect it demonstrates, the method lacks the ability to provide details concerning the effect of individual components on the overall operational conditions. Thus, confidence intervals for the Hotelling's T-square method in equation (5-5) need to be computed and utilized in order to estimate deviation level for each variable.

$$T^2 = N(U-\mu)^T S^{-1}(U-\mu) \tag{5-4}$$

$$d_k(\alpha_k) = \overline{u_k} + \sqrt{\frac{p(N-1)}{(N-p)}F_{p,N-p}(\alpha_k)}\sqrt{\frac{s_{kk}}{N}} \tag{5-5}$$

where $U = (u_1, u_2, \cdots, u_k)^T$ indicates a set of variables, for example, including the temperatures of gearbox bearing u_1, gearbox oil u_2, and drivetrain main bearing u_3 in this study. The $\mu = (\overline{u_1}, \overline{u_2}, \cdots, \overline{u_k})^T$, where $\overline{u_k}$ represents the mean value of the measurement parameter u_k. The distribution $F_{p,N-p}$ is a *F* distribution used in statistics; *N* is the number of the samples for each measurement parameter; *S* is the covariance matrix of *U*; $s_{kk}$is diagonal value in the covariance matrix. In equation (5-5), α_k is a parameter that determines the sample deviation degree; when α_k is determined, the value of $F_{p,N-p}$ can be found from the *F* distribution table [95] and the confidence interval is thus determined. The parameter *p* is the number of variables.

It is worth noting that $\alpha_k$indicates probability of occurrence of the residual signal. If α_k<0.01, the monitoring data is considered to indicate a fault in the component，while，in this study case, α_k=0.25 is defined as a threshold value for debilitating condition. The values of α_k can be application dependent.

Bonferroni interval method can provide more accurate confidence intervals to estimate deviation level of each component than Hotelling's T-square confidence interval [95]. Thus, Bonferroni interval method, as described in equation (5-6), is applied in this study.

$$d_k(\alpha_k) = \overline{u_k} + t_{N-1}\left(\frac{\alpha_k}{2p}\right)\sqrt{\frac{s_{kk}}{N}} \quad (5\text{-}6)$$

The distribution t_{N-1} is a *t* distribution used in statistics and the value of t_{N-1} can be found from a *t* distribution table. In our study, the value of residual signal after processing with the energy correction model is considered as a fault if the value is more than $d_k(0.01)$. Meanwhile, $d_k(0.25)$ is defined as another threshold value for debilitating condition.

5.3 Health condition estimation

The gained results in section 5.3 can provide a quantitative value about fault degree of each component in wind turbines. As mentioned above, the wind turbine is a complex system, each component has different weight of index significance in whole system, and the servicing time and cost for every component are also different. Hence, health condition estimation for the wind turbine is able to be seem as a kind of multi-criterion decision making. In order to optimise power dispatch based on health condition of wind turbines, it is necessary to adopt a method to solve multi-criterion decision making problem of wind turbines.

Analytic hierarchy process (AHP) is a kind of technology for analyzing complex decisions, which is widely used in the field of business, government, shipbuilding, healthcare, industry and education [96, 97]. Because AHP is reliable and easy to

use. Compared with former prescribing a “correct” decision, the AHP can provide a comprehensive and reasonable model for decision making problems with different criteria. Thus, it is suitable for applying AHP in the health condition estimation.

The aims of using AHP method is to gain health condition level sorting considering multi-criterion factors [98]. In this chapter, three criterion elements are defined including fault degree, maintenance cost and maintenance time. Fault degree estimation is detailed in section 5.2, which can provide the information of damage degree for each component in wind turbines. Damage degree may affect power output performance of wind turbines and determine whether the wind turbine should be stopped. Consequently, it is the key information for health condition estimation of wind turbines (with mechanical and electrical faults). Maintenance time and cost are also selected as criterion elements, because maintenance time and cost determine the effective operating time and economic benefit of wind turbines.

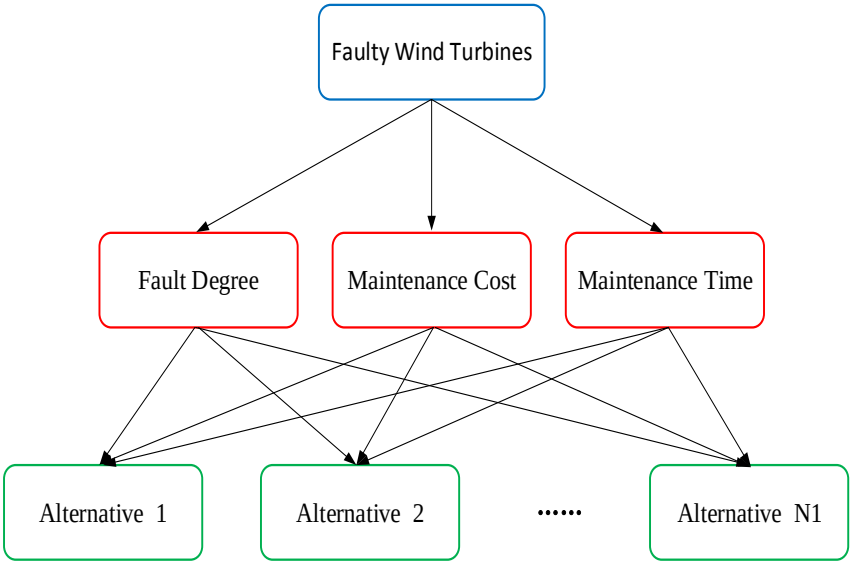

Figure 5.4 Hierarchical structure of wind turbines health condition estimation

Suppose there are *M* different alternatives and *c* different decision criterions. The steps of the health condition estimation for wind turbines incorporating the AHP are described as follows:

1) Define the evaluation criterions and establish a hierarchical structure. Fig 5.4 illustrates the hierarchical structure for wind turbines health condition estimation, which contains three predefined criterions including fault degree, maintenance cost and maintenance time.

2) Compose the pairwise criterion elements. Generally, there is an optional number from 1 to 9, which is usually assigned to a comparison matrix. In this chapter, we choose a typical three-point performance rating scale for significance of criterions. It defines that significance of criterions C_1, C_2, C_3 are high (C_1=9), medium (C_2=5) and low (C_3=1). Thus, the comparison matrix can be constituted in (5-7).

$$C_{3\times3} = \begin{bmatrix} c_{11} & c_{12} & c_{13} \\ c_{21} & c_{22} & c_{23} \\ c_{31} & c_{32} & c_{33} \end{bmatrix} = \begin{bmatrix} C_1/C_1 & C_1/C_2 & C_1/C_3 \\ C_2/C_1 & C_2/C_2 & C_2/C_3 \\ C_3/C_1 & C_3/C_2 & C_3/C_3 \end{bmatrix} \tag{5-7}$$

This method is also adopted to establish alternative pairwise comparison matrix A_N (*N*=1, 2 and 3) in (5-8). The vectors w_c and w_{AN} are eigenvectors corresponding to maximum eigenvalue of matrix $C_{3\times3}$ and A_N, which can be simplified the calculation by using equation (5-9),. (5-10) and (5-11).

$$A_N = \begin{bmatrix} a_{N11} & a_{N12} & \cdots & a_{N1M} \\ a_{N21} & a_{N22} & \cdots & a_{N2M} \\ \vdots & \vdots & \ddots & \vdots \\ a_{NM1} & a_{NM2} & \cdots & a_{NMM} \end{bmatrix}_{M\times M} \quad N=1, 2, 3 \tag{5-8}$$

Each column element of comparison matrix A_N is normalized as follow:

$$\overline{a_{ij}} = \frac{a_{ij}}{\sum_{i=1}^{M} a_{ij}} \tag{5-9}$$

Then, the line elements of the normalized comparison matrix A_N is added together by using equation (5-10).

$$\overline{w_i} = \sum_{j=1}^{M} \overline{a_{ij}} \tag{5-10}$$

The vector $\overline{w_i}$ is also needed to be normalized via the equation (5-11)

$$w_i = \frac{\overline{w_i}}{\sum_{j=1}^{M} \overline{w_j}} \tag{5-11}$$

Eigenvectors corresponding to maximum eigenvalue are given as follow:

$$w_c = [w_{c1} \quad w_{c2} \quad w_{c3}]$$
$$w_{A1} = [w_{A11} \quad w_{A12} \quad \cdots \quad w_{A1M}]$$
$$w_{A2} = [w_{A21} \quad w_{A22} \quad \cdots \quad w_{A2M}]$$
$$w_{A3} = [w_{A31} \quad w_{A32} \quad \cdots \quad w_{A3M}]$$

3) Calculate the health condition estimation relative criterion weights of the wind turbines via the equation (5-12)

$$\begin{bmatrix} w_1 \\ w_2 \\ \vdots \\ w_M \end{bmatrix} = \begin{bmatrix} w_{A11} & w_{A21} & w_{A31} \\ w_{A12} & w_{A22} & w_{A32} \\ \vdots & \vdots & \vdots \\ w_{A1M} & w_{A2M} & w_{A3M} \end{bmatrix}_{M\times 3} \times \begin{bmatrix} w_{c1} \\ w_{c2} \\ w_{c3} \end{bmatrix}_{3\times 1} \tag{5-12}$$

5.4 Optimized power dispatch control

Wind farm control scheme is designed to make wind farm steady operation by using a separate energy storage system or through de-rated operation of wind turbines [12]. But utilization of a separate energy storage system is impossible to apply in a large wind farm, due to high maintenance cost and capital investment of the separate

energy storage system. Thus, a de-rated operation wind farm control system is a practical solution. Generally, power demand of network operator is less than the maximum available power [34]. Fig 5.5 illustrates the schematic diagram of wind farm control system based on health condition estimation. It contains three parts, network operator (NP), and condition monitoring (CM) system and wind farm control (WFC) system. NP monitors the condition of the power grid to determine the demand of power output P^* to the wind farm; CM system determines information regarding the operating condition C_N of each wind turbine in the wind farm; WFC allocates the power output to each turbine ($P1$, $P2$ … PN) by considering both P^* and C_N. For each wind turbine, it may work under its own operation mode such as maximum power point tracing (MPPT) mode, de-rating mode, percentage mode and delta mode [66].

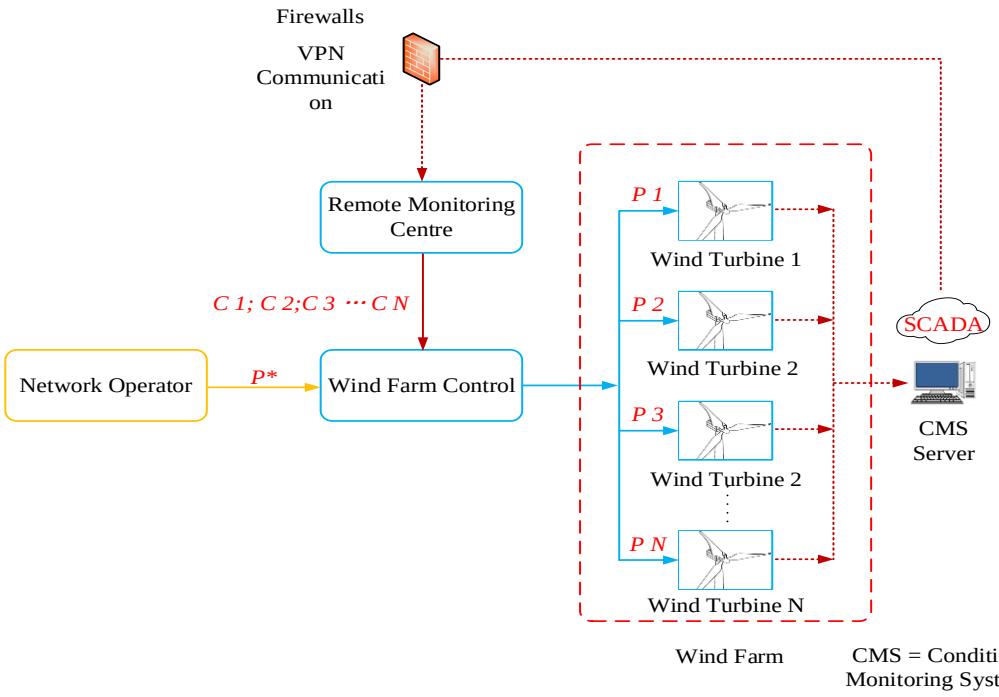

Figure.5.5 The schematic diagram of wind farm control system based on wind turbine health condition estimation

The proposed optimal power control for wind farm based on the heath condition estimation of individual turbine is to reduce mechanical loads acting on the faulty wind turbines while satisfying power output P^* demanded by the NP. Thus, the procedures of power dispatch strategy is defined as follows: for the healthy wind turbines, they are set to operate in MPPT mode, which produce maximum power output under variable wind speeds; for the faulty wind turbines, they work in power reducing mode. Therefore, the total power output of the wind farm P_t is defined as below, which is used to optimize the power distribution based on health condition of the wind turbine.

$$P_t = \sum_1^{N1} P_h + \sum_1^{N2} C_f P_f \tag{5-13}$$

Where N_1 and N_2 represent the number of the healthy and faulty wind turbines, respectively; P_h is the power output of the healthy wind turbine operating in MPPT mode whereas P_f is the power output of the faulty wind turbine working in power reducing mode, including de-rated mode, delta mode and percentage mode; C_f is the distribution coefficient based on result of health condition estimation relative criterion weights of the wind turbines. When the faulty wind turbines working in power reducing mode, the power dispatch control strategy is to make the power output of the faulty wind turbines satisfy the power balance between the network demand and power production of the wind farm. In this chapter, power is assigned to the faulty wind turbines based on a proportional distribution considering the outcome of health condition level estimation that we discuss above.

5.5 Case study and analysis

5.5.1 Case study about fault degree estimation

In this chapter, gearbox temperature at different locations are selected to monitor the condition of gearbox. The data contains temperature readings for gearbox bearing 1, i.e. the main speed shaft bearing connected to the rotor, the gearbox oil, and the main

bearing temperature, as shown in Fig 3.1. Two wind turbines are selected to verify the effectiveness of proposed method, one being a fault-free turbine with system aging only, while the other being a faulty turbine. In order to achieve an appropriate model identification, wind speed, ambient temperature and power output are selected as the inputs while the targeted temperature in the gearbox is considered as the output. This multiple-input and single-output (MISO) approach allows a more sensitive detection.

This section now presents and compares the residual temperature signal produced by using OS-ELM model without and with energy correction method being applied. Fig. 5.6 (a) and (b) illustrates residual signal of the gearbox bearing temperature due to the system aging problem by comparing the data obtained from the SCADA system and model prediction. It can be seen that both methods demonstrate the temperature rises with time, which is caused by the system aging. However, the corrected gearbox bearing temperature exhibits a more obvious deviation trend than the one produced from the normal method. The maximum difference between corrected signal and normal signal due to the system aging for the fault-free turbine can reach up to 4.7 ℃ because temperatures are converted to the values at the rated power output in the correction model. It means that the revised signal has more sensitivity than tradidtional method, which is benifical to detect the faults happened in the wind turbine. Fig. 5.7 (a) and (b) demonstrates residual signal of gearbox bearing temperature in the condition of the bearing fault. It can be seen that the gearbox bearing temperature deviates in April, indicating the onset of the fault, and it reaches the worst condition at the beginning of September. It also appears that the corrected bearing temperature shows a much clearer characteristics when the fault begins. The maximum difference between corrected signal and normal signal for the faulty turbine can reach up to 7.2 ℃. Consequently, the revised method has a better sensitivity than the normal method, thus facilitating a more accurate fault detection.

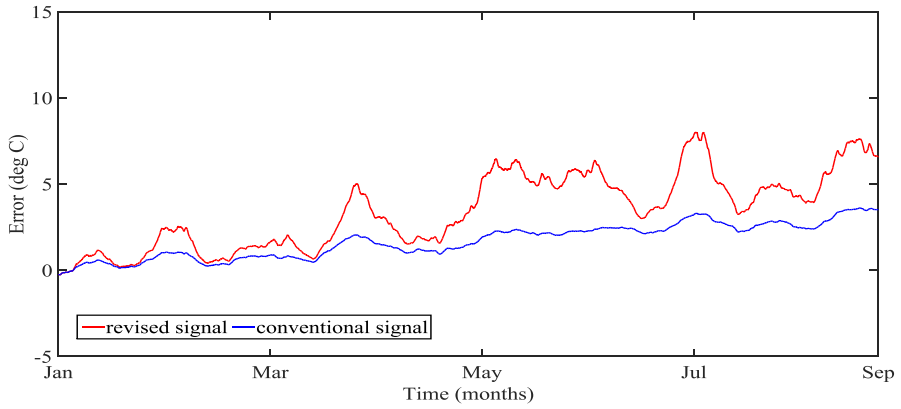

a.

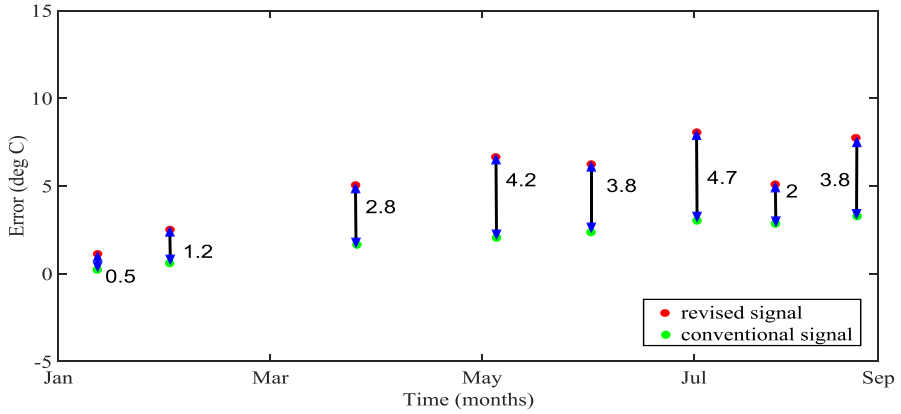

b.

Figure.5.6 Comparison of the difference between corrected signal and normal signal due to the system aging for the fault-free turbine

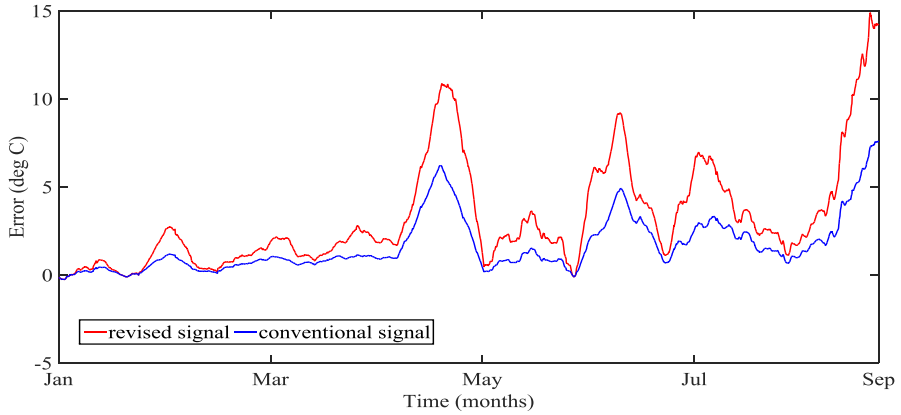

a.

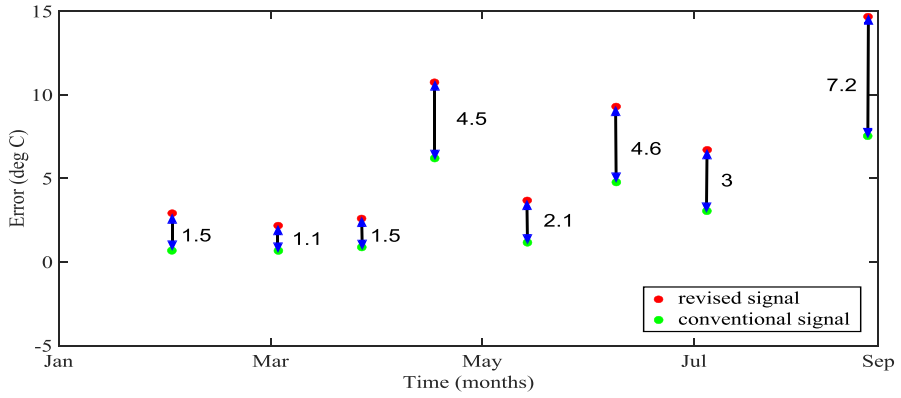

b.

Figure.5.7 Temperature changes from the corrected signal and normal signal for the faulty turbine

In order to assess further the condition of drivetrain components, the Bonferroni intervals and confidence intervals for Hotelling's T-square are compared, which are used to access each variable deviation in a multivariable system. Two sets of α values are selected for both Bonferroni intervals and confidence intervals for Hotelling's T-square. One is α=0.01, the other one is α=0.25, as described above. The residual signal is considered as an anomaly if it is over $d_k(0.01)$ [8]. Fig. 5.8 shows the residual signal between the actual temperature and predicted temperature of the gearbox bearing for the faulty turbine during 9 months. It can be seen that the gearbox bearing temperature deviate from the prediction at April, indicating the onset of the fault. Although the residual signal value starts fluctuating between April and September, it is still within the tolerance zone. At the beginning of September, the fault leads to a dramatic increase in the residual value. The values of $d_k(0.01)$ and $d_k(0.25)$ for Bonferroni intervals by using equation (5-6) are 9.84 ℃ and 6.4 ℃ respectively. Meanwhile, the values of $d_k(0.01)$ and $d_k(0.25)$ for Hotelling's T-square confidence intervals are 10.5 ℃ and 8 ℃ respectively. Therefore, Bonferroni intervals is smaller than Hotelling's T-square confidence intervals.

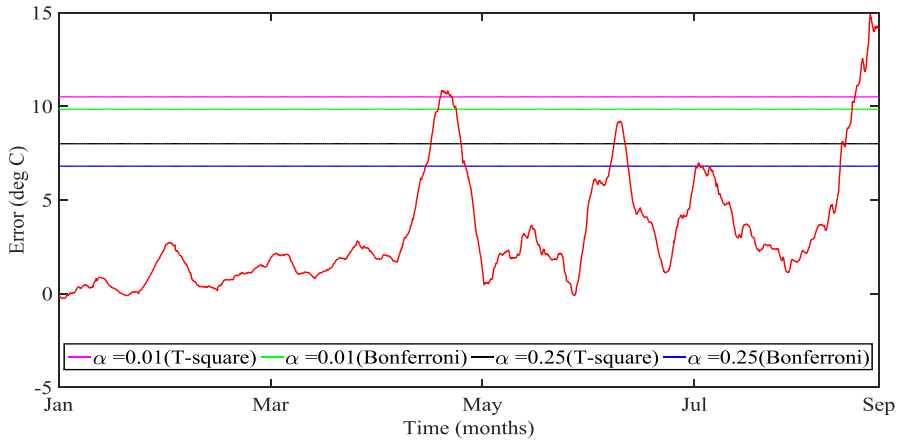

Figure.5.8 Comparison of Bonferroni intervals and confidence intervals for Hotelling's T-square for gearbox bearing in faulty wind turbine

The model predictions for gearbox oil and drivetrain main bearing using the OS-ELM model and physical kinetic energy correction model are given as follows. Fig 5.9 (a) shows the residual signal between the actual temperature and predicted temperature of the gearbox oil for the fault turbine during 9 months. The values of $d_k(0.01)$ and $d_k(0.25)$ for Bonferroni intervals are 9.78 ℃ and 6.6 ℃ respectively. It seems that the faulty characteristic of the gearbox oil is the same to the gearbox bearing. Fig 5.9 (b) illustrates the residual signal between the actual temperature and predicted temperature of the drivetrain main bearing. The values of $d_k(0.01)$ and $d_k(0.25)$ for Bonferroni intervals are 13.1 °C and 10.2 ℃ respectively. The drivetrain main bearing deviates from the prediction at April, and at the end of May with the temperature deviation exceeding of $d_k(0.01)$. The drivetrain main bearing temperature also begins to recover to normal temperature at the end of July. All the details about wind turbine faults mentioned above can be found in the alarm log obtained from operational wind farm.

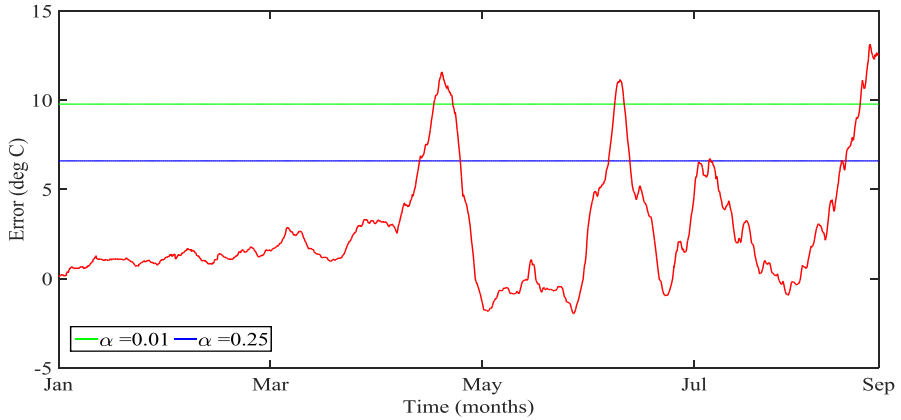

a. Gearbox oil temperature rise trend during 9 months

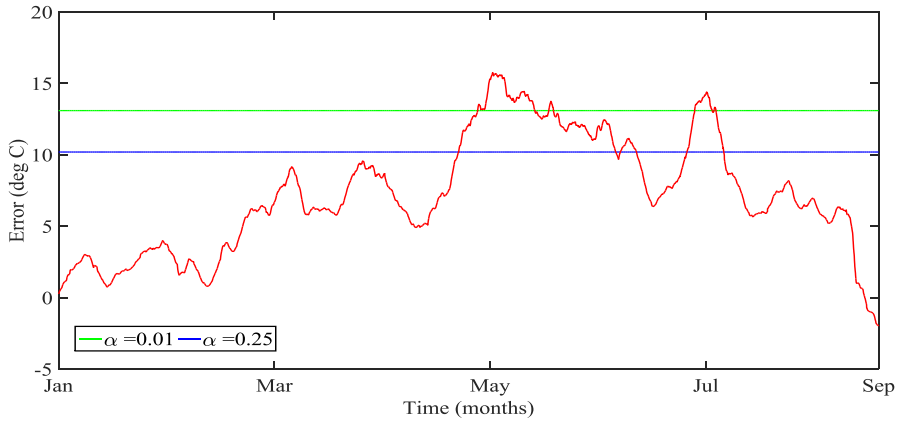

b.Drivetrain main bearing temperature rise trend during 9 months

Figure.5.9 Drivetrain temperature rise trend in the condition of the system faults during 9 months

In addition to condition monitoring of the faulty wind turbine, another example is to assess the above temperatures for a fault-free wind turbine with aging problem only. Fig 5.10 (a) shows the residual signal between the actual temperature and predicted temperature of the gearbox bearing for the aging turbine during 9 months. Fig 5.10 (b) illustrates the residual signal of gearbox oil temperature for the same wind turbine. It can be seen that although the gearbox bearing and oil temperature residual signals have a rising trend, they are still below the $d_k(0.25)$, indicating the gearbox is in healthy operational condition. The variation of power output has less effect on oil temperature than bearing temperature, because cooling oil has a higher

specific heat capacity than metal. Fig 5.10 (c) illustrates the residual signal between the actual temperature and predicted temperature of the drivetrain main bearing, showing it is also within a safe operational range.

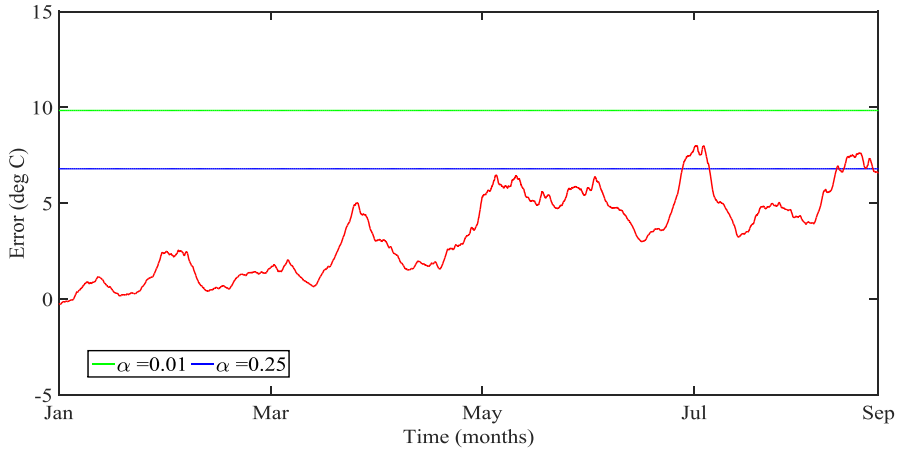

a.Gearbox bearing temperature rise trend

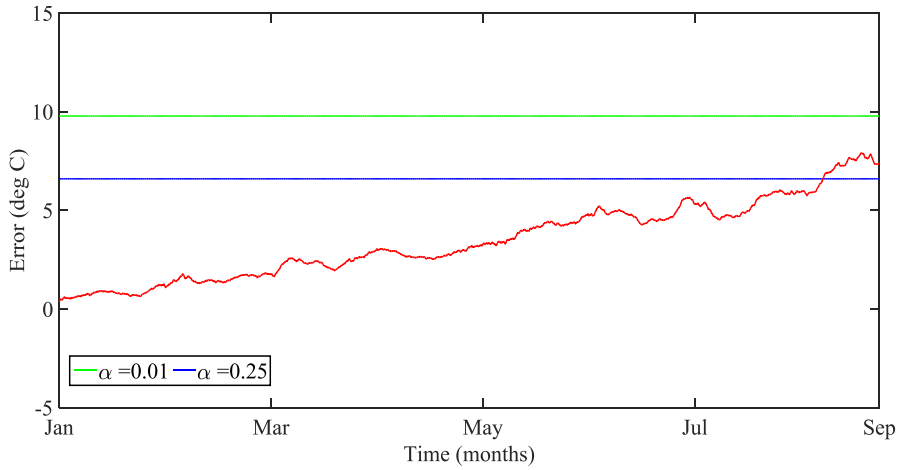

b.Gearbox oil temperature rise trend

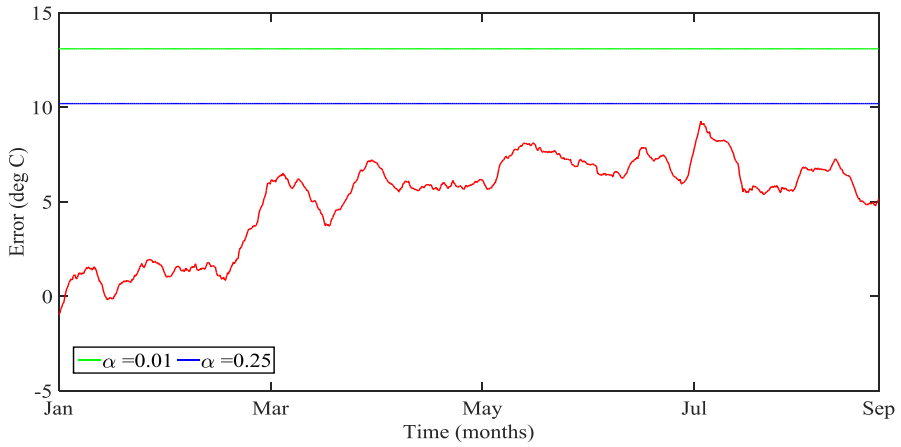

c. Drivetrain main bearing temperature rise trend

Figure.5.10 Drivetrain temperature rise trend in the condition of the system aging during 9 months

5.5.2 Case study about health condition estimation

In order to validate the proposed optimizing wind farm power output control based on estimating health condition of wind turbines, gearbox bearing (main-speed shaft bearing connected to the rotor, as shown in Fig 3.1) and generator winding temperature are selected from SCADA to monitor the condition of gearbox and generator. These signals can be used for feature extraction to show the condition of the gearbox and generator. The data sampling rate of SCADA data is 10 minutes.

The model predictions for gearbox bearing and generator winding temperatures using the ELM model and Bonferroni interval method are given as follows. Fig 5.11 shows the residual signal between the actual temperature and predicted temperature of the gearbox bearing for the faulty turbine during a time duration of 300 hours. The values of $d_k(0.01)$ and $d_k(0.25)$ for Bonferroni intervals are 9.84 and 6.4 respectively. It can be seen that the gearbox bearing temperature deviate from the prediction at 120 hours indicating the onset of the fault. Although the residual signal value between 120 and 280 hours becomes fluctuant but it still lies in zone of

tolerance. After 280 hours, the fault becomes serious, leading to a dramatic increase in the residual value.

Fig 5.12 illustrates the residual signal between the actual temperature and predicted temperature of generator winding. The values of $d_k(0.01)$ and $d_k(0.25)$ for Bonferroni intervals are 41.3 and 25.8 respectively. The temperature of generator winding has some fluctuation around 150 hours, however it still in the safe area, and at the end of 270 hours the temperature deviation exceeds value of $d_k(0.25)$, indicating a minor fault occurring in the generator. The details about wind turbine faults mentioned above can be found in alarm log obtained from the operational wind farm.

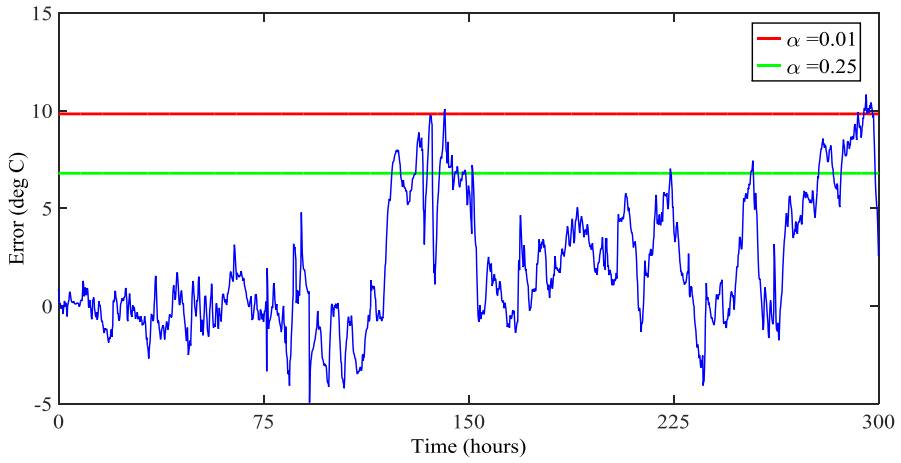

Figure 5.11 Residual signal of the gearbox bearing temperature between SCADA data and model prediction

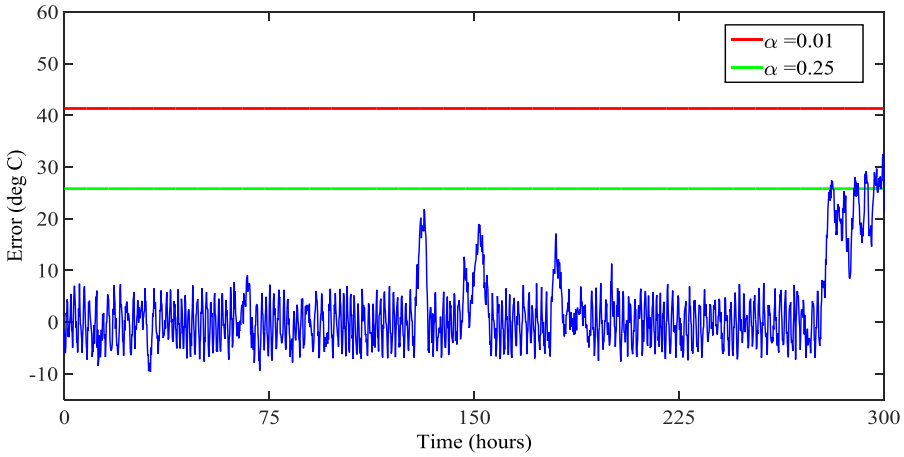

Figure 5.12 Residual signal of the generator winding temperature between SCADA data and model prediction

Components	Maintenance type	Cost (£)
Gearbox	Repair	5000
Generator	Repair	50000
Converter	Repair	12000
Pitch actuator	Repair	8000
Bearing	Repair	5000
Blade	Repair	4000

Table 5.1 Typical maintenance cost for different repair types [99]

Components	Downtime (days)
Gearbox	14
Generator	3
Converter	6
Pitch actuator	4
Bearing	11
Blade	4

Table 5.2 Downtime caused by different subsystems [15]

After fault degree estimation, AHP is then adopted to achieve health condition estimation considering many factors. In this case study, three criterion elements are selected including fault degree, maintenance cost and maintenance time. Table 5.1 and table 5.2 provide detailed information about typical maintenance costs for different repair types and downtime caused by different subsystems respectively. As above mentioned, it defines that significance of criterions C_1, C_2, C_3 are high (C_1=9), medium (C_2=5) and low (C_3=1). We define fault degree has high significance of criterion (C_1=9), maintenance time and maintenance cost are assumed as medium (C_2=5) and low (C_3=1) significance of criterion, respectively. Meanwhile, we also define that the residual signal over $d_k(0.01)$ from ELM model is high (C_3=9); the value between $d_k(0.01)$ and $d_k(0.25)$ is medium (C_2=5); and below $d_k(0.25)$ is low (C_1=1); the downtime of subsystems over 10 days is high (C_3=9); the downtime of subsystems between 10 days and 5 days is medium (C_2=5), and below 5 days is low (C_1=1); the maintenance cost of subsystems over £30000 is high (C_3=9); the maintenance cost of subsystems between £30000 and £10000 is medium (C_2=5), and below £10000 is low (C_1=1).

Six 2.5MW wind turbines are selected including four healthy wind turbines and two faulty wind turbines. The fault characteristic of two faulty wind turbines follow the previous fault degree level estimation results. Thus, through the proposed AHP

method, it can be obtained that the weight of the wind turbine with gearbox fault is 0.6924 via using equation (5-12); meanwhile, the weight of the wind turbine with generator fault is 0.3076. This means that the wind turbine with the gearbox fault is more serious than the winding fault for the wind turbines.

5.5.3 Case study about proposed power dispatch strategy

Fig 5.13 illustrates the wind speed for wind turbines in the wind farm within one day. According to the wind speed, the power output based on different power control strategies shown in Fig 2.3 are then calculated. In this chapter, we just compare the percentage power control strategy and the MPPT power control strategy under given wind condition, and the results are shown in Fig 5.14. The red line and blue line describe the power output of wind turbines operating in MPPT mode and 80% power reserve mode, respectively. In this study case, we assume that the network operator adopts 80% percentage mode power reserve strategy, hence resulting in blue line power output curve shown in Fig 5.14.

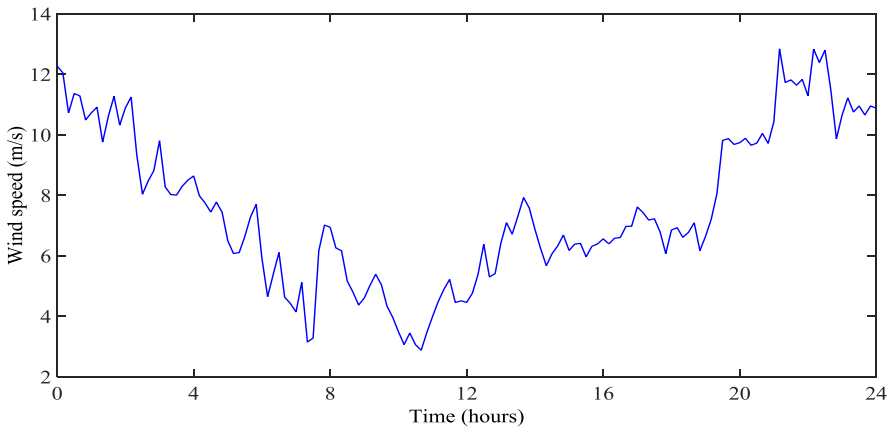

Figure 5.13 Wind speed for wind turbines in the wind farm within one day

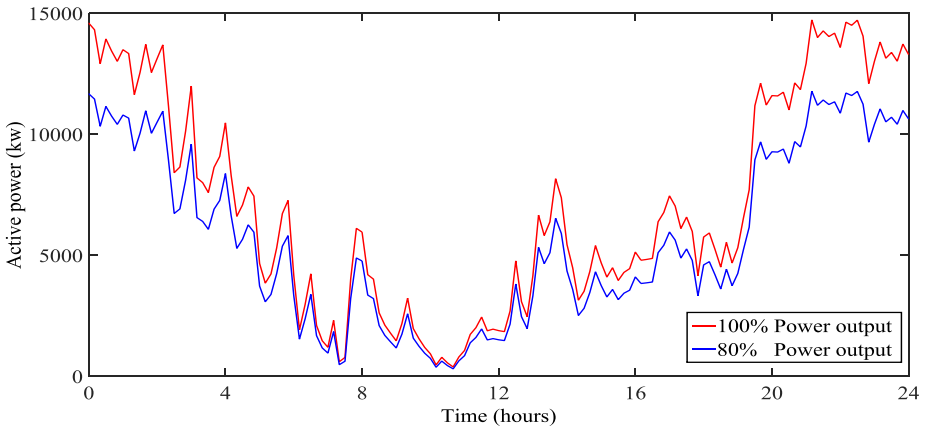

Figure 5.14 Comparison of the percentage power control and the MPPT power control under the given wind condition

Fig. 5.15 provides power output of the six wind turbines (wind turbine 5 with gearbox fault and wind turbine 6 with generator fault) following 80% percentage mode power control. It is worth noting that the power output for the wind turbines has some minute differences under given wind speed condition, due to the wake effect in wind farm [60]. The torque of generator for each wind turbine can be calculated by using equation from [7], as shown in Fig 5.16, in response to power demand for the farm. It can be seen that the generator torque for each turbine is almost same; thus this control strategy does not benefit to reduce mechanical load of faulty wind turbines.

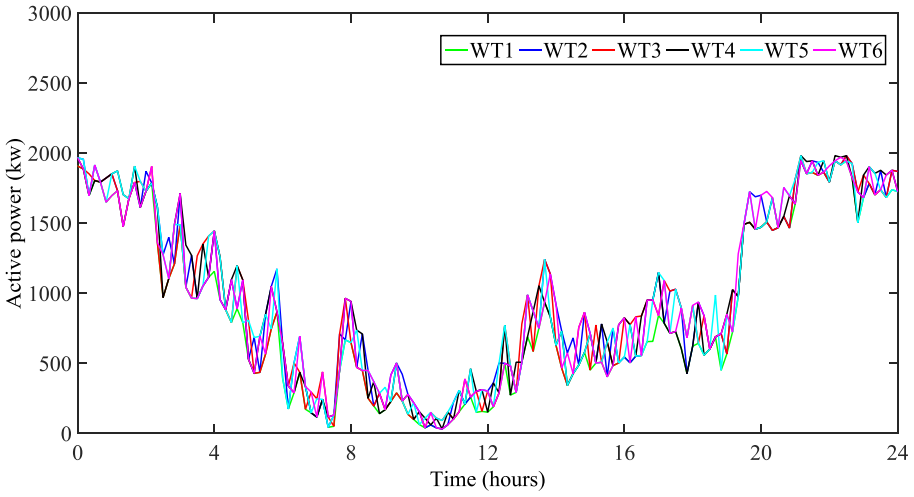

Figure 5.15 Power output from the turbines using conventional proportional allocation

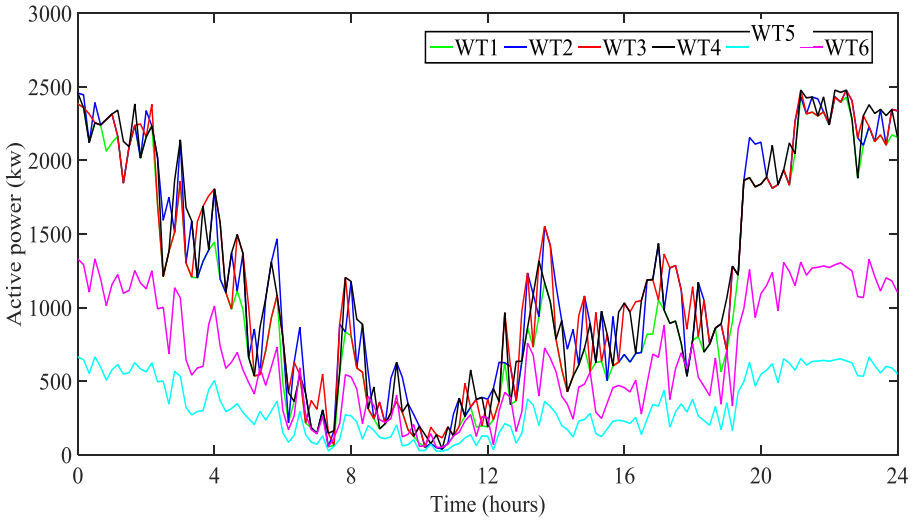

Figure 5.16 Corresponding torque outputs from the turbines using conventional proportional allocation method

Fig 5.17 illustrates the proposed optimizing control of the wind farm power output based on estimating health condition. In this case, the power distribution for faulty wind turbines adopts one to two proportional allocation (wind turbine 5 allocates less power due to more serious health condition) following principle of the equation (5-13); four healthy wind turbines operate in MPPT mode, and two faulty wind turbines are in reducing mode. It can be seen that four healthy wind turbines operate in MPPT mode to produce as much power as possible in order to meet demand specified by the network operator. Meanwhile, the two faulty turbines work in power-reducing mode in order to reduce mechanical load while still producing power balance between the network demand and the power output of the healthy wind turbines (operating in MPPT mode). Fig 5.18 describes corresponding torque of generator based on the proposed method. Clearly, it can be seen that generator torque of faulty wind turbines significantly decrease, due to reducing power output. The wind turbines operating in MPPT mode will not significantly reduce their

component life expectancy vs operating them at 80%, because the rated power output is in MPPT mode.

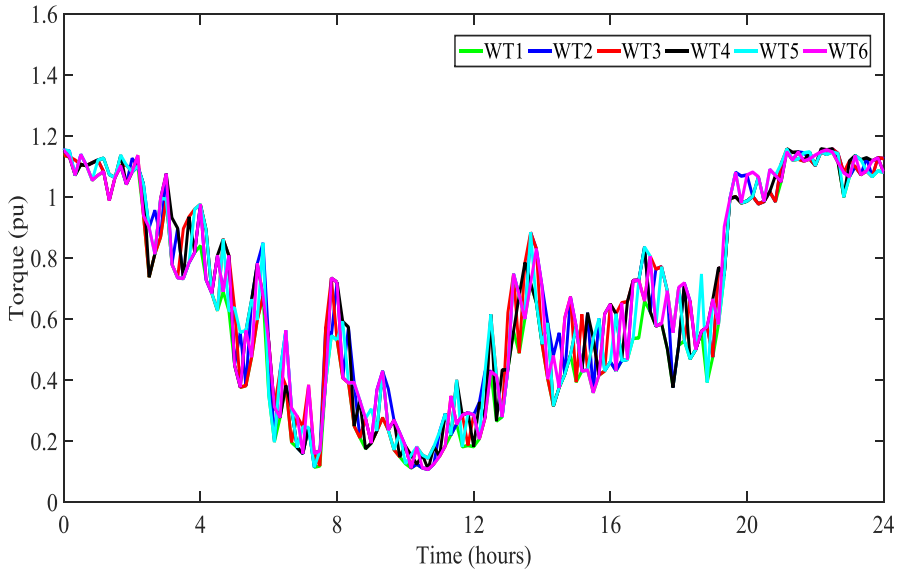

Figure 5.17 Power outputs from each turbine using the proposed optimizing control of the power output

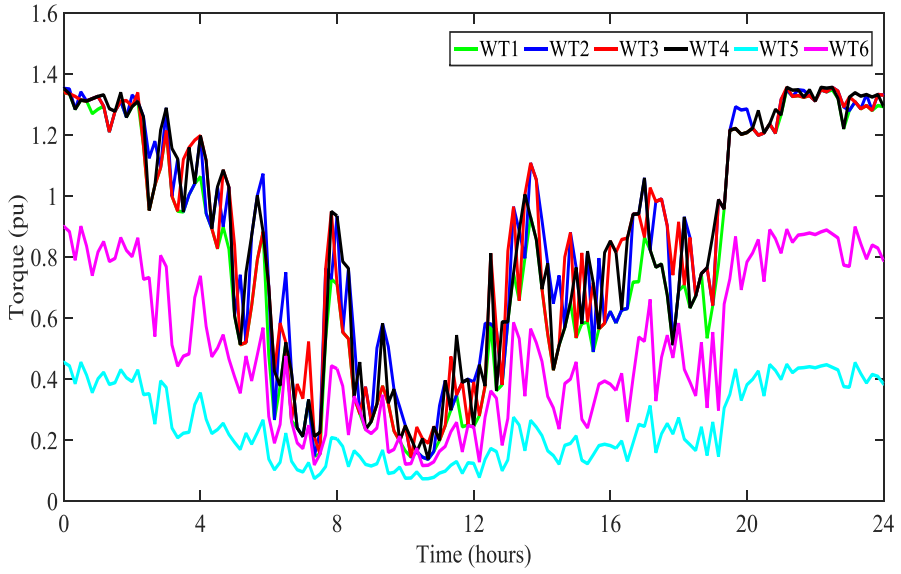

Figure 5.18 Corresponding torque outputs from each turbine using proposed the optimizing control of the power output

5.6 Summary and discussion.

This chapter has presented an optimizing wind farm power output control based on estimating health condition of wind turbines. It consists of three sections, including fault degree estimation, health condition estimation and optimizing power dispatch strategy. In order to demonstrate effectiveness of the proposed method in fault degree estimation section, two types of representative abnormal condition (long-term system aging and short-term component fault) from two wind turbines are selected in this chapter. The SCADA data, including the temperatures of gearbox oil, gearbox bearing and drivetrain main bearing obtained from an operational commercial wind farm have been used. Fault identification is achieved by using models derived from these data. The residual signals are the difference between the actual output and the predicted output, which are caused by system aging and fault, thus providing an early warning of impending failure. The residual temperature signal from the model-based CM system is revised by a physical kinetic energy correction model, which normalizes the temperature change at different power point to the value at the rated power output. The corrected values can provide a more sensitive trend indicative of signal changes. The results show that, using the Bonferroni method, a more accurate estimate of the health condition of drivetrain can be achieved, thus facilitating a more reliable fault diagnosis

Chapter6. shunt active power filter applied in wind farm

Shunt active power filters (SAPFs) have been widely used to improve power quality of the grid by mitigating harmonics injected from nonlinear loads. Harmonics will cause abnormal temperature rising and torque ripple in wind turbine generators, which reduces reliability and lifetime of the wind power system. This chapter presents a new method for improving the performance of SAPFs using neutral point clamped (NPC) three-level inverters. NPC three-level inverters often suffer excessive voltage fluctuations at the neutral-point of DC-link capacitors, which may damage switching devices and cause additional high harmonic distortion of the output voltage. In order to solve the problem, two compensating schemes are proposed to restrict voltage fluctuation in inverters. The first is voltage dependent, adopting a voltage compensation method, while the second is current dependent, using a current compensation method. This chapter describes the respective circuit architectures and principles of operation. Corresponding models are mathematically formulated and evaluated under typical balanced and unbalanced working load conditions. The results show that both schemes are able to alleviate considerably voltage oscillations and hence harmonic distortions, and the current compensated NPC inverter outperforms the voltage compensated NPC inverter. Consequently, it is shown that the proposed approaches are effective and feasible for improving power quality of the grid when connected to nonlinear loads.

6.1 Shunt active power filters

Recently, these has been a significant increase in the installation of distributed generation (DG) systems due to the deregulation of utilities, environmental constraints, and concerns regarding climate change. This type of power generation system, as shown in Fig. 6.1, can provide electric power at or on a site closer to end users [100]. However, harmonic-related problems have become a key concern because DG generators, such as wind and photovoltaics (PV), are coupled to power electronic converters and nonlinear loads [101, 102]. Harmonics will cause abnormal temperature rising and torque ripple in wind turbine generators, which reduces reliability and lifetime of the wind power system. In this regard, shunt active power filters (SAPFs) are widely used to mitigate these harmonic distortion problems in the grid.

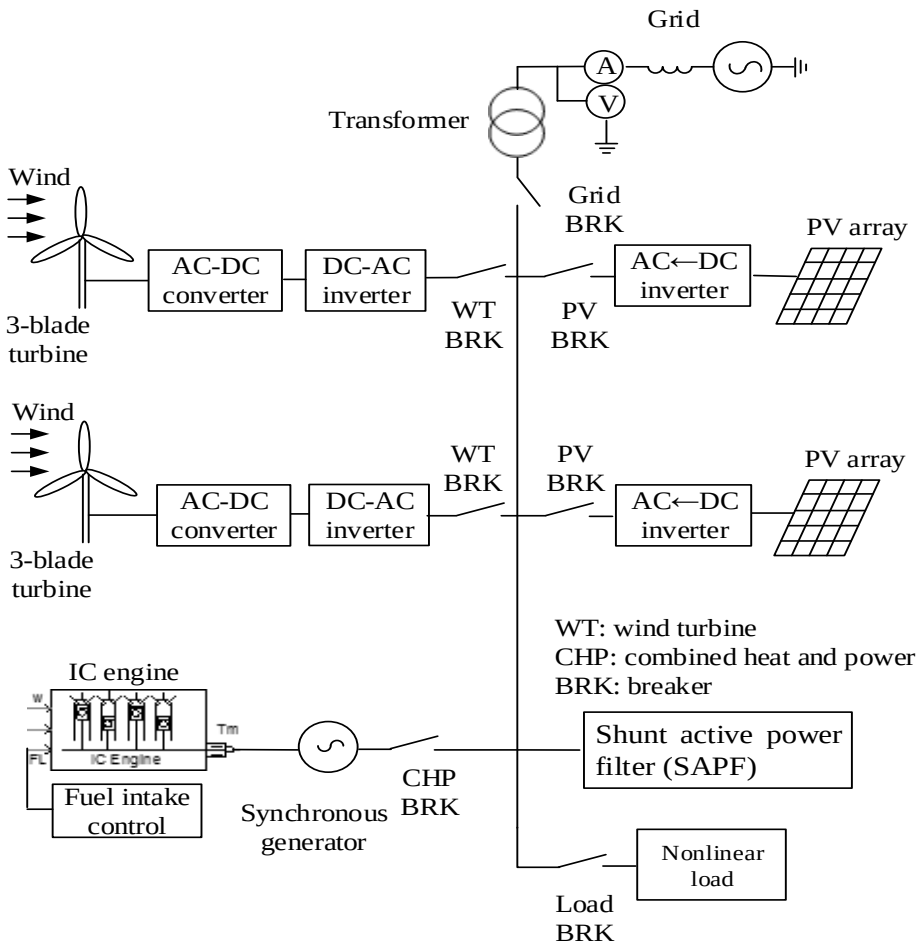

Figure 6.1 Schematic diagram of a distributed generation system

Fig 6.2 shows a SAPF based on the NPC three-level inverter. In this figure, u_{sa}, u_{sb}, u_{sc} are the three-phase alternating-current supplies; the load is nonlinear, generating harmonic currents; i_{sa}, i_{sb}, i_{sc} and i_{La}, i_{Lb}, i_{Lc} are grid currents and load currents, respectively; i_{ca}, i_{cb}, i_{cc} are compensation currents provided by the SAPF, which are used to eliminate harmonic currents in the grid. The SAPF is essentially composed of two major components, namely a conventional NPC three-level inverter and an associated control scheme. In the inverter circuit, K_1, K_2, K_3, K_4 are IGBT (insulated gate bipolar transistor) power switches, while DZ_1, DZ_2 are clamp diodes; note that only the components of one inverter arm are labelled for simplicity. The DC bus voltage is split in half using two DC capacitors, C_1 and C_2, and into three voltage levels, u_s, 0, and $-u_s$, via clamping diodes. The control scheme detects the load currents in real time, which are used to calculate command signals for the IGBT switches. The inverter then works as a signal amplification circuit, producing

appropriate compensation currents. This compensation current is equal but opposite to the harmonic currents, which can be overlaid to the load currents eliminating the harmonic currents generated by the nonlinear load.

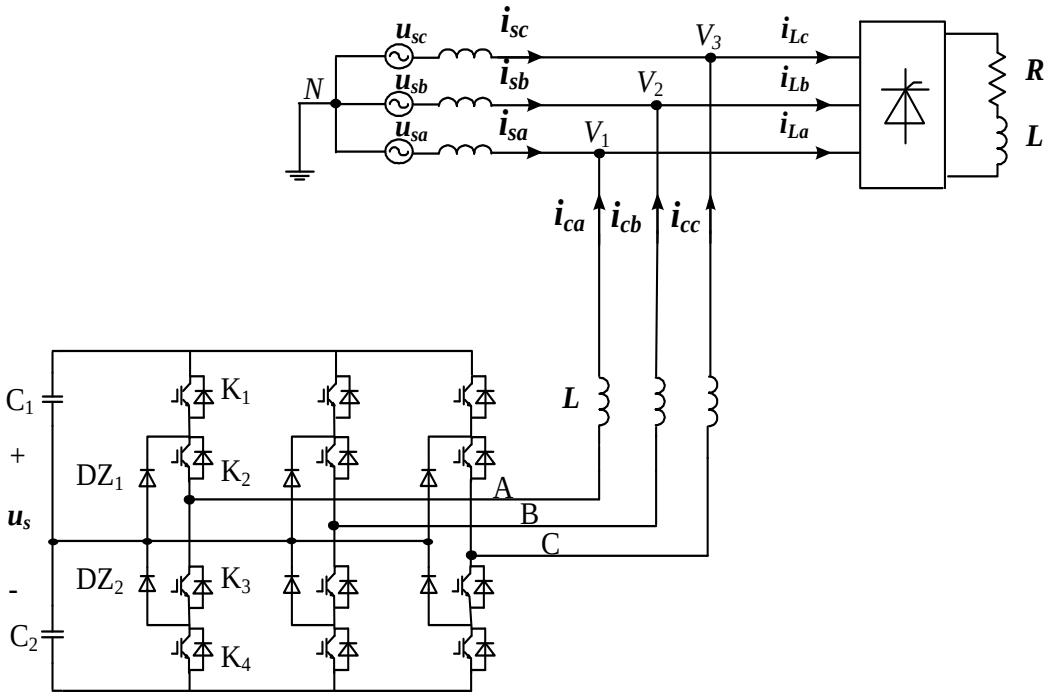

Figure 6.2 A SAPF based on the neutral point clamped (NPC) three-level inverter

6.2 Neutral point clamped three-level inverter

6.2.1 The structure of NPC three-level inverter

Compared to two-level voltage-source inverters used in SAPFs, three-level voltage-source inverters are able to bear higher voltage classes and operate with lower harmonic distortion and at lower switching frequencies. Three-level inverters therefore offer better performance, in particular for medium-voltage applications [103]. In terms of topological structure, three-level inverters can be classified as one of three distinct types, namely diode clamped multilevel inverters, clamping capacitor multilevel inverters, and isolated H-bridge multilevel inverters [104, 105]. Neutral point clamped (NPC) three-level inverters [106] may be classified as a type

of diode clamped multilevel inverter. The most commonly used NPC three-level inverter circuit [107-109] is shown in Fig. 6.3, where it is incorporated into a SAPF.

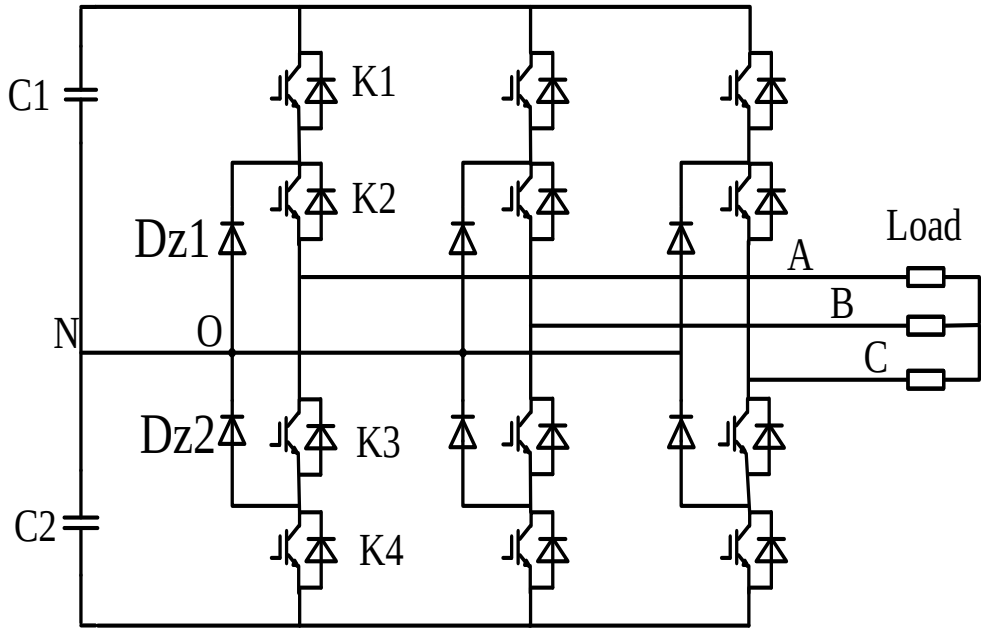

Figure 6.3 Schematic diagram of the neutral point clamped (NPC) three-level inverter

Table 6.1 illustrates the device On-Off state (phase A) definition of the NPC three-level inverter. [P] presents two switches in the up-side bridge arm at On state, while two switches in the down-side bridge arm is at Off state, generating u_s phase A output voltage ; [N] illustrates two switches in the down-side bridge arm at On state, while two switches in the up-side bridge arm is at Off state, producing $-u_s$ phase A output voltage; otherwise, [O] means two switches in the middle of the bridge arm is at On state, while the other two switches is at Off state, making phase A output voltage zero. Clearly, K_1 and K_3 switches operate in alternate switching mode; similarly, the same switching mode is applied in K_2 and K_4 switches.

Model condition	Device On-Off state (phase A)				Voltage (V_{AN})
	K_1	K_2	K_3	K_4	
[P]	On	On	Off	Off	u_s
[O]	Off	On	On	Off	0
[N]	Off	Off	On	On	$-u_s$

Table 6.1 Device On-Off state (A phase) definition of the NPC three-level inverter

An example of the gate drive signal, transferring from mode [O] to mode [P] in phase A is shown in fig 6.4. The thick lines and thin lines mean power switches are On and Off respectively. V_{g1}, V_{g2}, V_{g3}, and V_{g4} are the gate drive voltage for power switches K_1, K_2, K_3, and K_4. The dead-zone times δ are set during the switches mode changing, in order to avoid short circuit.

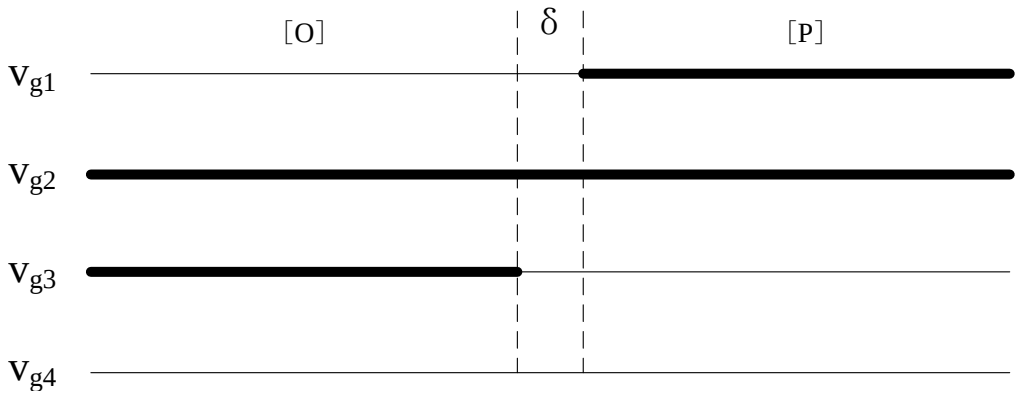

Figure 6.4 Gate drive signal of the NPC three-level inverter

In a NPC three-level inverter, the neutral point of the DC-link capacitors and the neutral point of the three-phase bridge circuit are linked together directly. The neutral-point voltage of the three-phase bridge arm will vary because of the

oscillation of the neutral-point voltage in the DC-link. The problem is inherent because there is a neutral-point current flowing in to or out of the neutral points in the circuit [110]. The varying current causes a charge-discharge phenomenon associated with the capacitors through the neutral-points in the circuit, thus resulting in a fluctuation in the neutral-point voltage. Consequently, the voltage ripples produced will affect the capability of the NPC three-level inverter to work efficiently [111, 112]. Furthermore, excessive fluctuations of the DC-link voltage increase voltage stresses on the switching devices and increases the total harmonic distortion (THD) of the output current, which may limit potential engineering applications of this type of inverter.

There are three main factors that may cause oscillations in the neutral-point voltage in the DC-link branch. Firstly, the capacitance associated with the DC-link capacitors may become unbalanced after use for extended periods of time; DC link capacitors are required to endure high ripple currents leading to self-heating, which, in addition to high ambient operating temperatures, can result in the deterioration of the electrolyte material and the loss of electrolyte by vapour diffusion. Secondly, a critical factor for the inverter to work is delivery of the gate drive signals to the switching devices, as controlled by the switching frequency. Any switching delay will cause load current imbalance. Thirdly, nonlinear loads also cause harmonics to appear in the load current, which may in turn inject harmonics back to the inverter.

6.2.2 The operational mode of NPC three-level inverter

As mentioned above, the essential reason that causes a fluctuation in the neutral-point voltage is a neutral-point current flowing in to or out of the neutral points in the circuit. The varying current will lead to charge-discharge phenomena associated with the capacitors through the neutral-points in the circuit, resulting in a fluctuation in the neutral-point voltage. Thus, operational mode of NPC three-level inverter is necessary to be analysed. Taking phrase A as an example, the analysis is divided into two parts, including phrase A current $i_A>0$ and phrase A current $i_A<0$.

1) When phrase A current is i_A>0, the operating flow charts are provided in fig 6.5.

In mode [O], the power switches K_2 and K_3 are in the condition of On state; while the power switches K_1 and K_4 are Off. The current flows across clamping diode D_{Z1}, the voltage applied to power switch K_1 and K_4 are E respectively. Clearly, there is a current flowing out of the neutral points.

In dead-zone times δ, the power switch K_3 is Off, keeping i_A current path invariability. The voltage applied to power switch K_3 and K_4 are E/2 respectively. The current also flows out of the neutral points, thus resulting in fluctuation in the neutral-point voltage.

In mode [P], the power switches K_1 is in the condition of On state, which makes clamping diode D_{Z1} to bear backward voltage. The current is through the power switches K_1 and K_2. In this mode, there is no current flowing in to or out of the neutral points in the circuit, the neutral-point voltage would therefore be no change.

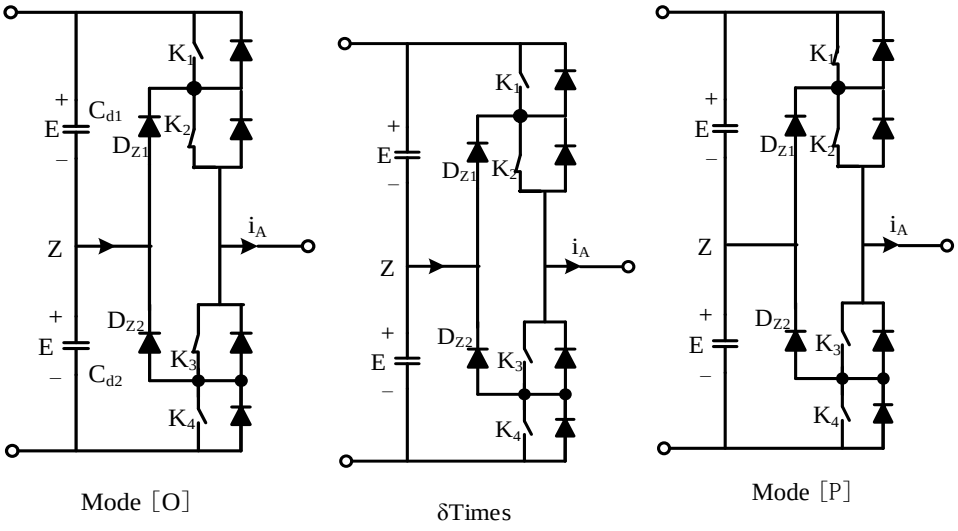

Figure 6.5 Operating flow charts under phrase A current i_A>0

2) When phrase A current i_A<0, the operating flow charts are provided in fig 6.6.

In mode [O], the power switches K_2 and K_3 are in the condition of On state; while the power switches K_1 and K_4 are Off. The current flows across clamping diode D_{Z2}, the voltage applied to power switch K_1 and K_4 are E respectively. Clearly, there is a current flowing in the neutral points.

In dead-zone times δ, the power switch K_3 is Off, keeping i_A current path invariability. The voltage applied in power switch K_3 and K_4 are E/2 respectively. The current also flows in the neutral points, thus resulting in fluctuation in the neutral-point voltage.

In mode [P], the power switches K_1 is in the condition of On state. Because of the. phrase A current $i_A<0$, the current goes through the diode D_1 and D_2. In this mode, there is no current flowing in to or out of the neutral points in the circuit, the neutral-point voltage would therefore no change.

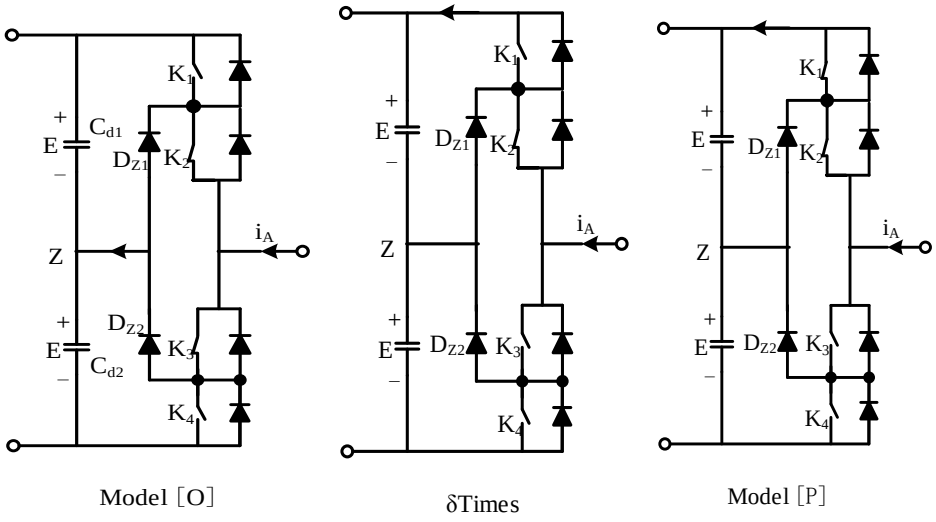

Figure 6.6 Operating flow charts under phrase A current $i_A<0$

6.2.3 The control strategy of NPC three-level inverter

As mentioned above, three modes, including [P], [O] and [N], are able to be used to describe operational mode of each bridge arm. For three-phrase bridge arm, there

are twenty-seven kinds of combinations. Thus, the control scheme of the NPC three-level inverter can be determined by analysis different operational mode. Fig 6.7 shows the schematic diagram of space voltage vector pulse-width modulation (SVPWM) of NPC three-level inverter, which is the most widely used control strategy for NPC three-level inverter. From the aspects of vector length, space voltage vector can be divide into four parts.

1) Zero-vector including $\overrightarrow{V_0}$. The amplitude of zero-vector is zero.

2) Small-vector including $\overrightarrow{V_1}$, $\overrightarrow{V_2}$, $\overrightarrow{V_3}$, $\overrightarrow{V_4}$, $\overrightarrow{V_5}$ and $\overrightarrow{V_6}$. The amplitude of small-vector is $\frac{V_d}{3}$.

3) Medium-vector including $\overrightarrow{V_7}$, $\overrightarrow{V_8}$, $\overrightarrow{V_9}$, $\overrightarrow{V_{10}}$, $\overrightarrow{V_{11}}$, and $\overrightarrow{V_{12}}$. The amplitude of small-vector is $\frac{\sqrt{3}V_d}{3}$.

4) Large-vector including $\overrightarrow{V_{13}}$, $\overrightarrow{V_{14}}$, $\overrightarrow{V_{15}}$, $\overrightarrow{V_{16}}$, $\overrightarrow{V_{17}}$ and $\overrightarrow{V_{18}}$. The amplitude of small-vector is $\frac{2V_d}{3}$

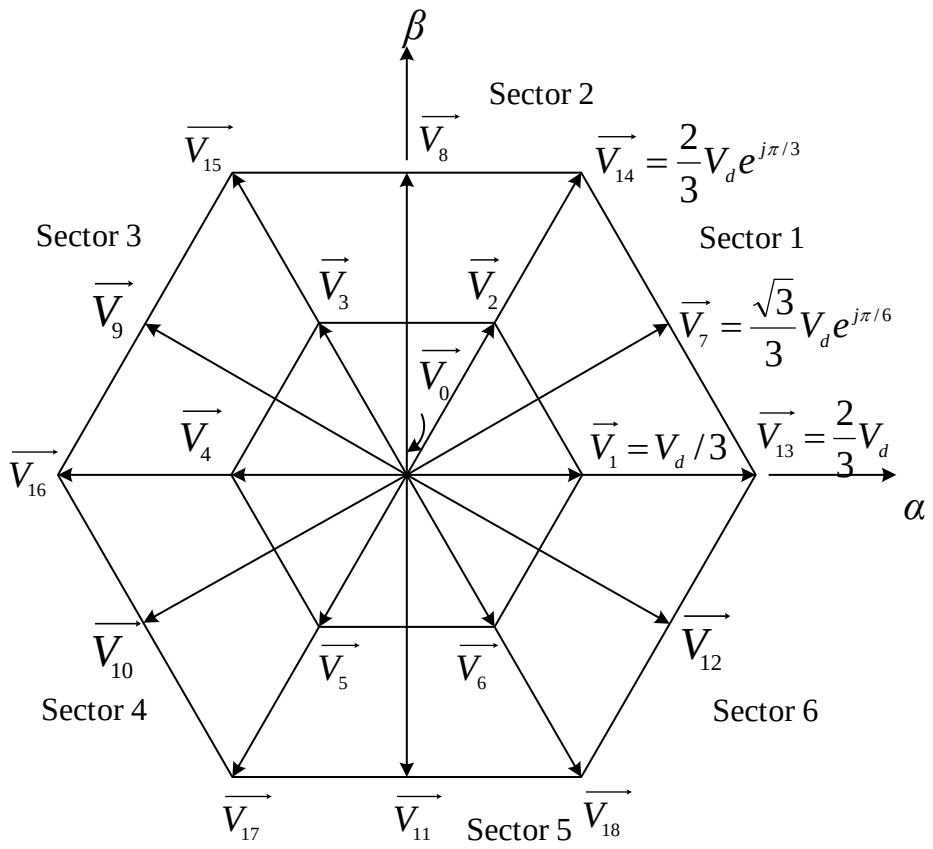

Figure 6.7 Schematic diagram of space voltage vector pulse-width modulation of NPC three-level inverter

In order to conveniently calculate action time of space voltage vector, the schematic diagram of space voltage vector modulation of NPC three-level inverter is usually split into six triangle sectors, and each triangle sector can be further divide into four smaller triangle sectors.

SVPWM algorithm for the NPC three-level inverter is based on voltage-second balance theory [113-115]. More specifically, it is the product of the given vector $\overrightarrow{V_{ref}}$ and sampling period T_s. The given vector $\overrightarrow{V_{ref}}$ is consisted of three static vectors. When the $\overrightarrow{V_{ref}}$ is in sectors 1, static vectors $\overrightarrow{V_1}$, $\overrightarrow{V_2}$, and $\overrightarrow{V_7}$ compound the given vector $\overrightarrow{V_{ref}}$, and T_a, T_b and T_c are the action time on corresponding static vectors.

$$\begin{cases} \overrightarrow{V_1}T_a + \overrightarrow{V_7}T_b + \overrightarrow{V_2}T_c = \overrightarrow{V_{ref}}T_s \\ T_a + T_b + T_c = T_s \end{cases} \quad (6\text{-}1)$$

Static vectors $\overrightarrow{V_1}$, $\overrightarrow{V_2}$, and $\overrightarrow{V_7}$ can also be describe as follow:

$$\overrightarrow{V_1} = \frac{1}{3}V_d \quad (6\text{-}2)$$

$$\overrightarrow{V_2} = \frac{1}{3}V_d e^{j\frac{\pi}{3}} \quad (6\text{-}3)$$

$$\overrightarrow{V_7} = \frac{\sqrt{3}}{3}V_d e^{j\frac{\pi}{6}} \quad (6\text{-}4)$$

$$\overrightarrow{V_{ref}} = V_d e^{j\theta} \quad (6\text{-}5)$$

Where V_d is the amplitude of DC-link voltage.

Substituting (6-2), (6-3), (6-4) and (6-5) into (6-9) gives:

$$\frac{1}{3}V_d T_a + \frac{\sqrt{3}}{3}V_d e^{j\frac{\pi}{6}}T_b + \frac{1}{3}V_d e^{j\frac{\pi}{3}}T_c = V_d e^{j\theta}T_s \quad (6\text{-}6)$$

The equation (6-6) is able to be transferred to trigonometric function expression given in equation (6-7):

$$\frac{1}{3}V_d T_a + \frac{\sqrt{3}}{3}V_d\left(cos\frac{\pi}{6} + jsin\frac{\pi}{6}\right)T_b + \frac{1}{3}V_d\left(cos\frac{\pi}{3} + jsin\frac{\pi}{3}\right)T_c = V_{ref}(cos\theta + jsin\theta)T_s \quad (6\text{-}7)$$

The equation (6-7) can also be divided into real component and imaginary component illustrated as follow:

$$\begin{cases} \text{Real component: } \frac{2}{3}T_b + \frac{\sqrt{3}}{2}T_c = 3\frac{V_{ref}}{V_d}sin\theta T_s \\ \text{Imaginary component: } T_a + \frac{3}{2}T_b + \frac{1}{2}T_c = 3\frac{V_{ref}}{V_d}cos\theta T_s \end{cases} \quad (6\text{-}8)$$

Under the constraint condition $T_s = T_a + T_b + T_c$, the action times are obtained as follow:

$$\begin{cases} T_a = T_s[1 - 2m_a sin\theta] \\ T_b = T_s\left[2m_a sin\left(\frac{\pi}{3} + \theta\right) - 1\right] \\ T_c = T_s\left[1 - 2m_a sin\left(\frac{\pi}{3} - \theta\right)\right] \end{cases} \quad (6\text{-}9)$$

Where the value arrange of θ is from 0 to $\frac{\pi}{3}$; m_a is modulation factor.

$$m_a = \sqrt{3}\frac{V_{ref}}{V_d} \quad (6\text{-}10)$$

The maximum amplitude value of V_{ref} is maximum inscribed circle radius of the space vector hexagon.

$$V_{ref,max} = \frac{\sqrt{3}V_d}{3} \quad (6\text{-}11)$$

Substituting $V_{ref,max}$ into equation (6-10) gives

$$m_{a,max} = \sqrt{3}\frac{V_{ref,max}}{V_d} = 1 \quad (6\text{-}12)$$

The value arrange of m_a is

$0 \leq m_a \leq 1$

6.2.4 The analysis of oscillations in the neutral-point voltage

From section 6.2.2, it provides the information about the fluctuation in the neutral-point voltage caused by operational mode change in single phrase. In this section, the voltage oscillation in the neutral-point influenced by SVPWM control sector changing is analyzed.

Fig. 6.8 shows the diagram of the oscillation in the neutral-point voltage affected by operating in different sectors. It can be seen that the neutral-point voltage is no change, when the NPC three-level inverter works in zero-vector and large-vector sectors shown in Fig. 6.8 (a) and (e); in P type small-vector sector, the neutral-point voltage rises described in Fig. 6.8 (b), because of current flowing in the neutral-point; while in N type small-vector sector, the neutral-point voltage decreases

illustrated in Fig. 6.8 (c), because of current flowing out of the neutral-point; Fig. 6.8 (d) shows the NPC three-level inverter operating in middle-vector sector. There are both current flowing in and out of the neutral-point in this sector, resulting in uncertain voltage fluctuation in the neutral-point.

Clearly, in order to reduce the oscillation in the neutral-point voltage in the NPC three-level inverter, the small-vector and middle-vector sectors are try to avoid being used in SVPWM control strategy.

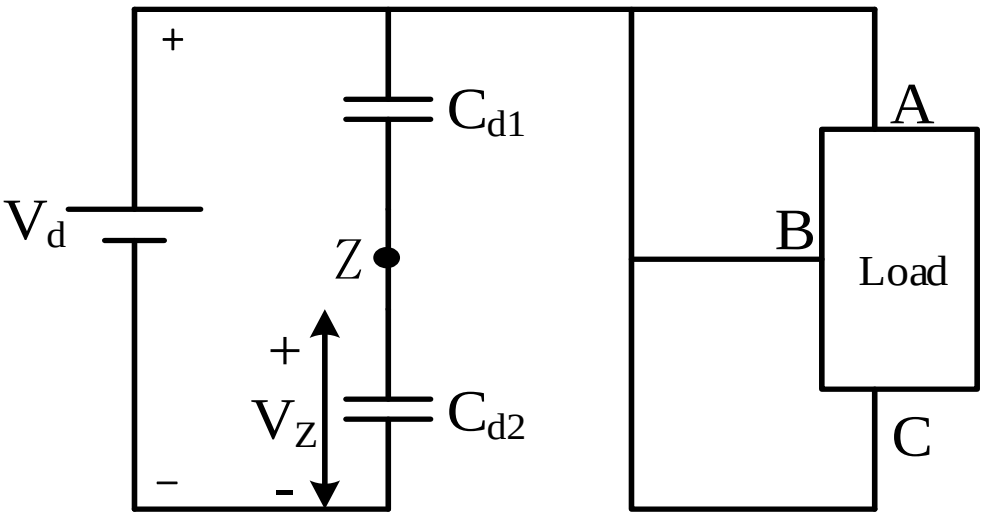

a. [PPP] mode

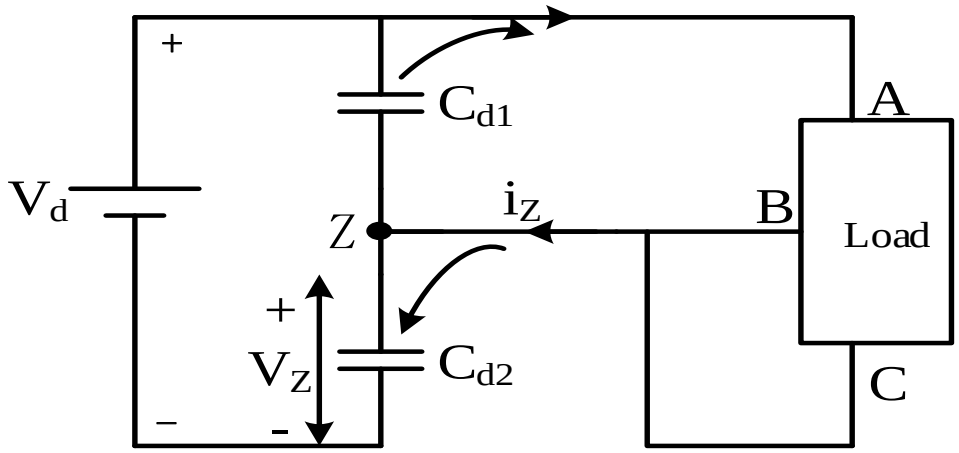

b. [P00] mode

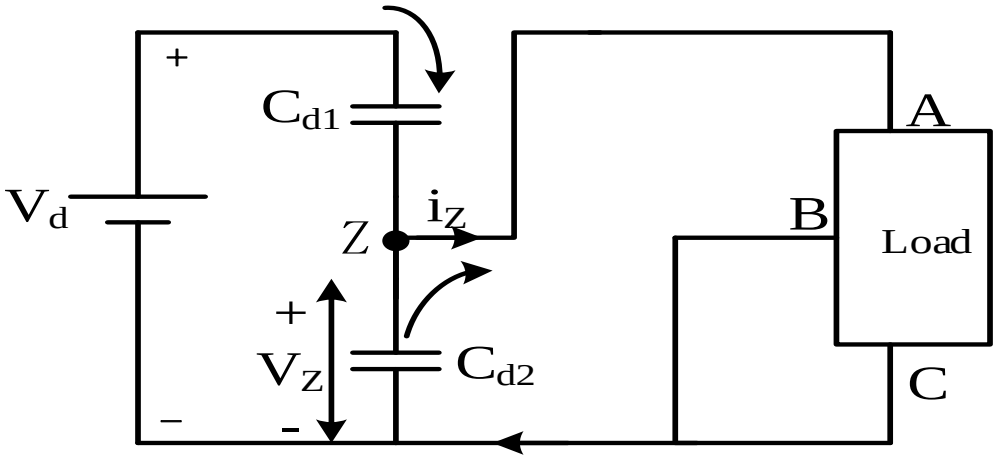

c. [0NN] mode

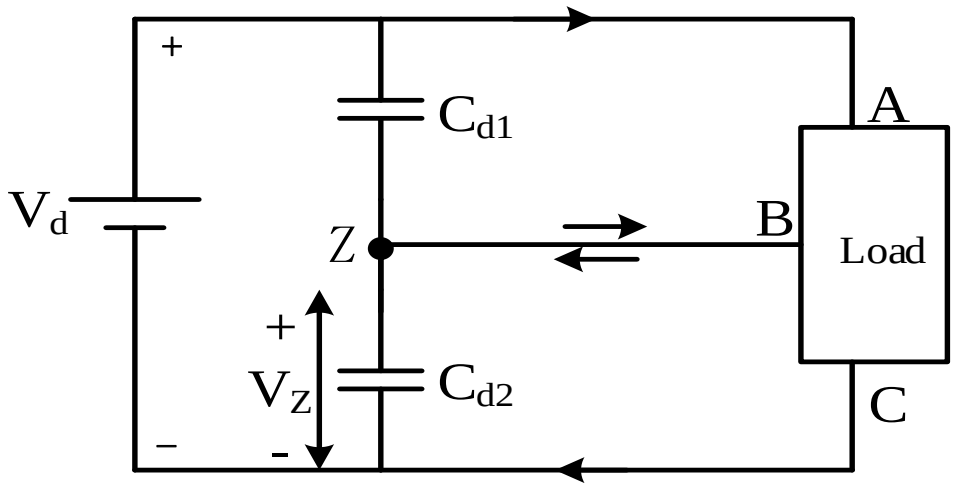

d. [PON] mode

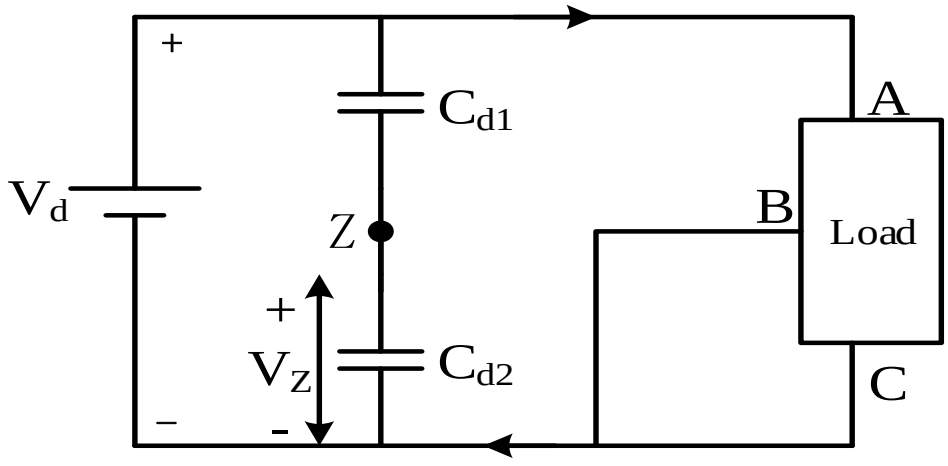

e. [PNN] mode

Figure 6.8 Diagram of the oscillation in the neutral-point voltage affected by operating in different sectors

In order to solve these problems, three main methods have been investigated to alleviate voltage oscillations. The first is through the use of two independent DC sources to ensure a stable and constant DC voltage across the inverter. The method is expensive [116], because the two independent DC sources require two isolation transformers. The second involves the design of improved control strategies; arguably the most widely used technique at present [117-119]. Among the control strategies, the best known is the SVPWM method [69, 70, 120-122]. The control strategy proposed in [70] replaces the P-type or N-type small switching states with other switching states that do not affect the neutral-point voltage. Reference [123] demonstrates the ability of the SVPWM method to balance the neutral point voltage for different regions of the space vector plane, while a new general model was introduced in [124] to investigate the theoretical and practical limitations of the balancing problems caused by space vector modulation. A control scheme based on a virtual space vector PWM method is proposed in [125] to control the neutral-point voltage fluctuation over the full range of the modulation index and load power factor, subject to the condition that the sum of the three-phase output currents equals zero. The third method reduces voltage oscillations through a change in circuit topology. This method incorporates auxiliary components in the traditional NPC three-level inverter circuit, and has proved to be able to achieve good performance to suppress excessive neutral-point voltage fluctuation effectively at low cost [126].

In this chapter, two new NPC three-level inverter topologies are proposed. The first is a voltage dependent NPC three-level inverter (VNPCI), which adopts a voltage compensation method to restrain the neutral point voltage fluctuation in the DC-link. The second method is a current controlled NPC three-level inverter (CNPCI), and uses a current compensation method. Both two new inverter topologies are incorporated in a SAPF.

6.3 Voltage compensated NPC inverter (VNPCI)

6.3.1 Inverter circuit

The schematic diagram of the VNPCI circuit is shown in Fig 6.9 Essentially, the circuit consists of two power units. Power unit 1 is associated with the conventional NPC three-level inverter, as described in the preceding section. In order to reduce excessive neutral-point voltage fluctuations across the DC-link capacitors, this chapter considers the application of an active voltage compensation method in which the controllable voltage source is used in series between the neutral point of the DC-link and the neutral point of the three-phase bridge circuit. This voltage source is used in order to compensate for voltage fluctuations across the three-phase bridge arm of the inverter. The voltage at the neutral-point of the three-phase bridge arm is detected in real time and compared with a reference voltage, producing an appropriate value for the compensation voltage. Subsequently, the voltage source generates an equal but opposite voltage, thus reducing the voltage fluctuation across the inverter.

Power unit 2 is an active voltage compensation device, which in essence is a single-phase full-bridge inverter. The device works as a controllable voltage source and is connected in series between the neutral point of the three-phase bridge arm and the neutral point of the DC-link through a coupling transformer. The variables u_o and u_N denote the neutral point voltage across the three-phase bridge arm and the DC-link capacitors, respectively; u_c and u_b are the voltages across the primary and secondary sides of the transformer, respectively, for which u_b is used as the compensating voltage; u_s is the DC-link voltage applied across the capacitors.

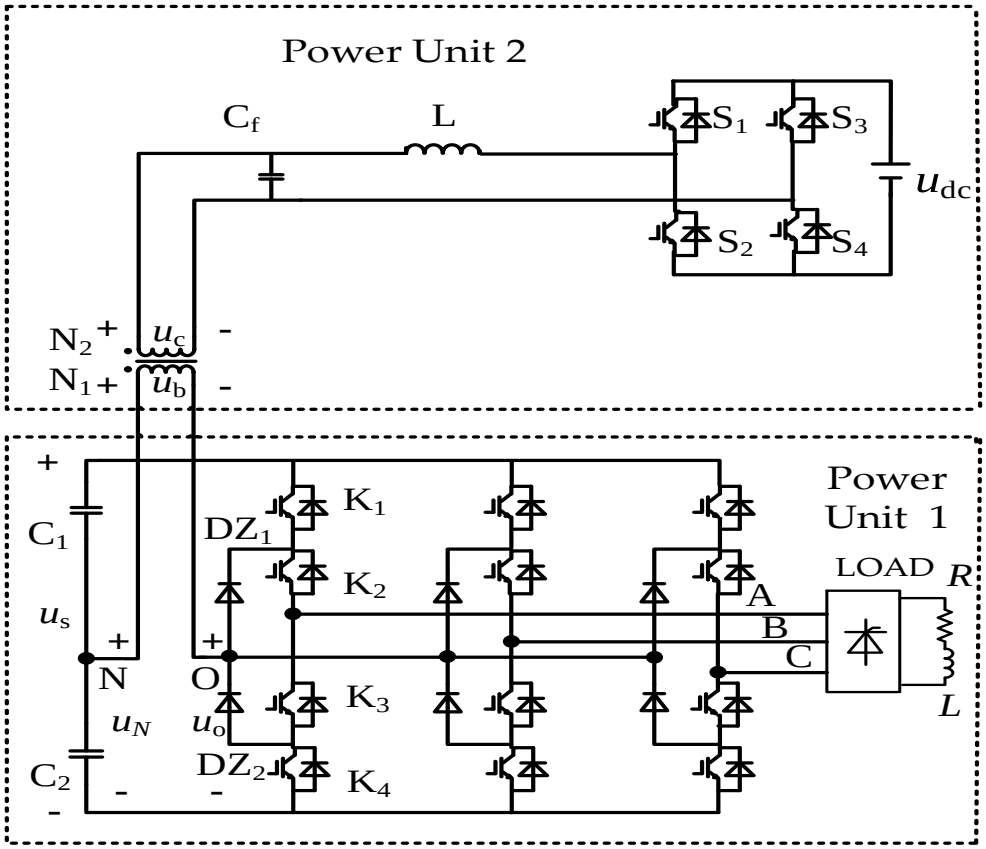

Figure 6.9 Schematic diagram of the voltage compensated NPC inverter

6.3.2 The active voltage compensation device

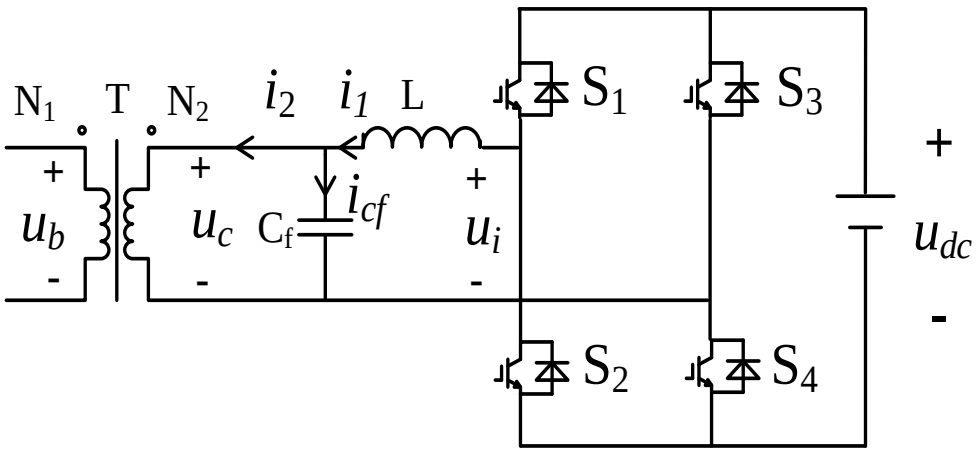

Figure 6.10 Schematic diagram of the active voltage compensation device

The voltage compensation device is shown in Fig. 6.10. It is composed of a single-phase full-bridge inverter circuit, where S_1, S_2, S_3, S_4 are IGBT power switches; T is the coupling transformer with a transformation ratio of n; the inductor L and the capacitor C_f form a LC filter that removes unwanted switching harmonics from the inverter output.

In the circuit illustrated in Fig. 6.10, u_{dc} is a DC voltage applied to the single-phase full-bridge inverter; u_i is the voltage output of the single-phase inverter; i_1 is the current through the filter inductor; i_2 is the transformer primary side current; i_{cf} is the current passing through the filter capacitor.

For an ideal transformer (i.e., no losses and no leakage flux between the primary and secondary windings),

$$u_b = n\left(u_i - L\frac{di_1}{dt}\right) \tag{6-13}$$

Hence, for the NPC inverter shown in Fig. 6.9, the voltage due to the introduction of the compensating voltage u_b can be obtained via the following equations. In the ideal situation, the three-phase bridge arm voltage u_o should be equal to half the DC-link voltage, i.e. 0.5 u_s.

$$u_N - u_b = u_O \tag{6-14}$$

$$u_N - n\left(u_i - L\frac{di_1}{dt}\right) = 0.5u_s \tag{6-15}$$

For the voltage output of the single-phase inverter u_i

$$u_i = S^* u_{dc} \tag{6-16}$$

Where S^* represents the switching function; if S_1 and S_4 are switched on while S_2 and S_3 are switched off, then S^*=1; if S_1 and S_4 are switched off while S_2 and S_3 are switched on, then S^*=-1.

Substituting (6-16) into (6-15) gives

$$u_N - n\left(S^* u_{dc} - L\frac{di_1}{dt}\right) = 0.5u_s \tag{6-17}$$

Therefore, the state equations of this active voltage compensation device can be described as,

$$\frac{du_c}{dt} = \frac{1}{C_f}(i_1 - i_2) \tag{6-18}$$

$$\frac{di_1}{dt} = \frac{1}{L}(u_i - u_c) \quad (6\text{-}19)$$

The resulting control scheme of the active voltage compensation device is shown in Fig. 6.11. In this diagram, the voltage $u_s^*(s)$ refers to the DC-link voltage under balanced capacitors; $u_n(s)$ is the DC-link neutral-point voltage measured in real time; $u_c^*(s)$ is the reference compensating voltage; $u_i(s)$ is the output voltage of the single phase full bridge inverter circuit; $u_c(s)$ is the transformer primary side voltage; $i_1(s)$ is the current in the filter inductor; and $i_2(s)$ is the transformer primary side current. The compensating voltage $u_c^*(s)$ is obtained by calculating the difference between the measured neutral-point voltage of DC-link and half of the ideal DC-link voltage. The error voltage between $u_c^*(s)$ and $u_c(s)$ is then used for generating PWM signals based on the triangular wave modulation method. This signal is then used to control the voltage output of the single-phase inverter. A PI controller, represented by K_p+K_i/s, is used because it can provide a compensating voltage output more accurately.

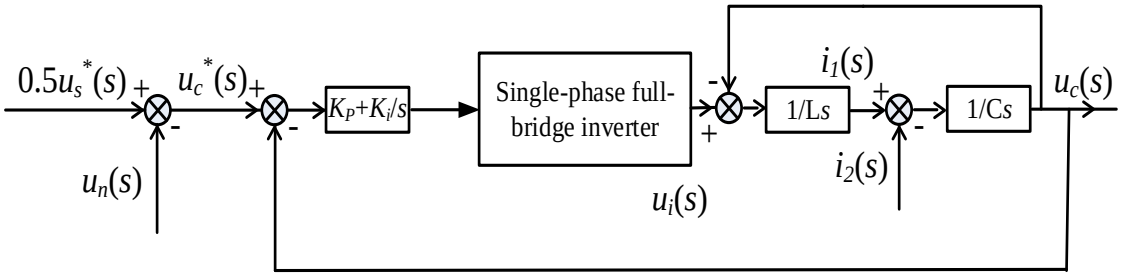

Figure 6.11 The control scheme for the active voltage compensation device

6.4 Current compensated NPC inverter (CNPCI)

6.4.1 Inverter circuit

As described above, the primary reason causing neutral-point voltage fluctuation across the DC-link is the current that flows in to or out of the neutral points in the circuit. The varying current will lead to charge-discharge phenomena associated with the capacitors through the neutral-points in the circuit, resulting in a fluctuation

in the neutral-point voltage. The voltage fluctuation can be alleviated naturally through the use of an active current compensation scheme in which a controllable current source is connected in shunt with one of the DC capacitors. This controllable current source is used to compensate for the current flow between the neutral point of DC-link capacitors and the neutral point of three-phase bridge circuit. It can further suppress neutral-point voltage fluctuations because, if this scheme is applied effectively, there is approximately zero current flowing between the neutral points in the inverter.

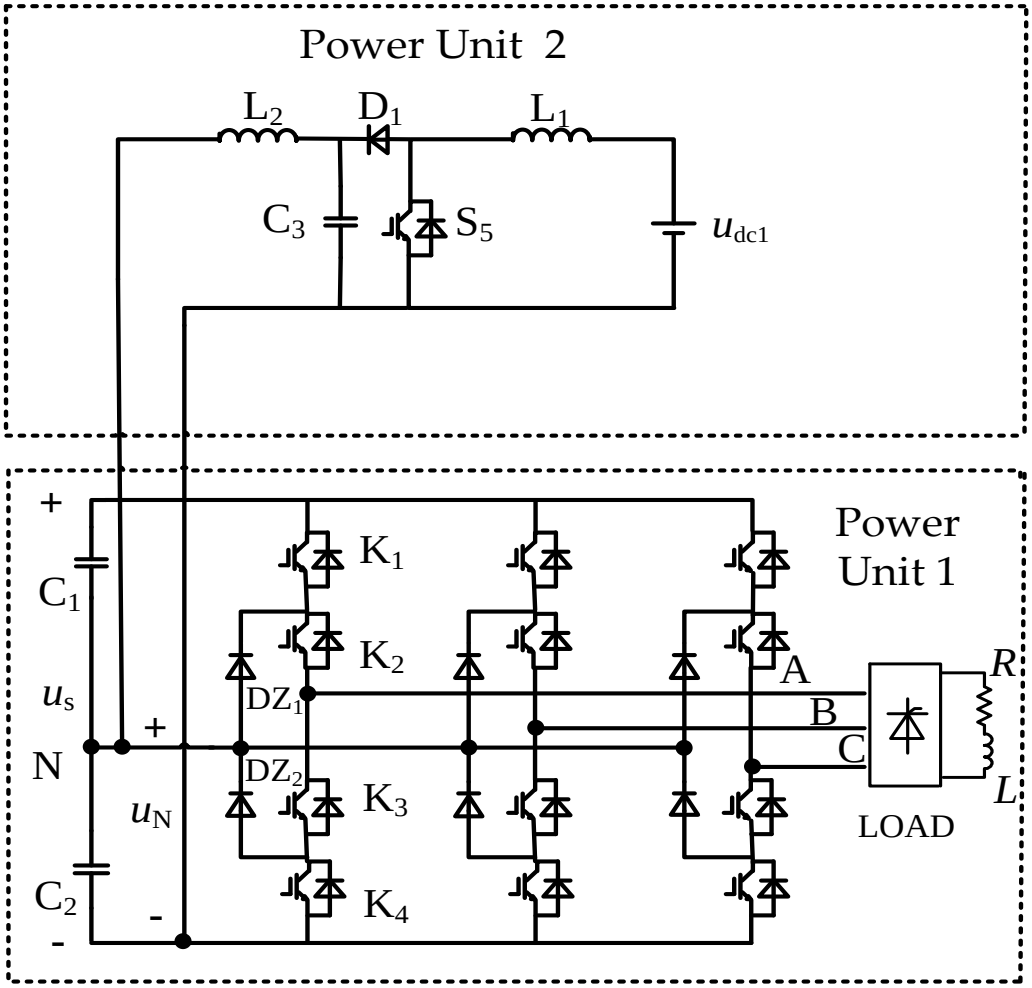

Figure 6.12 Schematic diagram of the current compensation NPC inverter

The schematic diagram of CNPCI is shown in Fig 6.12. It can be seen that the inverter consists of two parts: part 1 is the conventional NPC three-level inverter; and part 2 is an active current compensation device. The compensation device is essentially a boost DC/DC conversion circuit, which works as a current source. The current flowing between the neutral points of the inverter is detected in real time, and an equal but opposite current is generated through the current compensation device, offsetting the current flow. Thus, the charge-discharge phenomenon of DC capacitors through DC-link neutral-point can be restrained effectively. The effectiveness of the current compensation device relies on the voltage difference between the boost circuit and the DC-link, which is applied to the inductor (L_2 in Fig. 6.12), thus producing a compensation current for the DC capacitor.

6.4.2 The active current compensation device

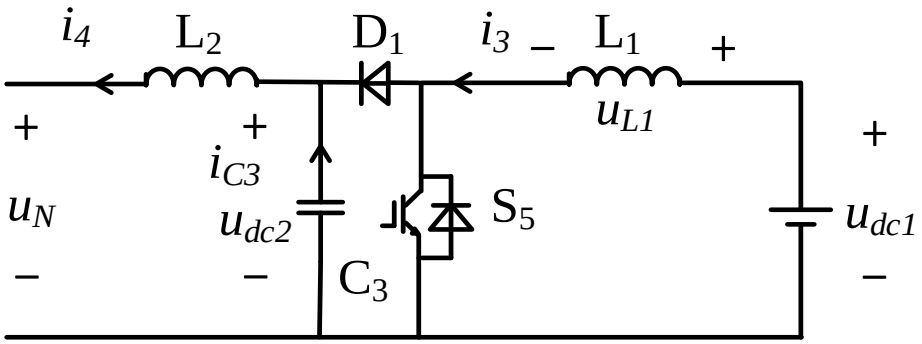

Figure 6.13 Schematic diagram of the active current compensation device

Fig 6.13 shows the proposed active current compensation device, essentially a boost DC/DC converter circuit, where S_5 is the IGBT power switch; D_1 is a diode preventing reverse current flow; L_1 is a power inductor used for energy storage; L_2 and C_3 form a LC filter for the circuit. In the circuit, u_{dc1} is the voltage input of the boost DC/DC converter; u_{dc2} is the voltage output of the boost DC/DC convertor; u_N is the DC-link neutral-point voltage; i_{c3} is the current in the capacitor C_3; i_3 is the

current in the inductor L_1; i_4 is the compensating current. Suppose $i_{c3(off)}$ and $i_{c3(on)}$ are the current in capacitor C_3 when the switching device S_5 is off and on, respectively; $u_{L1(off)}$ is the voltage across the inductor L_1 when the switching device S_5 is off while $u_{L1(on)}$ is the voltage across the inductor L_1 when the switch S_5 is on.

When the switch S5 is on, the state equations of the current compensation device can be described as,

$$\begin{cases} L_1 \frac{di_3}{dt} = u_{dc1} = u_{L_1(on)} \\ C_3 \frac{du_{dc2}}{dt} = i_4 = i_{c_3(on)} \end{cases} \tag{6-20}$$

When the switching device S5 is turned off, the above equation can be written as

$$\begin{cases} L_1 \frac{di_3}{dt} = u_{dc1} - u_{dc2} = u_{L_1(off)} \\ C_3 \frac{du_{dc2}}{dt} = i_4 - i_3 = i_{c_3(off)} \end{cases} \tag{6-21}$$

During one switching cycle, T_S, the average voltage across the inductor L_1 is,

$$\overline{u_{L_1}} = \frac{1}{T_s}\left[\int_t^{t+DT_s} u_{L_1(on)}(\tau)d\tau + \int_{t+DT_s}^{t+T_s} u_{L_1(off)}(\tau)d\tau\right] \tag{6-22}$$

$$\overline{u_{L_1}} = Du_{dc1} + (1-D)(u_{dc1} - u_{dc2}) \tag{6-23}$$

Where D represents the duty cycle of the switching device S_5, i.e., the proportion of time during which S_5 is operated.

During one switching cycle, the average current in the capacitor C_3 is equal to

$$\overline{i_{c_3}} = \frac{1}{T_s}\left[\int_t^{t+DT_s} i_{c_3(on)}(\tau)d\tau + \int_{t+DT_s}^{t+T_s} i_{c_3(off)}(\tau)d\tau\right] \tag{6-24}$$

$$\overline{i_{c_3}} = Di_4 + (1-D)(i_4 - i_3) \tag{6-25}$$

It is well known that the average voltage across an inductor and the average current in a capacitor should be zero during a switching cycle. Hence, under steady state, the current compensation device can be described as follows

$$\begin{cases} u_{dc2} = \frac{1}{1-D} u_{dc1} \\ i_4 = (1-D)i_3 \end{cases} \tag{6-26}$$

A control scheme, designed for the active current compensation device, can be derived from this model, as shown in Fig 6.14. In this circuit, u_{dc2}(s) is the voltage

output of the boost DC/DC converter; u_N(s) is the DC-link neutral-point voltage measured in real time. The reference compensating current i_c*(s) is obtained by the real-time detection of the current flowing between the neutral points of the inverter. The current i_c(s) is the compensation current generated by the boost circuit. The error current between i_c*(s) and i_c(s) is then used to generate PWM signals. This signal is based on the triangular wave modulation method, producing a compensating current at the desired level. As with the voltage compensation scheme, a PI controller, represented by K_p+K_i/s, is used because it generates a more accurate compensation current.

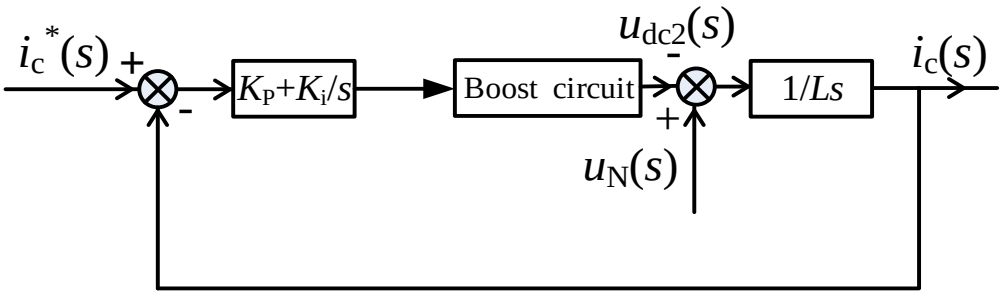

Figure 6.14 The control scheme for the active current compensation device

6.5 Results and analysis

6.5.1The inverters

Models of the voltage compensation device and the current compensation device have been built using Simulink SimPowerSystems, as described above and shown in Fig. 6.9 and Fig. 6.12, respectively. The parameters used in the models are given in Table 6.1. The DC-link voltage is 3 kV, a level commonly used in medium voltage power drives; the switching frequency for the NPC three-level inverter is 1 kHz; and the switching frequencies used to control the single-phase inverter for the voltage- and current-compensation device are both set to 10 kHz. In order to evaluate the dynamic performance of the proposed inverters, a nonlinear load is used in this study. This load consists of a three-phase rectifier with a resistive (4Ω)

and inductive (15mH) load shown in Fig. 6.15. The use of a nonlinear load increases the neutral-point voltage fluctuation of the DC-link, because the nonlinear load draws a current that is not necessarily sinusoidal, hence generating harmonic currents. The NPC three-level inverter is used with a constant voltage output control strategy, based upon space voltage vector modulation (SVPWM). The error voltage between the NPC three-level inverter output voltage and the reference voltage is processed by a PI controller, which is then used as the input signal for SVPWM to generate appropriate PWM signals. This control scheme has a higher efficiency for controlling the DC-side voltage than the equivalent sine pulse width modulation method.

Parameters of the VNPCI		Parameters of the CNPCI	
Parameters	Value	Parameters	Value
u_{dc}	500 V	u_{dc1}	100 V
C_f	50 μF	L_1	10 mH
L	0.4 mH	L_2	0.5 mH
		C_3	800 μF
Parameters of the NPC three-level inverter			
u_s	3000 V		
C_1, C_2	500 μF		

Table 6.2 Parameters used in the VNPCI and CNPCI inverters

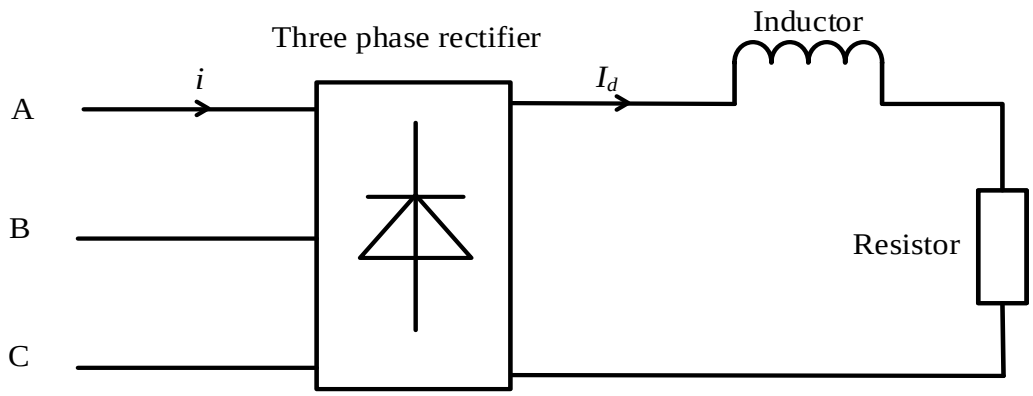

Figure 6.15 Schematic diagram of the nonlinear load

In real world applications, the load can be either in a balanced or unbalanced condition. An unbalanced load added to the three phase output voltage of an inverter can result in greater fluctuations in the neutral-point voltage across the DC-link. In the simulation, the inverters are initially connected to a balanced nonlinear load, and resistive (8Ω) and inductive (1.5mH) loads are then applied between phase A and phase B in order to evaluate the dynamic performance of the proposed compensation devices under a unbalanced load condition. The unbalanced load occurs at 10.05 s and lasts for 0.05 s.

Firstly, a conventional NPC three-level inverter, under balanced and unbalanced working load conditions, has been modelled and investigated. Fig. 6.16 (a) and (b) show the waveform of the neutral-point voltage u_o, the phase A to phase B voltage u_{AB} of the conventional inverter from simulation results. The neutral-point voltage fluctuation across the DC-link is severe, even in the balanced load condition; the range of the fluctuation reaches a value of 200V. During the unbalanced load condition, applied from 10.05s to 10.1s, it can be seen the neutral-point voltage fluctuation range increases to 300V. The THD (total harmonic distortion) of the output voltage waveform across the inverter is 45.30%.

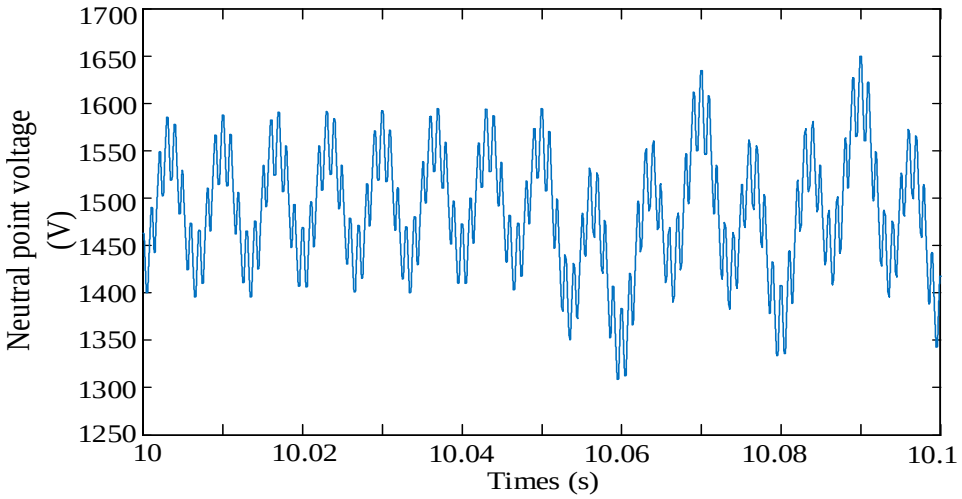

a. Voltage waveform of neutral-point voltage u_o

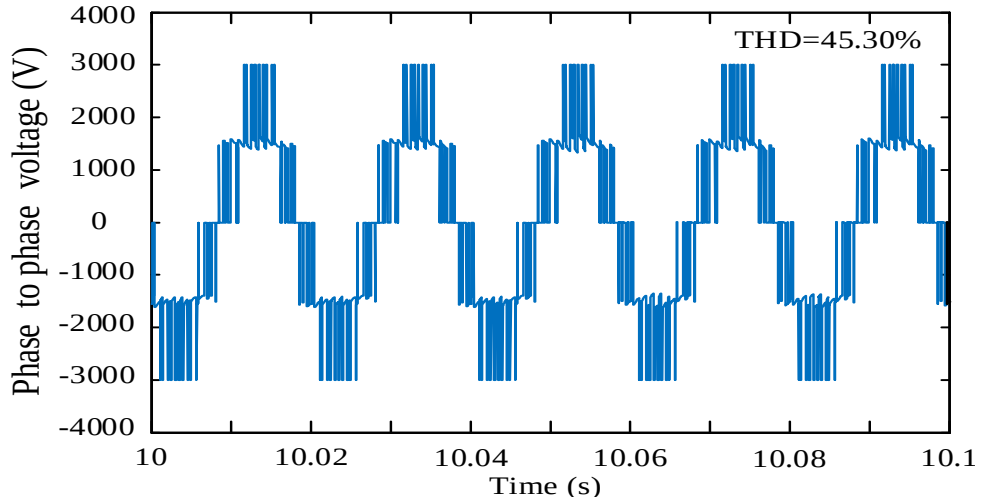

b. Voltage waveform of phase A to phase B voltage u_{AB}

Figure 6.16 Voltage waveforms of the conventional NPC in a load swell

Fig. 6.17 (a) and (b) show the waveform of the neutral-point voltage u_o, the phase A to phase B voltage u_{AB} of the proposed voltage compensated NPC inverter under the balanced and unbalanced working load conditions. With the voltage compensation device being added, the neutral-point voltage fluctuation of DC-link is suppressed effectively, being reduced to 40V. Similarly, an unbalanced load is applied at 10.05 s, lasting 0.05 s. The neutral-point voltage fluctuation of DC-link

is reduced to 75V under the unbalanced load condition. The THD of output voltage of the inverter is 42.24%.

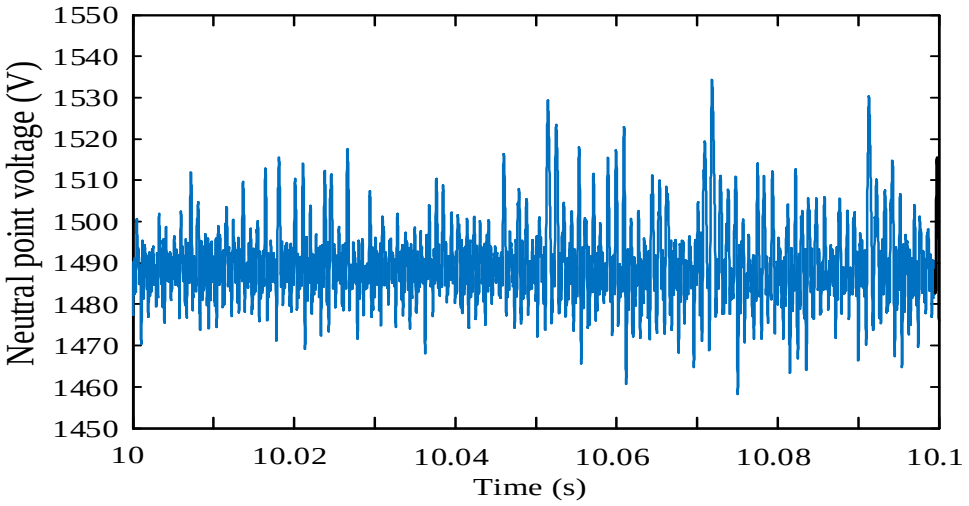

a. Voltage waveform of neutral-point voltage u_o

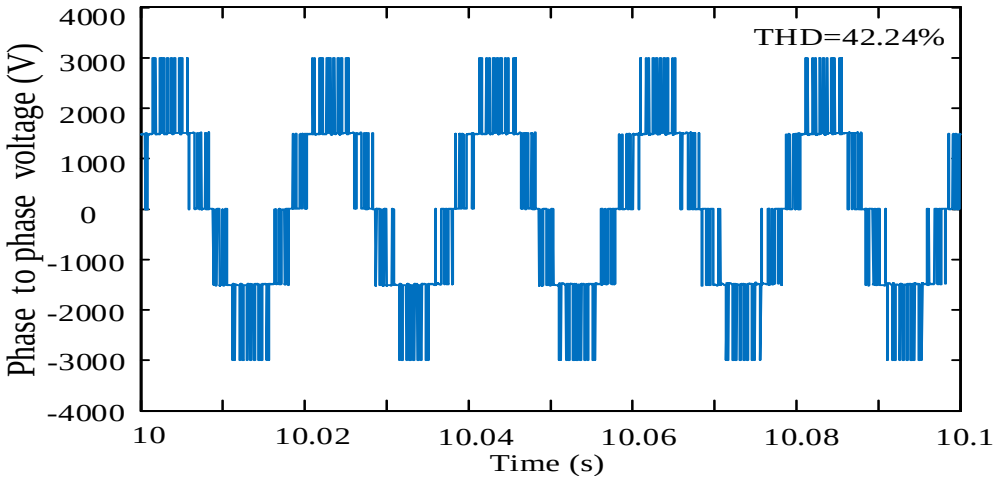

b. Voltage waveform of the phase A to phase B voltage u_{AB}

Figure 6.17 Voltage waveforms of the proposed VNPCI in a load swell

Fig. 6.18 (a) and (b) shows the neutral-point voltage u_o, the phase A to phase B voltage u_{AB} of the proposed current compensated NPC inverter under the balanced and unbalanced working load conditions. With the current compensation device

being added, the neutral-point voltage fluctuation of DC-link is suppressed further to 18V. Under the unbalanced load condition between 10.05 s and 10.1 s, the neutral-point voltage fluctuation of DC-link is reduced to 25V. The THD of output voltage of the NPC three-level inverter is 42.08%.

The results clearly show that the current compensated NPC inverter (CNPCI) has a better performance than the voltage compensated NPC inverter (VNPCI). Fig. 6.17 and Fig. 6.18 demonstrate that the CNPCI can restrict the neutral-point voltage fluctuation of the DC-link to 0.6% and 0.83%, respectively, when the CNPCI works under typical balanced and unbalanced working load conditions. However, the VNPCI restrains the neutral-point voltage fluctuation of DC-link to 1.2% and 2.3%, respectively, in the same conditions. The waveform comparison of neutral-point voltage u_o produced in different condition is shown in Fig. 6.19. The effect of the switching frequency on the output performance was also investigated. It was found a frequency higher than 2 kHz can produce acceptable results but the use of 10 kHz switching frequency produced the best results although it might be too fast for the device to work at such a high voltage level.

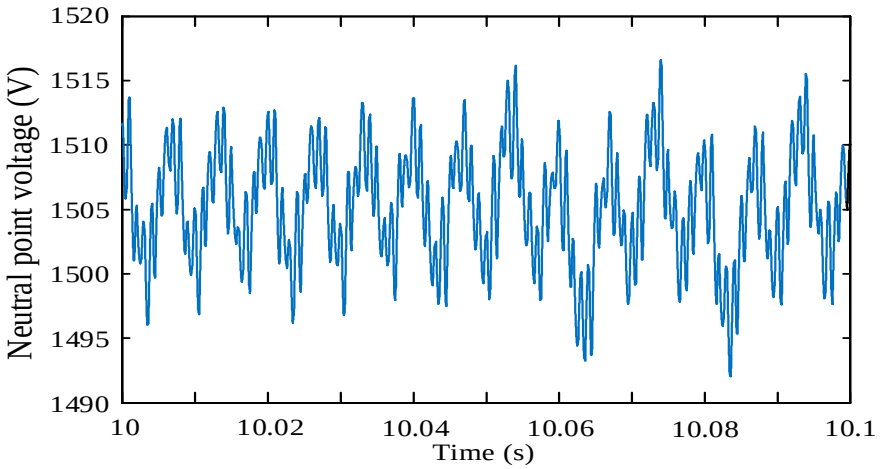

a. Voltage waveform of neutral-point voltage u_o

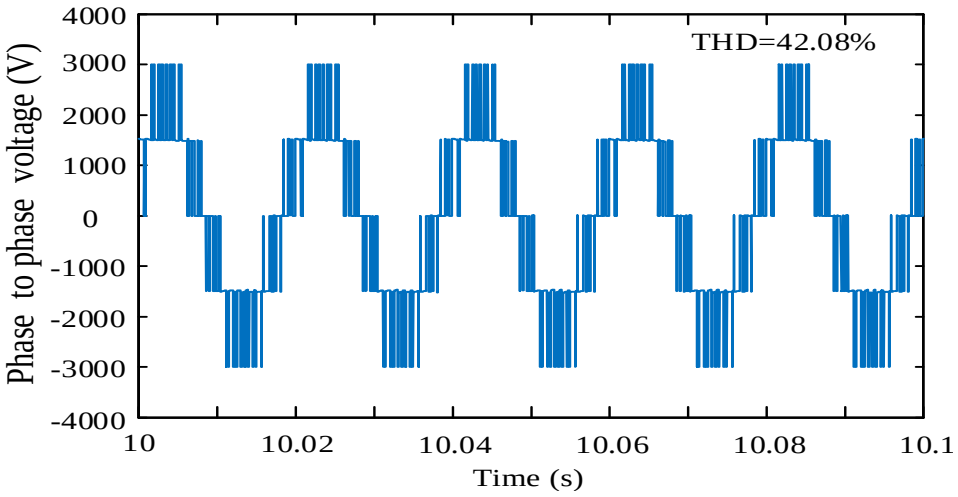

b. Voltage waveform of the phase A to phase B voltage u_{AB}

Figure 6.18 Voltage waveforms of the proposed CNPCI in a load swell

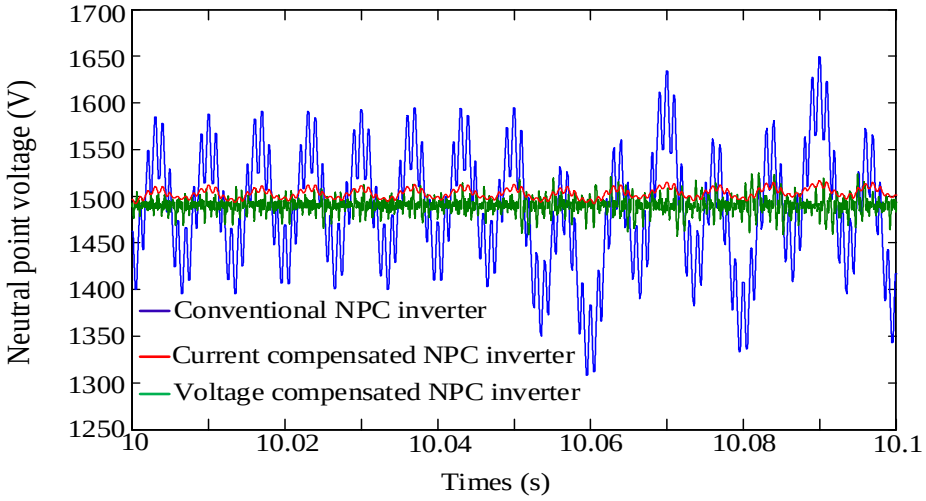

Figure 6.19 Waveform comparison of the neutral-point voltage u_o produced in the three inverter topologies

The VNPCI only eliminates the voltage fluctuation at the neutral-point of three-phase bridge arm; there is still fluctuation of the neutral-point voltage of the DC-link. This means the fluctuation problem cannot be eliminated thoroughly. However, the CNPCI can eliminate the neutral-point voltage fluctuation of the DC-link more effectively because the CNPCI offsets the current that flows between the neutral

point of the DC-link capacitors and the neutral point of the three-phase bridge circuit in the inverter, which is the cause of the voltage fluctuation. In addition, for the VNPCI, an isolated transformer is required, which should be able to handle several harmonic components without entering to the saturation region in the primary side and handle secondary side voltage range quickly to compensate the zero sequence voltage generated at the NPC converter. A complicated control scheme is therefore needed to overcome these problems [127]. On the contrary, the CNPCI avoids using the isolated transformer; the cost to manufacture and assemble the CNPCI is therefore lower than the VNPCI; the CNPCI requires only one IGBT power switching device (the most expensive component in the circuit), while the VNPCI needs four IGBT power switches and a coupling transformer. Thus, the CNPCI offers a more cost-effective performance.

The selection of PI control parameters were made by trial and error, aiming to achieve an optimal performance from tests. The proportional response can be adjusted by multiplying the error (i.e., the voltage difference in the case of the VNPCI and the current difference in the case of the CNPCI) by the proportional gain K_p. The integral term in the PI controller is the sum of the instantaneous error over time, thus giving the accumulated offset, which is then multiplied by the integral gain K_i. For the VNPCI, the selected value of K_p and K_i are 5 and 10, respectively, while, for the CNPCI, the selected value of K_p and K_i are 10 and 0.5, respectively. Results have shown that the use of these parameters can provide an improved performance of the controllers.

6.5.2 The shunt active power filters (SAPF)

The two proposed inverters are now applied in the SAPF that is indispensable part of the grid system. The SAPFs incorporating with the current compensated NPC inverter and the voltage compensated NPC inverter have been built and simulated. One of the typical SAPF applications is in the AC 400V DG system; but unlike the normal inverter, in order to satisfy the working condition in three phase power

system, the DC link voltage of SAPF must be over 3 times higher than the phase voltage. Thus, the NPC three-level inverter is very suitable to apply in SAPF due to high DC link voltage. The parameters used in the model are defined as follows: DC link voltage of SAPF is 800V; supply fundamental frequency f = 50Hz; filter line inductance Ls= 2mH; other parameters used for the inverters are referred to Table 6.1. It is noteworthy that the use of a low DC link voltage, rather than the 3000V previously discussed, was to assess the performance of the proposed inverters for this particular application in SAPF. As mentioned above, nonlinear loads are often connected in the power grid and the load condition will affect the work efficiency of the NPC three-level SAPF. The SAPF is firstly connected to a balanced nonlinear load and then to an unbalanced load emulated by a resistive (8Ω) and inductive (1.5mH) load being applied between phase A and phase B. The unbalanced load also occurs at 10.05 s and lasts 0.05 s.

Firstly, a SAPF based on the traditional NPC three-level inverter connected with the three phase nonlinear load, as shown in Fig. 6.2, has been investigated under the balanced and unbalanced working load conditions. Fig. 6.20 show the waveform and spectrogram of grid current of phase A, as an example. The grid current distorts heavily in both balanced and unbalanced load condition, and the THD of the grid current is 18.52%.

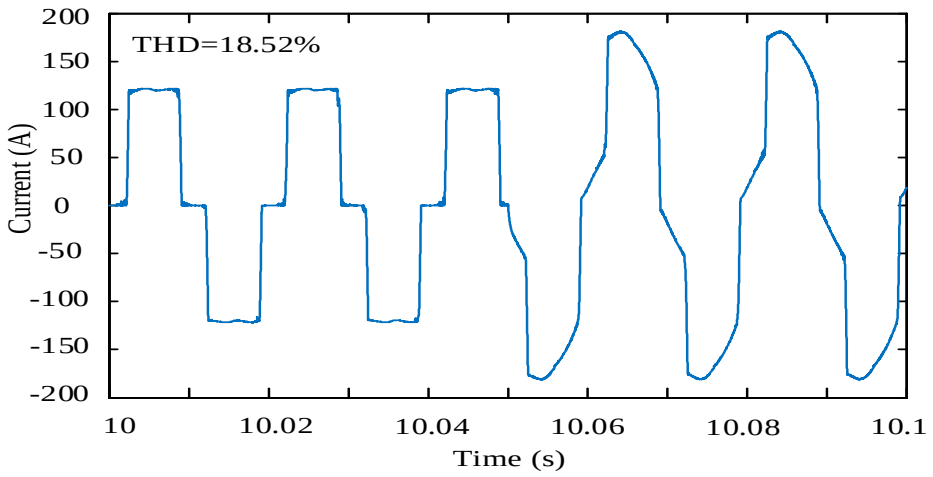

a. Waveform of phase-A current

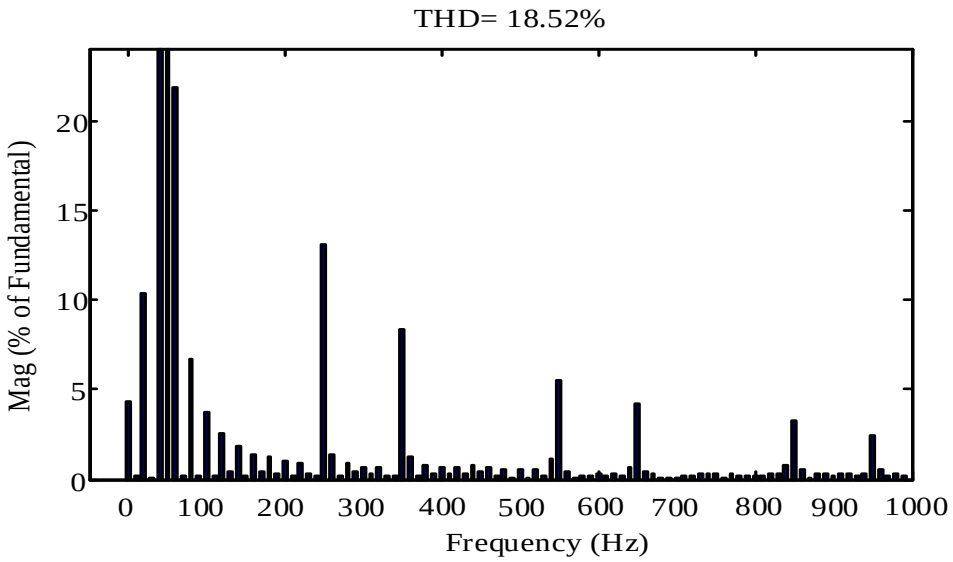

b. Spectrogram of phase-A current

Figure 6.20 Waveform and spectrogram of phase-A current of the power grid under the nonlinear load

Fig. 6.21 shows the waveform and spectrogram of the filter output of phase A, i.e., the currents i_{ca}, i_{cb} and i_{cc} as shown in Fig. 6.2, and the grid currents of the proposed VNPCI three-level SAPF, i.e., the currents i_{sa}, i_{sb} and i_{sc} as shown in Fig. 6.2, under the typical balanced and unbalanced working load conditions. Essentially, the filter output currents are effective to compensate the harmonics being injected from nonlinear loads, hence improving the quality of the gird currents. The frequency component is dominant at 50 Hz while other harmonic components in phase-A current are now eliminated effectively. The THD of the grid current is reduced to 2.05%. Fig. 6.22 shows the waveform and spectrogram of the grid currents of the proposed CNPCI three-level SAPF under typical balanced and unbalanced working load conditions. It can be seen that the harmonic currents in phase A can be eliminated more effectively. The THD of the grid current is reduced further to 1.7%.

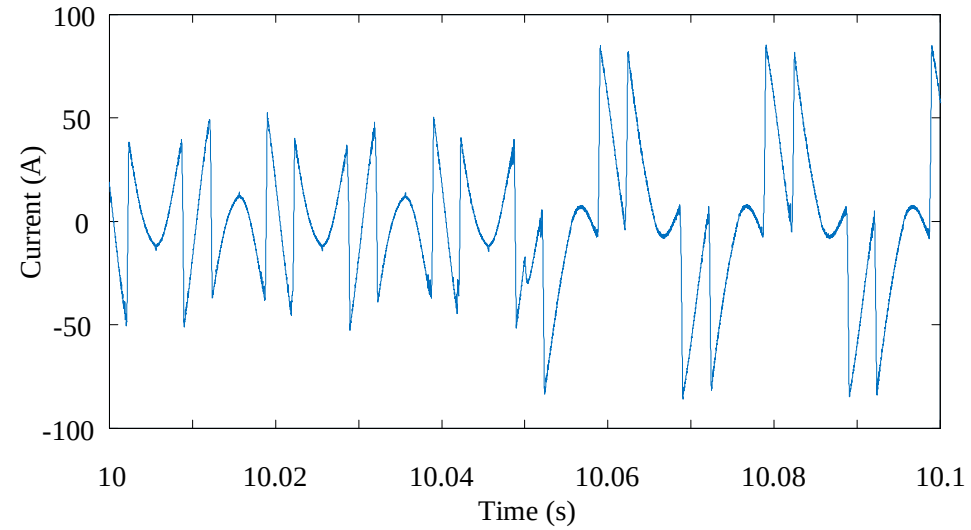

a. Waveform of the phase-A current in the filter output

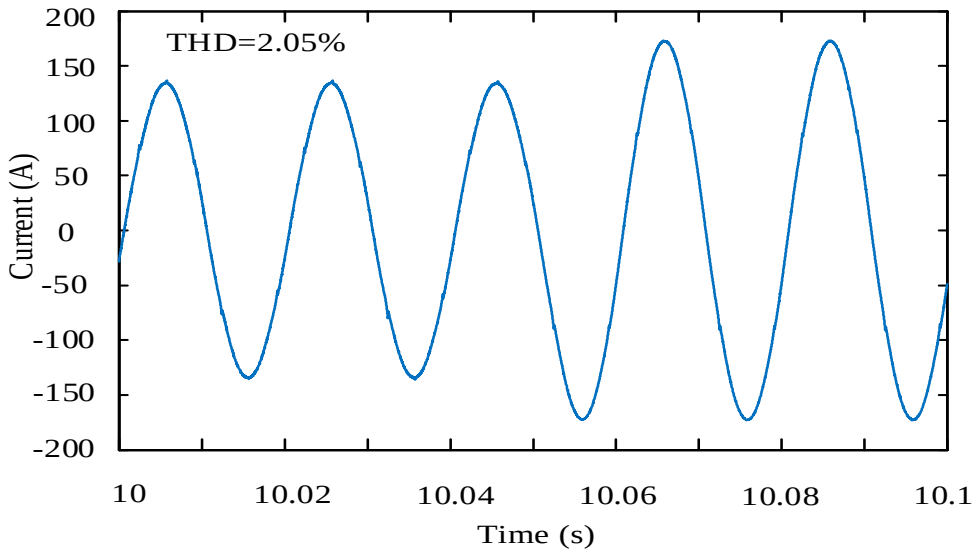

b. Waveform of the phase-A current in the power grid

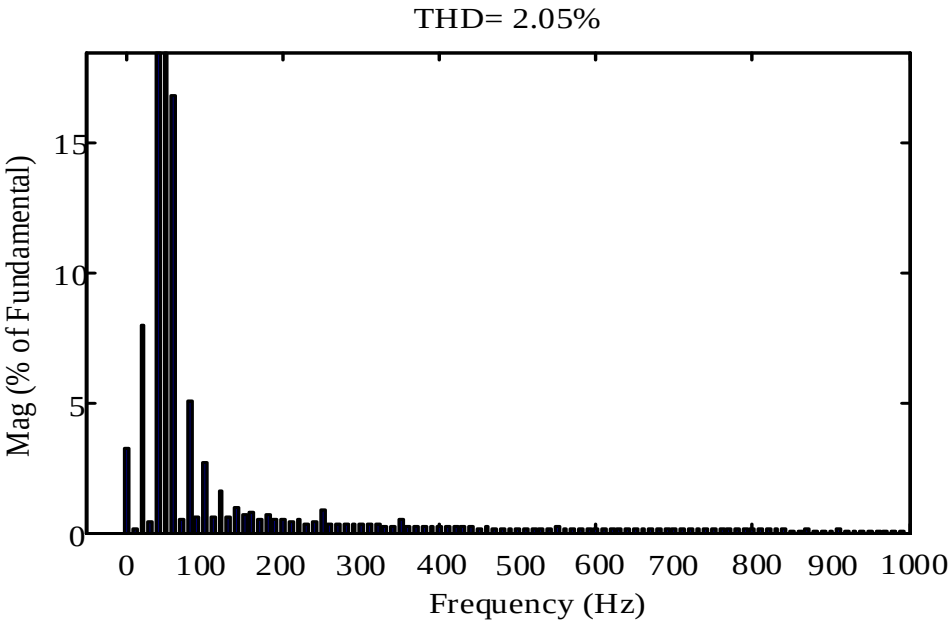

c. Spectrogram of phase-A current

Figure 6.21 Waveform and spectrogram of the phase-A currents in the filter output and the power grid employing the proposed VNPCI three-level SAPF

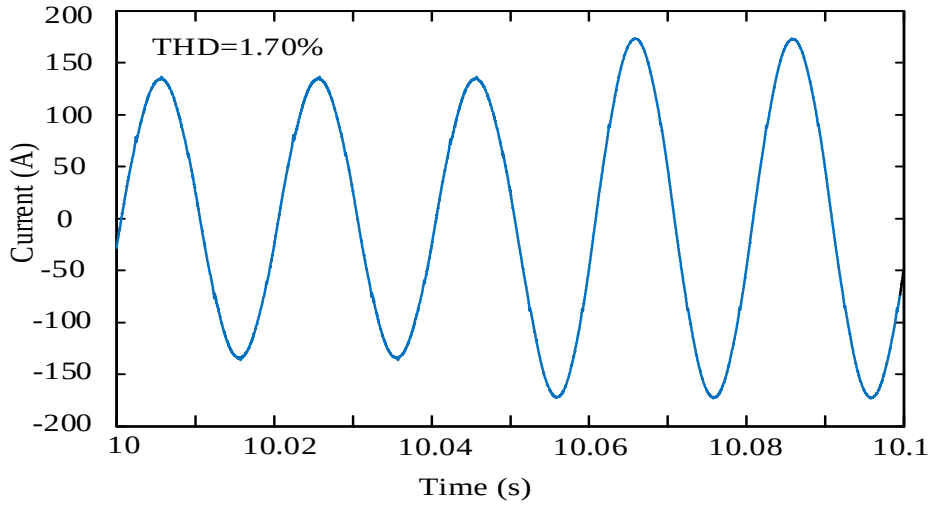

a. Waveform of phase-A current

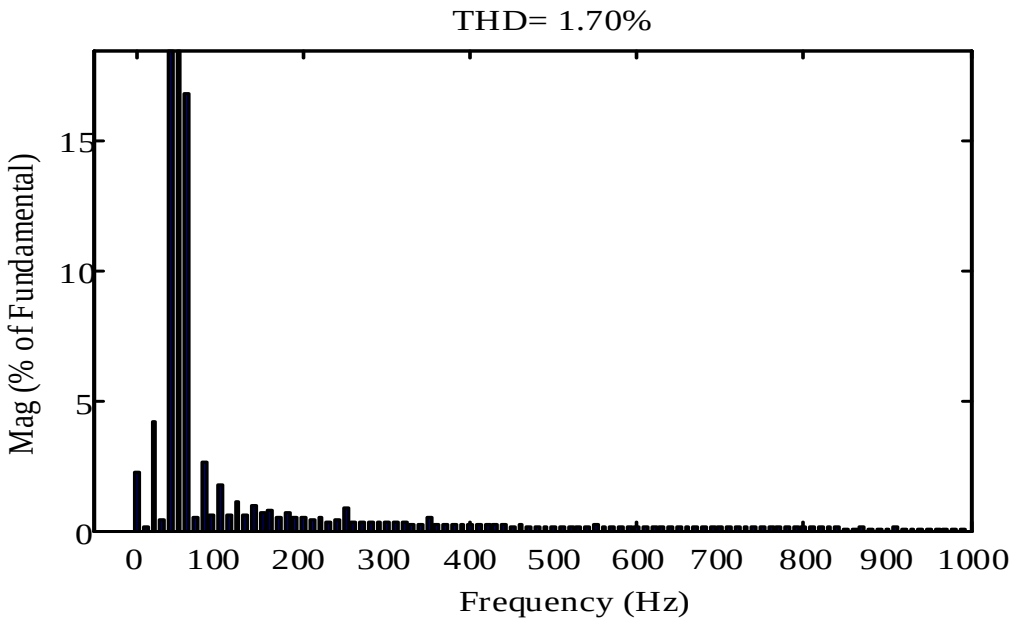

b. Spectrogram of phase-A current

Figure 6.22. Waveform and spectrogram of the power grid currents employing the proposed CNPCI three-level SAPF

6.6 Summary and discussion

The chapter has presented two new NPC three-level inverter topologies in order to eliminate excessive voltage fluctuation at the neutral-point of DC-link capacitors in the inverter. The first is voltage dependent, which adopts a voltage compensation method to restrain the neutral point voltage fluctuation. The second is current dependent, using a current compensation method to restrict the voltage fluctuation. The results have shown that both topologies can suppress the neutral-point voltage fluctuation of the DC-link effectively under typical balanced and unbalanced working load conditions. The current compensated NPC inverter outperforms the voltage compensated NPC inverter. Furthermore, these compensated NPC three-level inverters are applied to a shunt active power filter in the grid lines. It is shown that the proposed approaches are effective and feasible for eliminating harmonic currents and therefore improving power quality of the grid system when connected with nonlinear loads. The THD of the grid current is reduced from 18.52% to 2.05%.

Future work will focus on experimental testing of the proposed NPC three-level SAPFs to further verify their performance. Optimal selection of PI control parameters for the inverters will also be investigated in order to further optimize system performance under different load conditions. In addition, the application of the proposed current compensated NPC inverter is being considered in both a wind power generation system and a small grid system in the laboratory in order to address the power quality issues related to inverter-coupled generation and associated loads.

Chapter7. Conclusion and discussion

This chapter summarises the achievements of the research and explains how the objectives stated in Section 1.3 are achieved by the researcher. Thereafter, the academic contributions obtained from the research are illustrated. Finally, the conclusion of the research work during the PhD period and the future works are presented.

7.1 Overview of the research objectives and achievements

The development of the wind farm has grown dramatically in worldwide over the past 20 years. In order to satisfy the reliability requirement of the power grid, the wind farm should generate sufficient active power to make the frequency stable. Consequently, there are many methods that have been proposed to achieve optimizing wind farm active power dispatch strategy. In previous research, it assumed that each wind turbine has the same health condition in the wind farm, hence the power dispatch for healthy and sub-healthy wind turbines are treated equally. It will accelerate the sub-healthy wind turbines damage, which may leads to decrease generating efficiency and increases operating cost of the wind farm. In this thesis, a study has been carried out into optimizing wind farm power output control based on estimating health condition of wind turbines. The main achievements of this research, which are associated with the original objectives given in Section 1.3, are as follows:

Objective 1: To conduct a systematic literature review of background information of wind power technology, previous research works concerning to condition monitoring algorithms and techniques applied in wind turbines, and optimizing power dispatch strategy of the wind farm.

Achievement 1: An overview of the background information of wind power technology are achieved in section 2.1 and 2.2; the model of a typical DFIG system is illustrated in section 3.2. The wind turbine model includes aerodynamics model, drive train model, generator model and pitch model; the literature review of the condition monitoring algorithms is illustrated in section 2.3， where it can be categorized into statistical condition monitoring system and model based condition monitoring system. There are many types of signals can be used in condition monitoring systems, including current, voltage, temperature, strain, vibration, oil pressure, acoustic emission and torque.

Objective 2: To study the SCADA data obtained from a commercial operational wind farm for future research.

Achievement 2: The SCADA data obtained from a commercial operational wind farm is analyzed to gain the fault feature. The SCADA data used, in this study case, contains 128 types of parameters, which comprises temperatures, pressures, vibrations, power outputs, wind speed, and digital control signals. Note that SCADA signals are usually processed and stored at 10 minute intervals, although sampled in the order of 2 s

Objective 3: To propose appropriate model based algorithm to detect the faults of wind turbines effectively.

Achievement 3: The ELM algorithm is adopted to establish the prediction model of condition monitoring system. In order to solve the arbitrary values assignment problem, the weights of the inputs and the biases of the hidden neurons of the ELM model are optimized by the genetic algorithm (GA) in section 4.3. Furthermore, a kind of improved online ELM algorithm is also applied to model-based condition monitoring system. Models have been validated from supervisory control and data acquisition (SCADA) data acquired from an operational wind farm, which contains various types of temperature and pressure data of the gearbox. The results show that the proposed method can more efficiently detect faults in section 4.5

Objective 4: To establish health condition estimation method to assess the health condition of the whole wind turbine system.

Achievement 4: The health condition of the wind turbine is consisted of two parts：
one is the fault degree level estimation, the other one is the health condition estimation based on fault degree level estimation. Bonferroni interval is selected to achieve fault degree estimation of wind turbines, while analytic hierarchy process (AHP) is used to estimate health condition level by considered the maintenance time and cost determine the effective operating time and economic benefit of wind turbines.

Objective 5: To design an optimizing wind farm power output control strategy based on estimating health condition of wind turbines.

Achievement 5: A novel wind farm active power dispatch strategy considering the health condition of wind turbines is the proposed in section 5.4. Essentially, the aim of the proposed method is to make the healthy wind turbines generate power as much as possible and reduce fatigue loads on the sub-healthy wind turbines. Compared with previous methods, the proposed methods is able to dramatically reduce the fatigue loads on sub-healthy wind turbines under the condition of satisfying network operator active power demand.

Objective 6: To adopt SAPF to enhance the reliability and output power quality of the wind farm

Achievement 6: In chapter 6, a novel NPC three-level SAPF is proposed. The result shows that the proposed approaches are effective and feasible for eliminating harmonic currents and therefore improving power quality of the grid system when connected with nonlinear loads. It means that adopting SAPF is able to enhance the reliability and output power quality of the wind farm.

Objective 7: To validate and analyze the proposed methods and algorithms by using SCADA data and simulation data.

Achievement 7: The SCADA data obtained from the commercial wind farm and mathematical simulation model are used to validate proposed methods in section 4.5, section 5.5 and section 6.5.

7.2 Knowledge contributions arising from the research

Contribution 1: In this study, a data-based approach using an extreme learning machine (ELM) algorithm optimized with a genetic algorithm has been proposed for condition monitoring of the gearbox in wind turbines. Compared with traditional BP-ANN algorithm, the ELM learning algorithm can provide a good fit with a considerably reduced learning time.

Contribution 2: Wind turbines are the complicate system that generally have several subsystems, and each subsystem also has many components. Thus, multivariable analysis taking account to interaction between different kinds of variables is more valuable yet. The Mahalanobis distance (MD) is a minimum-redundancy maximum-relevance feature approach, taking into account interactions between signals measured from different components in the gearbox without consideration of the units used for the measurement. This means that the MD measure has the capability to describe correlations among variables in a process or a system. Thus, the MD measure can provide a univariate distance value for multivariate data, which is ideal for estimating the deviation values of a complex system

Contribution 3: A physical kinetic energy correction model is proposed in this thesis. Traditionally, the same threshold is applied to temperature monitoring regardless of the operating power, which means the same weight is assigned for the temperature change in terms of its contribution to the damage of gearbox. However, the operating power could have a significant impact on the temperature changes; therefore, its effect on the temperature changes should be weighted differently.

Contribution 4: In order to obtain the fault degree of the components of the wind turbine, Bonferroni interval method can provide confidence intervals to estimate deviation level of each component by providing details concerning the effect of individual components on the overall operational conditions. Then, the health condition estimation method based on AHP is used to sort health condition level by accounting for multi- criterion factors, including fault degree, maintenance cost and maintenance time.

Contribution 5: In previous research, it assumed that each wind turbine has the same health condition in the wind farm, hence the power dispatch for healthy and sub-healthy wind turbines are treated equally. It will accelerate the sub-healthy wind turbines damage, which may leads to decrease generating efficiency and increases operating cost of the wind farm. Thus, a novel wind farm active power dispatch strategy considering the health condition of wind turbines is the proposed. The results have shown that the proposed method can significantly reduce fatigue loads

on sub-healthy wind turbines under satisfying wind farm total power output condition, which is beneficial to prolong life-span and economic benefit of wind turbines.

Contribution 6: A new method for improving the performance of SAPFs using neutral point clamped (NPC) three-level inverter is adopted to improve power quality of the grid by mitigating harmonics injected from nonlinear loads. The results have shown that both topologies can suppress the neutral-point voltage fluctuation of the DC-link effectively under typical balanced and unbalanced working load conditions, which is beneficial to the proposed SAPF to improve power quality of the grid system when connected with nonlinear loads.

7.3 Future work for improvement

The limitations of the proposed techniques and recommendations concerning future work that could potentially improve the optimizing wind farm power output control based on estimating health condition of wind turbines.

1. In chapter 4, the data used in this paper are mostly representative of the normal operation of wind turbines and do not contain a great deal of information regarding the occurrence of faults; consequently, this paper employs static ELM models only. Future work will therefore consider dynamic models by taking into account the effect of more past inputs on the model output, and the different effect each component has on the health condition of the gearbox.

2. In chapter 4, the main purpose of using OS-ELM is to achieve training data being updated to ensure that the model is adapted to accommodate different operational behaviours of the wind turbines encountered during their operations. Real time online training capacity of the method is not considered in the thesis. However, this OS-ELM algorithm has the ability of achieving the online training in real time, if the sampling speed for updated training data is quick enough.

3. In chapter 5, the optimized power dispatch strategy considering the health condition of the wind turbine adopts the simple proportion distribution to dispatch reference power to each wind turbine. However, effects of different power generation strategies on wind turbine structural loads are different. Compared with baseline mode, de-rated and percentage mode can decrease the fatigue loads on sub-healthy wind turbines by limiting maximum power output. Percentage mode has better performance on reducing the torque loads on drivetrain system than de-rated mode at same active power output level. However, percentage mode also has higher the fatigue loads on blade system than de-rated mode due to increasing rotate speed of the rotor. High rotate speed of the rotor will increase the loads on blade system. It means that de-rated mode is more suitable to reduce loads on blade system, while percentage mode is more beneficial to decrease the torque loads on drivetrain system. So it is desirable to adopt an optimized control mode selection method in wind turbine control system for wind farm control, taking into account effects of power reserve control on wind turbine structural loading, to further optimize load reduction on sub-healthy component.

4. In chapter 6, the research is only focus on simulation analysis. Future work will focus on experimental testing of the proposed NPC three-level SAPFs to further verify their performance. Optimal selection of PI control parameters for the inverters will also be investigated in order to further optimize system performance under different load conditions. In addition, the application of the proposed current compensated NPC inverter is being considered in both a wind power generation system and a small grid system in the laboratory in order to address the power quality issues related to inverter-coupled generation and associated loads.

Reference

[1] H. Bevrani, A. Ghosh, and G. Ledwich, "Renewable energy sources and frequency regulation: survey and new perspectives," *IET Renewable Power Generation*, vol. 4, p. 438, 2010.

[2] W. Weisheng, C. Yongning, W. Zhen, L. Yan, W. Ruiming, N. Miller, *et al.*, "On the Road to Wind Power: China's Experience at Managing Disturbances with High Penetrations of Wind Generation," *IEEE Power and Energy Magazine*, vol. 14, pp. 24-34, 2016.

[3] L. Jiang, Y. Chi, H. Qin, Z. Pei, Q. Li, M. Liu, *et al.*, "Wind Energy in China," *IEEE Power and Energy Magazine*, vol. 9, pp. 36-46, 2011.

[4] X. Yang, Y. Song, G. Wang, and W. Wang, "A Comprehensive Review on the Development of Sustainable Energy Strategy and Implementation in China," *IEEE Transactions on Sustainable Energy*, vol. 1, pp. 57-65, 2010.

[5] A. Walford, "Wind Turbine Reliability: understanding and minimizing wind turbine operation and maintenance costs," Sandia National Laboratories2006.

[6] W. Zhang and X. Ma, "Simultaneous Fault Detection and Sensor Selection for Condition Monitoring of Wind Turbines," *Energies*, vol. 9, p. 280, 2016.

[7] W. Yang, P. J. Tavner, and W. Tian, "Wind Turbine Condition Monitoring Based on an Improved Spline-Kernelled Chirplet Transform," *IEEE Transactions on Industrial Electronics*, vol. 62, pp. 6565-6574, 2015.

[8] P. Guo and D. Infield, "Wind Turbine Tower Vibration Modeling and Monitoring by the Nonlinear State Estimation Technique (NSET)," *Energies*, vol. 5, pp. 5279-5293, 2012.

[9] Y. Wenxian, P. J. Tavner, C. J. Crabtree, and M. Wilkinson, "Cost-Effective Condition Monitoring for Wind Turbines," *IEEE Transactions on Industrial Electronics*, vol. 57, pp. 263-271, 2010.

[10] R. J. de Andrade Vieira and M. A. Sanz-Bobi, "Failure Risk Indicators for a Maintenance Model Based on Observable Life of Industrial Components With an Application to Wind Turbines," *IEEE Transactions on Reliability*, vol. 62, pp. 569-582, 2013.

[11] E. S áz-Mar ń, E. Lobato, I. Egido, and L. Rouco, "Economic assessment of voltage and reactive power control provision by wind farms," *Wind Energy*, vol. 18, pp. 851-864, 2015.

[12] Z. Lubosny and J. W. Bialek, "Supervisory Control of a Wind Farm," *IEEE Transactions on Power Systems*, vol. 22, pp. 985-994, 2007.

[13] M. Tsili and S. Papathanassiou, "A review of grid code technical requirements for wind farms," *IET Renewable Power Generation*, vol. 3, p. 308, 2009.

[14] P. Cross and X. Ma, "Nonlinear system identification for model-based condition monitoring of wind turbines," *Renewable Energy,* vol. 71, pp. 166-175, 2014.
[15] W. Qiao and D. Lu, "A Survey on Wind Turbine Condition Monitoring and Fault Diagnosis;Part I: Components and Subsystems," *IEEE Transactions on Industrial Electronics,* vol. 62, pp. 6536-6545, 2015.
[16] W. Qiao and D. Lu, "A Survey on Wind Turbine Condition Monitoring and Fault Diagnosis;Part II: Signals and Signal Processing Methods," *IEEE Transactions on Industrial Electronics,* vol. 62, pp. 6546-6557, 2015.
[17] X. Sun, J. Zeng, and Z. Chen, "Site Selection Strategy of Single-Frequency Tuned R-APF for Background Harmonic Voltage Damping in Power Systems," *IEEE Transactions on Power Electronics,* vol. 28, pp. 135-143, 2013.
[18] J. He, B. Liang, Y. W. Li, and C. Wang, "Simultaneous Microgrid Voltage and Current Harmonics Compensation Using Coordinated Control of Dual-Interfacing Converters," *IEEE Transactions on Power Electronics,* vol. 32, pp. 2647-2660, 2017.
[19] J. Chen, X. Zhang, and C. Wen, "Harmonics Attenuation and Power Factor Correction of a More Electric Aircraft Power Grid Using Active Power Filter," *IEEE Transactions on Industrial Electronics,* vol. 63, pp. 7310-7319, 2016.
[20] C. Zhong, L. Yingpeng, and C. Miao, "Control and Performance of a Cascaded Shunt Active Power Filter for Aircraft Electric Power System," *IEEE Transactions on Industrial Electronics,* vol. 59, pp. 3614-3623, 2012.
[21] J. Fang, G. Xiao, X. Yang, and Y. Tang, "Parameter Design of a Novel Series-Parallel-Resonant <italic>LCL</italic> Filter for Single-Phase Half-Bridge Active Power Filters," *IEEE Transactions on Power Electronics,* vol. 32, pp. 200-217, 2017.
[22] P. Kanjiya, V. Khadkikar, and H. H. Zeineldin, "Optimal Control of Shunt Active Power Filter to Meet IEEE Std. 519 Current Harmonic Constraints Under Nonideal Supply Condition," *IEEE Transactions on Industrial Electronics,* vol. 62, pp. 724-734, 2015.
[23] M. Qasim, P. Kanjiya, and V. Khadkikar, "Optimal Current Harmonic Extractor Based on Unified ADALINEs for Shunt Active Power Filters," *IEEE Transactions on Power Electronics,* vol. 29, pp. 6383-6393, 2014.
[24] H.-S. Kim, Y.-C. Kwon, S.-J. Chee, and S.-K. Sul, "Analysis and Compensation of Inverter Nonlinearity for Three-Level T-Type Inverters," *IEEE Transactions on Power Electronics,* vol. 32, pp. 4970-4980, 2017.
[25] P. Sørensen, A. D, F. Iov, F. Blaabjerg, and M. H. Donovan, "Wind farm models and control strategies," Risø National LaboratoryAugust 2005.
[26] P. Guo and N. Bai, "Wind Turbine Gearbox Condition Monitoring with AAKR and Moving Window Statistic Methods," *Energies,* vol. 4, pp. 2077-2093, 2011.

[27] A. Rolan, F. Corcoles Lopez, S. Bogarra, L. Monjo, and J. Pedra, "Reduced-Order Models of Squirrel-Cage Induction Generators for Fixed-Speed Wind Turbines Under Unbalanced Grid Conditions," *IEEE Transactions on Energy Conversion,* vol. 31, pp. 566-577, 2016.
[28] M. H. Marzebali, S. H. Kia, H. Henao, G.-A. Capolino, and J. Faiz, "Planetary Gearbox Torsional Vibration Effects on Wound-Rotor Induction Generator Electrical Signatures," *IEEE Transactions on Industry Applications,* vol. 52, pp. 4770-4780, 2016.
[29] X. Zhang, Y. Wang, Y. Fu, and L. Xu, "A novel method for obtaining virtual inertial response of DFIG-based wind turbines," *Wind Energy,* vol. 19, pp. 313-328, 2016.
[30] R. Sarrias-Mena, L. M. Fernández-Ramírez, C. A. García-Vázquez, and F. Jurado, "Dynamic evaluation of two configurations for a hybrid DFIG-based wind turbine integrating battery energy storage system," *Wind Energy,* vol. 18, pp. 1561-1577, 2015.
[31] M. Curzi, R. Sharma, and F. Martin, "In fault ride through reactive current rise time requirements of various European grid codes-analysis based on a full-converter wind turbine," *Wind Energy,* vol. 19, pp. 1121-1133, 2016.
[32] Y. Qiu, W. Zhang, D. Infield, Y. Feng, and J. Sun, "Applying thermophysics for wind turbine drivetrain fault diagnosis using SCADA data," *IET Renewable Power Generation,* vol. 10, pp. 661-668, 2016.
[33] C. Kaidis, B. Uzunoglu, and F. Amoiralis, "Wind turbine reliability estimation for different assemblies and failure severity categories," *IET Renewable Power Generation,* vol. 9, pp. 892-899, 2015.
[34] H. Zhao, Q. Wu, Q. Guo, H. Sun, and Y. Xue, "Distributed Model Predictive Control of a Wind Farm for Optimal Active Power ControlPart I: Clustering-Based Wind Turbine Model Linearization," *IEEE Transactions on Sustainable Energy,* vol. 6, pp. 831-839, 2015.
[35] R. Bi, "Interpretation to Wind Turbine Generator Faults and an Improved Condition Monitoring Technique Based on Normal Behaviour Models for Wind Turbine Generator Systems," Doctor of Philosophy, School of Engineering and Built Environment, Glasgow Caledonian University, Glasgow, 2016.
[36] D. Pattison, M. Segovia Garcia, W. Xie, F. Quail, M. Revie, R. I. Whitfield, *et al.*, "Intelligent integrated maintenance for wind power generation," *Wind Energy,* vol. 19, pp. 547-562, 2016.
[37] C. Tibaldi, L. C. Henriksen, M. H. Hansen, and C. Bak, "Wind turbine fatigue damage evaluation based on a linear model and a spectral method," *Wind Energy,* vol. 19, pp. 1289-1306, 2016.
[38] D. G. Giaourakis and A. N. Safacas, "Quantitative and qualitative behavior analysis of a DFIG wind energy conversion system by a wind gust and converter faults," *Wind Energy,* vol. 19, pp. 527-546, 2016.
[39] X. Gong and W. Qiao, "Current-Based Mechanical Fault Detection for Direct-Drive Wind Turbines via Synchronous Sampling and Impulse Detection," *IEEE Transactions on Industrial Electronics,* vol. 62, pp. 1693-1702, 2015.

[40] X. An, D. Jiang, S. Li, and M. Zhao, "Application of the ensemble empirical mode decomposition and Hilbert transform to pedestal looseness study of direct-drive wind turbine," *Energy,* vol. 36, pp. 5508-5520, 2011.
[41] T. Barszcz and R. B. Randall, "Application of spectral kurtosis for detection of a tooth crack in the planetary gear of a wind turbine," *Mechanical Systems and Signal Processing,* vol. 23, pp. 1352-1365, 2009.
[42] S. J. Watson, B. J. Xiang, W. Yang, P. J. Tavner, and C. J. Crabtree, "Condition Monitoring of the Power Output of Wind Turbine Generators Using Wavelets," *IEEE Transactions on Energy Conversion,* vol. 25, pp. 715-721, 2010.
[43] C. S. Tsai, C. T. Hsieh, and S. J. Huang, "Enhancement of Damage-Detection of Wind Turbine Blades Via CWT-Based Approaches," *IEEE Transactions on Energy Conversion,* vol. 21, pp. 776-781, 2006.
[44] F. P. Garc á M árquez, A. M. Tobias, J. M. Pinar P érez, and M. Papaelias, "Condition monitoring of wind turbines: Techniques and methods," *Renewable Energy,* vol. 46, pp. 169-178, 2012.
[45] C. S. Gray and S. J. Watson, "Physics of Failure approach to wind turbine condition based maintenance," *Wind Energy,* vol. 13, pp. 395-405, 2009.
[46] Shulian Yang, Wenhai Li , and C. Wang, "The Intelligent Fault diagnosis of Wind Turbine Gearbox Based on Artificial Neural Network," presented at the International Conference on Condition Monitoring and Diagnosis, Beijing, China, 2008.
[47] Jianwu Zeng, Dingguo Lu, Yue Zhao, Zhe Zhang, S Wei Qiao*, and XiangGong, "Wind Turbine Fault Detection and Isolation Using Support Vector Machine and a Residual-Based Metho," presented at the American Control Conference (ACC)

Washington, DC, USA, 2013.
[48] H. Li, Y. G. Hu, C. Yang, Z. Chen, H. T. Ji, and B. Zhao, "An improved fuzzy synthetic condition assessment of a wind turbine generator system," *International Journal of Electrical Power & Energy Systems,* vol. 45, pp. 468-476, 2013.
[49] X. Chen, Z. Y. Dong, K. Meng, Y. Xu, K. P. Wong, and H. W. Ngan, "Electricity Price Forecasting With Extreme Learning Machine and Bootstrapping," *IEEE Transactions on Power Systems,* vol. 27, pp. 2055-2062, 2012.
[50] X. Lu, C. Liu, and M. Huang, "Online Probabilistic Extreme Learning Machine for Distribution Modeling of Complex Batch Forging Processes," *IEEE Transactions on Industrial Informatics,* vol. 11, pp. 1277-1286, 2015.
[51] R. Zhang, Y. Lan, G. B. Huang, Z. B. Xu, and Y. C. Soh, "Dynamic extreme learning machine and its approximation capability," *IEEE Trans Cybern,* vol. 43, pp. 2054-65, Dec 2013.
[52] B. Tang, T. Song, F. Li, and L. Deng, "Fault diagnosis for a wind turbine transmission system based on manifold learning and Shannon wavelet support vector machine," *Renewable Energy,* vol. 62, pp. 1-9, 2014.

[53] y. li, Z. Xu, and K. Meng, "Optimal Power Sharing Control of Wind Turbines," *IEEE Transactions on Power Systems,* pp. 1-1, 2016.
[54] H. Zhao, Q. Wu, Q. Guo, H. Sun, and Y. Xue, "Distributed Model Predictive Control of a Wind Farm for Optimal Active Power ControlPart II: Implementation With Clustering-Based Piece-Wise Affine Wind Turbine Model," *IEEE Transactions on Sustainable Energy,* vol. 6, pp. 840-849, 2015.
[55] P. Sørensen, A. D. Hansen, F. Iov, F. Blaabjerg, and M. H. Donovan, "Wind turbine power references in coordinated control of wind farms," 2005.
[56] P. Hou, B. Zhang, M. Soltani, Z. Chen, C. Chen, and W. Hu, "Optimised power dispatch strategy for offshore wind farms," *IET Renewable Power Generation,* vol. 10, pp. 399-409, 2016.
[57] Y. Tan, L. Meegahapola, and K. M. Muttaqi, "A Suboptimal Power-Point-Tracking-Based Primary Frequency Response Strategy for DFIGs in Hybrid Remote Area Power Supply Systems," *IEEE Transactions on Energy Conversion,* vol. 31, pp. 93-105, 2016.
[58] G. Zonghe, G. Jian, Z. Kaifeng, D. Zemei, B. Xingzhong, P. Mingqiao, *et al.*, "Wind Power Dispatch Supporting Technologies and Its Implementation," *IEEE Transactions on Smart Grid,* vol. 4, pp. 1684-1691, 2013.
[59] K. T. Magar, M. J. Balas, and S. A. Frost, "Direct adaptive torque control for maximizing the power captured by wind turbine in partial loading condition," *Wind Energy,* vol. 19, pp. 911-922, 2016.
[60] M. Martini, R. Guanche, J. A. Armesto, I. J. Losada, and C. Vidal, "Met-ocean conditions influence on floating offshore wind farms power production," *Wind Energy,* vol. 19, pp. 399-420, 2016.
[61] H. Long, L. Wang, Z. Zhang, Z. Song, and J. Xu, "Data-Driven Wind Turbine Power Generation Performance Monitoring," *IEEE Transactions on Industrial Electronics,* vol. 62, pp. 6627-6635, 2015.
[62] S. Gill, B. Stephen, and S. Galloway, "Wind Turbine Condition Assessment Through Power Curve Copula Modeling," *IEEE Transactions on Sustainable Energy,* vol. 3, pp. 94-101, 2012.
[63] K. De Vos, J. Morbee, J. Driesen, and R. Belmans, "Impact of wind power on sizing and allocation of reserve requirements," *IET Renewable Power Generation,* vol. 7, pp. 1-9, 2013.
[64] C.-T. Li, H. Peng, and J. Sun, "Predictive control and sizing of energy storage to mitigate wind power intermittency," *Wind Energy,* vol. 19, pp. 437-451, 2016.
[65] T. Knudsen, T. Bak, and M. Svenstrup, "Survey of wind farm control—power and fatigue optimization," *Wind Energy,* vol. 18, pp. 1333–1351, 2015.
[66] P. A. Fleming, J. Aho, A. Buckspan, E. Ela, Y. Zhang, V. Gevorgian, *et al.*, "Effects of power reserve control on wind turbine structural loading," *Wind Energy,* vol. 19, pp. 453-469, 2016.

[67] M.-H. Wang, S. Yan, S.-C. Tan, and S. Y. R. Hui, "Hybrid-DC Electric Springs for DC Voltage Regulation and Harmonic Cancellation in DC Microgrids," *IEEE Transactions on Power Electronics,* vol. 33, pp. 1167-1177, 2018.
[68] F. Blaabjerg, R. Teodorescu, M. Liserre, and A. V. Timbus, "Overview of Control and Grid Synchronization for Distributed Power Generation Systems," *IEEE Transactions on Industrial Electronics,* vol. 53, pp. 1398-1409, 2006.
[69] A. Lewicki, Z. Krzeminski, and H. Abu-Rub, "Space-Vector Pulsewidth Modulation for Three-Level NPC Converter With the Neutral Point Voltage Control," *IEEE Transactions on Industrial Electronics,* vol. 58, pp. 5076-5086, 2011.
[70] T. Ghennam, E. M. Berkouk, and B. Francois, "A Novel Space-Vector Current Control Based on Circular Hysteresis Areas of a Three-Phase Neutral-Point-Clamped Inverter," *IEEE Transactions on Industrial Electronics,* vol. 57, pp. 2669-2678, 2010.
[71] C. A. Walford, "Wind Turbine Reliability: understanding and minimizing wind turbine operation and maintenance costs," Sandia National Laboratories, USA2006.
[72] P. Qian, X. Ma, and Y. Wang, "Condition monitoring of wind turbines based on extreme learning machine," presented at the 21st International Conference on Automation & Computing, Glasgow, UK, 2015.
[73] X. Ma, P. Cross, and P. Qian, "A condition monitoring system for an early warning of developing faults in wind turbine electrical systems," *Insight* vol. 58, pp. 663-670, 2016.
[74] J. Ribrant and L. M. Bertling, "Survey of Failures in Wind Power Systems With Focus on Swedish Wind Power Plants During 1997–2005," *IEEE Transactions on Energy Conversion,* vol. 22, pp. 167-173, 2007.
[75] L. M. Elobaid, A. K. Abdelsalam, and E. E. Zakzouk, "Artificial neural network-based photovoltaic maximum power point tracking techniques: a survey," *IET Renewable Power Generation,* vol. 9, pp. 1043-1063, 2015.
[76] A. Zaher, S. D. J. McArthur, D. G. Infield, and Y. Patel, "Online wind turbine fault detection through automated SCADA data analysis," *Wind Energy,* vol. 12, pp. 574-593, 2009.
[77] H. Guang-Bin, Z. Qin-Yu, K. Z. Mao, S. Chee-Kheong, P. Saratchandran, and N. Sundararajan, "Can threshold networks be trained directly?," *IEEE Transactions on Circuits and Systems II: Express Briefs,* vol. 53, pp. 187-191, 2006.
[78] Z.-L. Sun, K. M. Ng, J. Soszynska-Budny, and M. S. Habibullah, "Application of the LP-ELM Model on Transportation System Lifetime Optimization," *IEEE Transactions on Intelligent Transportation Systems,* vol. 12, pp. 1484-1494, 2011.
[79] C. Wan, Z. Xu, Y. Wang, Z. Y. Dong, and K. P. Wong, "A Hybrid Approach for Probabilistic Forecasting of Electricity Price," *IEEE Transactions on Smart Grid,* vol. 5, pp. 463-470, 2014.

[80] G. Feng, G. B. Huang, Q. Lin, and R. Gay, "Error minimized extreme learning machine with growth of hidden nodes and incremental learning," *IEEE Trans Neural Netw*, vol. 20, pp. 1352-7, Aug 2009.
[81] J. Tang, C. Deng, G.-B. Huang, and B. Zhao, "Compressed-Domain Ship Detection on Spaceborne Optical Image Using Deep Neural Network and Extreme Learning Machine," *IEEE Transactions on Geoscience and Remote Sensing*, vol. 53, pp. 1174-1185, 2015.
[82] A. Grigorievskiy, Y. Miche, M. Käpylä, and A. Lendasse, "Singular Value Decomposition update and its application to (Inc)-OP-ELM," *Neurocomputing*, vol. 174, pp. 99-108, 2016.
[83] N. Y. Liang, G. B. Huang, P. Saratchandran, and N. Sundararajan, "A fast and accurate online sequential learning algorithm for feedforward networks," *IEEE Trans Neural Netw*, vol. 17, pp. 1411-23, Nov 2006.
[84] B. Ozcelik and T. Erzurumlu, "Comparison of the warpage optimization in the plastic injection molding using ANOVA, neural network model and genetic algorithm," *Journal of Materials Processing Technology*, vol. 171, pp. 437-445, 2006.
[85] A. P. McCabe, G. A. Aggidis, and M. B. Widden, "Optimizing the shape of a surge-and-pitch wave energy collector using a genetic algorithm," *Renewable Energy*, vol. 35, pp. 2767-2775, 2010.
[86] P. Bangalore and L. B. Tjernberg, "An Artificial Neural Network Approach for Early Fault Detection of Gearbox Bearings," *IEEE Transactions on Smart Grid*, vol. 6, pp. 980-987, 2015.
[87] Y. Zhang, B. Du, L. Zhang, and S. Wang, "A Low-Rank and Sparse Matrix Decomposition-Based Mahalanobis Distance Method for Hyperspectral Anomaly Detection," *IEEE Transactions on Geoscience and Remote Sensing*, vol. 54, pp. 1376-1389, 2016.
[88] Y. Wang, Q. Miao, E. W. M. Ma, K.-L. Tsui, and M. G. Pecht, "Online anomaly detection for hard disk drives based on Mahalanobis distance," *IEEE Transactions on Reliability*, vol. 62, pp. 136-145, 2013.
[89] C. M. C. G. Fernandes, P. M. T. Marques, R. C. Martins, and J. H. O. Seabra, "Gearbox power loss. Part I: Losses in rolling bearings," *Tribology International*, vol. 88, pp. 298-308, 2015.
[90] C. M. C. G. Fernandes, P. M. T. Marques, R. C. Martins, and J. H. O. Seabra, "Gearbox power loss. Part III: Application to a parallel axis and a planetary gearbox," *Tribology International*, vol. 88, pp. 317-326, 2015.
[91] C. M. C. G. Fernandes, P. M. T. Marques, R. C. Martins, and J. H. O. Seabra, "Gearbox power loss. Part II: Friction losses in gears," *Tribology International*, vol. 88, pp. 309-316, 2015.
[92] P. Guo, D. Infield, and X. Yang, "Wind Turbine Generator Condition-Monitoring Using Temperature Trend Analysis," *IEEE Transactions on Sustainable Energy*, vol. 3, pp. 124-133, 2012.
[93] A. B. Borchersen and M. Kinnaert, "Model-based fault detection for generator cooling system in wind turbines using SCADA data," *Wind Energy*, vol. 19, pp. 593-606, 2016.

[94] P. Lall, P. Gupta, and K. Goebel, "Decorrelated Feature Space and Neural Nets Based Framework for Failure Modes Clustering in Electronics Subjected to Mechanical Shock," *IEEE Transactions on Reliability,* vol. 61, pp. 884-900, 2012.
[95] K. Krishnamoorthy and T. Mathew, *Statistical Tolerance Regions: Theory, Applications, and Computation*. NJ, USA: Wiley, 2009.
[96] N. Yaraghi, P. Tabesh, P. Guan, and J. Zhuang, "Comparison of AHP and Monte Carlo AHP Under Different Levels of Uncertainty," *IEEE Transactions on Engineering Management,* vol. 62, pp. 122-132, 2015.
[97] A. Moghadasi, A. Sarwat, and J. M. Guerrero, "Multiobjective optimization in combinatorial wind farms system integration and resistive SFCL using analytical hierarchy process," *Renewable Energy,* vol. 94, pp. 366-382, 2016.
[98] H. Tanaka, S. Tsukao, D. Yamashita, T. Niimura, and R. Yokoyama, "Multiple Criteria Assessment of Substation Conditions by Pair-Wise Comparison of Analytic Hierarchy Process," *IEEE Transactions on Power Delivery,* vol. 25, pp. 3017-3023, 2010.
[99] B. Le and J. Andrews, "Modelling wind turbine degradation and maintenance," *Wind Energy,* vol. 19, pp. 571-591, 2016.
[100] X. Ma, Y. Wang, and J. Qin, "Generic model of a community-based microgrid integrating wind turbines, photovoltaics and CHP generations," *Applied Energy,* vol. 112, pp. 1475-1482, 2013.
[101] E. Pouresmaeil, D. Montesinos-Miracle, O. Gomis-Bellmunt, and A. Sudrià-Andreu, "Instantaneous active and reactive current control technique of shunt active power filter based on the three-level NPC inverter," *European Transactions on Electrical Power,* vol. 21, pp. 2007-2022, 2011.
[102] L. Shun, H. Qiaohui, and L. Wei-Jen, "A Survey of Harmonic Emissions of a Commercially Operated Wind Farm," *IEEE Transactions on Industry Applications,* vol. 48, pp. 1115-1123, 2012.
[103] J. Allmeling, "A Control Structure for Fast Harmonics Compensation in Active Filters," *IEEE Transactions on Power Electronics,* vol. 19, pp. 508-514, 2004.
[104] L. Wang, D. Zhang, Y. Wang, B. Wu, and H. S. Athab, "Power and Voltage Balance Control of a Novel Three-Phase Solid-State Transformer Using Multilevel Cascaded H-Bridge Inverters for Microgrid Applications," *IEEE Transactions on Power Electronics,* vol. 31, pp. 3289-3301, 2016.
[105] B. N. Roodsari and E. P. Nowicki, "Fast space vector modulation algorithm for multilevel inverters and its extension for operation of the cascaded H-bridge inverter with non-constant DC sources," *IET Power Electronics,* vol. 6, pp. 1288-1298, 2013.
[106] K. Ma and F. Blaabjerg, "The Impact of Power Switching Devices on the Thermal Performance of a 10 MW Wind Power NPC Converter," *Energies,* vol. 5, pp. 2559-2577, 2012.

[107] S. M. Muyeen, R. Takahashi, and J. Tamura, "Wind power and hydrogen generation system with cooperatively controlled three-level NPC-VSC based energy capacitor," *European Transactions on Electrical Power,* vol. 20, pp. 1071-1081, 2010.
[108] T. Zaveri, B. R. Bhalja, and N. Zaveri, "Load compensation using DSTATCOM in three-phase, three-wire distribution system under various source voltage and delta connected load conditions," *International Journal of Electrical Power & Energy Systems,* vol. 41, pp. 34-43, 2012.
[109] S. Saad and L. Zellouma, "Fuzzy logic controller for three-level shunt active filter compensating harmonics and reactive power," *Electric Power Systems Research,* vol. 79, pp. 1337-1341, 2009.
[110] U.-M. Choi, F. Blaabjerg, and K.-B. Lee, "Method to Minimize the Low-Frequency Neutral-Point Voltage Oscillations With Time-Offset Injection for Neutral-Point-Clamped Inverters," *IEEE Transactions on Industry Applications,* vol. 51, pp. 1678-1691, 2015.
[111] J. Rodriguez, S. Bernet, P. K. Steimer, and I. E. Lizama, "A Survey on Neutral-Point-Clamped Inverters," *IEEE Transactions on Industrial Electronics,* vol. 57, pp. 2219-2230, 2010.
[112] P. Caramia, G. Carpinelli, M. Pagano, and P. Varilone, "Probabilistic three-phase load flow for unbalanced electrical distribution systems with wind farms," *IET Renewable Power Generation,* vol. 1, p. 115, 2007.
[113] C. Wang, K. Wang, and X. You, "Research on Synchronized SVPWM Strategies Under Low Switching Frequency for Six-Phase VSI-Fed Asymmetrical Dual Stator Induction Machine," *IEEE Transactions on Industrial Electronics,* vol. 63, pp. 6767-6776, 2016.
[114] B. Venugopal Reddy and V. T. Somasekhar, "An SVPWM Scheme for the Suppression of Zero-Sequence Current in a Four-Level Open-End Winding Induction Motor Drive With NestedRectifier–Inverter," *IEEE Transactions on Industrial Electronics,* vol. 63, pp. 2803-2812, 2016.
[115] M. Gu, S. Ogasawara, and M. Takemoto, "Novel PWM Schemes With Multi SVPWM of Sensorless IPMSM Drives for Reducing Current Ripple," *IEEE Transactions on Power Electronics,* vol. 31, pp. 6461-6475, 2016.
[116] A. Yazdani and R. Iravani, "A Generalized State-Space Averaged Model of the Three-Level NPC Converter for Systematic DC-Voltage-Balancer and Current-Controller Design," *IEEE Transactions on Power Delivery,* vol. 20, pp. 1105-1114, 2005.
[117] J. Zaragoza, J. Pou, S. Ceballos, E. Robles, C. Jaen, and M. Corbalan, "Voltage-Balance Compensator for a Carrier-Based Modulation in the Neutral-Point-Clamped Converter," *IEEE Transactions on Industrial Electronics,* vol. 56, pp. 305-314, 2009.
[118] U.-M. Choi, J.-S. Lee, and K.-B. Lee, "New Modulation Strategy to Balance the Neutral-Point Voltage for Three-Level Neutral-Clamped Inverter Systems," *IEEE Transactions on Energy Conversion,* vol. 29, pp. 91-100, 2014.

[119] S. R. Pulikanti, M. S. A. Dahidah, and V. G. Agelidis, "Voltage Balancing Control of Three-Level Active NPC Converter Using SHE-PWM," *IEEE Transactions on Power Delivery,* vol. 26, pp. 258-267, 2011.
[120] X. Chen and M. Kazerani, "Space Vector Modulation Control of an AC–DC–AC Converter With a Front-End Diode Rectifier and Reduced DC-link Capacitor," *IEEE Transactions on Power Electronics,* vol. 21, pp. 1470-1478, 2006.
[121] Z. Huibin, S. Jon Finney, A. Massoud, and B. W. Williams, "An SVM Algorithm to Balance the Capacitor Voltages of the Three-Level NPC Active Power Filter," *IEEE Transactions on Power Electronics,* vol. 23, pp. 2694-2702, 2008.
[122] O. Bouhali, B. Francois, E. M. Berkouk, and C. Saudemont, "DC Link Capacitor Voltage Balancing in a Three-Phase Diode Clamped Inverter Controlled by a Direct Space Vector of Line-to-Line Voltages," *IEEE Transactions on Power Electronics,* vol. 22, pp. 1636-1648, 2007.
[123] Dongsheng Zhou and Didier G. Rouaud, "Experimental comparisons of space vector neutral point balancing strategies for three-level topology," *IEEE Transactions on Power Electronics,* vol. 16, pp. 872-879, November 2001.
[124] Nikola Celanovic and Dushan Boroyevich, "A comprehensive study of neutral-point voltage balancing problem in three-level neutral-point-clamped voltage source PWM inverters," *IEEE Transactions on Power Electronics,* vol. 15, pp. 242-249, March 2000.
[125] S. Busquets-Monge, J. Bordonau, D. Boroyevich, and S. Somavilla, "The nearest three virtual space vector PWM - a modulation for the comprehensive neutral-point balancing in the three-level NPC inverter," *IEEE Power Electronics Letters,* vol. 2, pp. 11-15, 2004.
[126] M. K. Mishra, A. Joshi, and A. Ghosh, "Control schemes for equalization of capacitor voltages in neutral clamped shunt compensator," *IEEE Transactions on Power Delivery,* vol. 18, pp. 538-544, 2003.
[127] Y. Li, Y. Peng, F. Liu, D. Sidorov, D. Panasetsky, C. Liang, *et al.*, "A Controllably Inductive Filtering Method With Transformer-Integrated Linear Reactor for Power Quality Improvement of Shipboard Power System," *IEEE Transactions on Power Delivery*, pp. 1-1, 2016.

Appendix A

1	Mains voltage L2 -L3	V		1	Angels	Nacelle Position
2	Mains voltage L1 - L3	V		2		Twist
3	Mains voltage L1 - L2	V		3		Minimum pitch angle
4	Mains current L1	A		4		Redundant pitch postion 1
5	Mains current L2	A		5		Redundant pitch postion 2
6	Mains current L3	A		6		Redundant pitch postion 3
7	Apparent power	kVA		7		Pitch angle blade 1
8	Pitch Motor Current 3	A		8		Pitch angle blade 2
9	Reactive power	kVAr		9		Pitch angle blade 3
10	Power factor			10		Pitch angle average blade 1-3
11	Oscillation Signal Eff Y	cm/s²		11	Electrical	Mains voltage L2 -L3
12	Oscillation Signal Eff Z	cm/s²		12		Mains voltage L1 - L3
13	Set value brake	bar		13		Mains voltage L1 - L2
14	Oscillation Signal Filt Eff Y	cm/s²		14		Mains current L1
15	Wind speed	m/s		15		Mains current L2
16	Wind speed left-hand	m/s		16		Mains current L3
17	Wind speed right-hand	m/s		17		Apparent power
18	Wind direction	°		18		Active power
19	Wind direction left-hand	°		19		Reactive power
20	Wind direction right-hand	°		20		Power factor
21	Speed generator	U/min		21		EB Vw P
22	Speed rotor	U/min		22		Net Frequency
23	System pressure	bar		23		Pitch Motor Current 1
24	Speed rotor over speed controller	U/min		24		Pitch Motor Current 2
25	Brake pressure	bar		25		Pitch Motor Current 3
26	Oil pressure gearbox	bar		26		Pitch Inverter Voltage 1
27	Temperature cooling water generator advance	°C		27		Pitch Inverter Voltage 2
28	Oscillation Signal Filt Eff Z	cm/s²		28		Pitch Inverter Voltage 3
29	Temperature Outside	°C		29	Setpoints	Set value brake
30	Temperature Generator L1	°C		30		Generator RPM reference value
31	Temperature Generator L2	°C		31		Generator RPM setpoint
32	Temperature Gearbox Bearing 1	°C		32		Torque difference
33	Temperature Gearbox Oil Heat Exchanger Outpu	°C		33		Torque setpoint Out
34	Temperature Nacelle	°C		34		Maximum allowed change of RPM setpoint
35	Pitch Converter Temperature 1	°C		35		Measuring bus channel 21.1.1
36	Temperature main bearing 1	°C		36		Measuring bus channel 21.1.2
37	Temperature main bearing 2	°C		37		Measuring bus channel 21.1.3
38	Temperature hydraulic fluid	°C		38		Measuring bus channel 21.1.4
39	Temperature cooling water generator return	°C		39		Measuring bus channel 21.1.5
40	Temperature generator bearing AS	°C		40		Measuring bus channel 21.1.6
41	Temperature generator bearing BS	°C		41		Measuring bus channel 21.1.7
42	Pitch Converter Temperature 2	°C		42		Measuring bus channel 21.1.8
43	Temperature Gearbox Oil Sump	°C		43		Operation state
44	Oil Pressure Gearbox Behind Pump	bar		44		Pit_PID1_P
45	Temperature Topbox 1	°C		45		Pit_PID1_I
46	Temperature Topbox 2	°C		46		Pit_PID1_D
47	Vibration y-direction	cm/s²		47		Pit_PID1
48	Vibration z-direction	cm/s²		48		Pit_PID2_P
49	Nacelle Position	°		49		Pit_PID2_I
50	LS Temperature Control Switchboard	°C		50		Pitch mode
51	LS Temperature Power Switchboard	°C		51		Set-point pitch angle blade 1
52	Medium VoltageTrafo Temperature	°C		52		Set-point pitch angle blade 2
53	KS Temperature	°C		53		Set-point pitch angle blade 3
54	Pitch Statusword Pitchdrive 1			54		Set-point pitch angle
55	Pitch Statusword Pitchdrive 2			55		Setpoint pitch speed
56	Pitch Statusword Pitchdrive 3			56		Pitch Motor 1 RPM Setpoint
57	Pitch Alarmword Pitchdrive 1			57		Pitch Motor 2 RPM Setpoint
58	Pitch Alarmword Pitchdrive 2			58		Pitch Motor 3 RPM Setpoint
59	Pitch Alarmword Pitchdrive 3			59		Pitch Statusword Pitchdrive 1
60	Redundant pitch postion 1	°		60		Pitch Statusword Pitchdrive 2
61	Twist			61		Pitch Statusword Pitchdrive 3
62	Temperature Pitchmotor 1	°C		62		Pitch Alarmword Pitchdrive 1
63	Temperature Pitchmotor 2	°C		63		Pitch Alarmword Pitchdrive 2
64	Temperature Pitchmotor 3	°C		64		Pitch Alarmword Pitchdrive 3

65:H1	Redundant pitch postion 2	°		65		Air Pressure	[Factor]
66	Redundant pitch postion 3	°		66	Pressures	Oil Pressure Gearbox Behind Pump	bar
67	Air Pressure	[Factor]		67		System pressure	bar
68	Pitch angle blade 1	°		68		Brake pressure	bar
69	Pitch angle blade 2	°		69		Oil pressure gearbox	bar
70	Pitch angle blade 3	°		70		Gear Oil Pressure Behind Pump B	bar
71	Pitch angle average blade 1-3	°		71	Oscillations	Oscillation Signal Eff Y	cm/s²
72	Set-point pitch angle blade 1	°		72		Oscillation Signal Eff Z	cm/s²
73	Set-point pitch angle blade 2	°		73		Oscillation Signal Filt Eff Y	cm/s²
74	Set-point pitch angle blade 3	°		74		Oscillation Signal Filt Eff Z	cm/s²
75	Set-point pitch angle	°		75		Vibration y-direction	cm/s²
76	Measuring bus channel 21.1.1			76		Vibration z-direction	cm/s²
77	Setpoint pitch speed	°/s		77	Speeds	Speed generator	U/min
78	Minimum pitch angle	°		78		Speed rotor	U/min
79	Maximum pitch speed	°/s		79		Speed rotor over speed controller	U/min
80	Generator RPM reference value	U/min		80		Maximum pitch speed	°/s
81	Maximum allow ed change of RPM setpoint	U/min/s		81		Generator speed ST-RFC	U/min
82	Generator speed ST-RFC	U/min		82		Generator speed ST-RFC (to-default)	U/min
83	Generator speed ST-RFC (to-default)	U/min		83		Pitch Motor 1 RPM	U/min
84	Generator RPM setpoint	U/min		84		Pitch Motor 2 RPM	U/min
85	Operation state			85		Pitch Motor 3 RPM	U/min
86	Measuring bus channel 21.1.2			86	Wind	Wind speed	m/s
87	Measuring bus channel 21.1.3			87		Wind speed left-hand	m/s
88	Measuring bus channel 21.1.4			88		Wind speed right-hand	m/s
89	Measuring bus channel 21.1.5			89		Wind direction	°
90	Measuring bus channel 21.1.6			90		Wind direction left-hand	°
91	Measuring bus channel 21.1.7			91		Wind direction right-hand	°
92	Temperature GearCoolWa behind OilHE	°C		92	Temperatures	Temperature cooling w ater generator advance	°C
93	Temperature GearCW before OilHE	°C		93		Temperature Outside	°C
94	Temperature Gearbox Bearing 2	°C		94		Temperature Generator L1	°C
95	Temperature Cooling Water Inverter Flow	°C		95		Temperature Generator L2	°C
96	Temperature Cooling Water MI Return	°C		96		Temperature Gearbox Bearing 1	°C
97	EB Vw P	[Factor]		97		Temperature Gearbox Oil Heat Exchanger Outpu	°C
98	Net Frequency	Hz		98		Temperature Nacelle	°C
99	Measuring bus channel 21.1.8			99		Pitch Converter Temperature 1	°C
100	Hygrometer 1 Relative Humidity	%		100		Temperature main bearing 1	°C
101	Hygrometer 1 Temperature	°C		101		Temperature main bearing 2	°C
102	Hygrometer 2 Relative Humidity	%		102		Temperature hydraulic fluid	°C
103	Hygrometer 2 Temperature	°C		103		Temperature cooling w ater generator return	°C
104	Gear Oil Pressure Behind Pump B	bar		104		Temperature generator bearing AS	°C
105	Torque difference	Nm		105		Temperature generator bearing BS	°C
106	Torque setpoint Out	Nm		106		Pitch Converter Temperature 2	°C
107	Pitch mode	[Factor]		107		Temperature Gearbox Oil Sump	°C
108	Active pow er pitch	kW		108		Temperature Topbox 1	°C
109	Pit_PID1_P	°/s		109		Temperature Topbox 2	°C
110	Pit_PID1_I	°/s		110		LS Temperature Control Sw itchboard	°C
111	Pit_PID1_D	°/s		111		LS Temperature Pow er Sw itchboard	°C
112	Pit_PID1	°/s		112		Medium VoltageTrafo Temperature	°C
113	Pit_PID2_P	°		113		KS Temperature	°C
114	Pit_PID2_I	°		114		Temperature Pitchmotor 1	°C
115	Relative Humidity Nacelle	%		115		Temperature Pitchmotor 2	°C
116	Pitch Converter Temperature 3	°C		116		Temperature Pitchmotor 3	°C
117	Pitch Motor 1 RPM Setpoint	U/min		117		Temperature GearCoolWa behind OilHE	°C
118	Pitch Motor 2 RPM Setpoint	U/min		118		Temperature GearCW before OilHE	°C
119	Pitch Motor 3 RPM Setpoint	U/min		119		Temperature Gearbox Bearing 2	°C
120	Pitch Motor 1 RPM	U/min		120		Temperature Cooling Water Inverter Flow	°C
121	Pitch Motor 2 RPM	U/min		121		Temperature Cooling Water MI Return	°C
122	Pitch Motor 3 RPM	U/min		122		Hygrometer 1 Temperature	°C
123	Pitch Inverter Voltage 1	V		123		Hygrometer 2 Temperature	°C
124	Pitch Inverter Voltage 2	V		124		Pitch Converter Temperature 3	°C
125	Pitch Inverter Voltage 3	V		125	Others	Hygrometer 1 Relative Humidity	%
126	Pitch Motor Current 1	A		126		Hygrometer 2 Relative Humidity	%
127	Pitch Motor Current 2	A		127		Relative Humidity Nacelle	%
128	Active pow er	kW		128		Active pow er pitch	kW

Detail of SCADA data